SLAC – 293
UC – 34D
(T/E)

A SEARCH FOR PRIMARILY NON-INTERACTING DECAY MODES OF THE UPSILON*

John Stephen Leffler

Stanford Linear Accelerator Center
Stanford University
Stanford, California 94305

March 1986

Prepared for the Department of Energy
under contract number DE-AC03-76SF00515

Printed in the United States of America. Available from the National Technical Information Service, U.S. Department of Commerce, 5285 Port Royal Road, Springfield, Virginia 22161. Price: Printed Copy A07, Microfiche A01.

* Ph.D. Dissertation.

ABSTRACT

The hadronic transition $\Upsilon(2S) \rightarrow \pi^0\pi^0\Upsilon(1S)$ is utilized to search for the reactions: $\Upsilon(1S) \rightarrow$non-interacting particles and $\Upsilon(1S) \rightarrow \gamma +$ non-interacting particles. 44 pb^{-1} of $\Upsilon(2S)$ data was taken by the Crystal Ball detector at the DORIS II storage ring in order to perform this study.

An upper limit of

$$BR(\Upsilon \rightarrow Unseen) < 12\% \qquad (90\%\ C.L.)\ ,$$

is obtained via this approach.

The second process investigated involved the radiative decay of the Upsilon into non-interacting particles. 57 $pb^{-1}$of $\Upsilon(2S)$ data was available for this study. An upper limit on the branching ratio BR($\Upsilon \rightarrow \gamma +$ Unseen) is measured for photon energies in the range $500\ MeV < E_\gamma < \frac{M_\gamma}{2}$. This is the first reported measurement of this type. For the highest energy photons, an upper limit of

$$BR(\Upsilon \rightarrow \gamma + Unseen) < 2.3 \times 10^{-3} \qquad (90\%\ C.L.)\ ,$$

is obtained. The compact size of the Crystal Ball detector enhances the observable branching ratio for noninteracting particles with short lifetimes such as massive axions. The identification of the recent Darmstadt events with a 1.6 MeV axion is excluded by the present result assuming the minimal Peccei-Quinn model. Limits on the spontaneous supersymmetry breaking mass scale are also derived as a function of gravitino mass.

ACKNOWLEDGEMENTS

I would like to take this opportunity to thank all the members of the Crystal Ball Collaboration for helping to make this thesis possible. In particular, I wish to thank my advisor, Elliott Bloom, for inspiring this thesis topic and providing the guidance and support necessary to its completion, for constant intellectual stimulation and for his timely editorial assistance. I am indebted to Gary Godfrey for taking an interest in this analysis and making extremely useful suggestions in this regard. I also received valuable analysis advice and aid from Frank Porter, Andreas Schwarz, Susan Cooper and my fellow graduate students: Roger Lee, David Gelphman, Ray Cowan, Duncan Prindle, David Williams and Steve Lowe. John Broeder's technical experience and advice was quite handy at times. Moral support and camaraderie from John Gaiser, Achim Irion, Peter Schmitt, Stefan Keh, Wim Walk, Patty McBride, Gabi Glaser, Andrea Higashi and Nina Adelman was appreciated as well.

For fellowship above and beyond the call of grad school, I would like to nominate: Steve Lindgren, George Pastrana, John Butler, Les Rosenberg and Harry Nelson.

For helping me while away the last few years, the only nominee in the best office-mate category is clearly: Steve Lowe.

The award for TEXnical achievement must go to Ray Cowan whose typesetting software and uncountable hours of consultation (at cut rate) greatly enhanced the esthetic appeal and production rate of this thesis. June Belew, his assistant, was invaluable to this effort.

The off-site unit was responsible for providing non-physics related stimuli, real life simulation, sounding boards, sympathy, haute cuisine, and raucous gatherings. For their work in this regard, the nominees are Liz and Pam.

I would also like to gratefully acknowledge the encouragement and inspiration received from the Physics (and French!!) department at Wright State University while I was an undergraduate. Drs. Andrews, Martin, Thomas, Wolfe, Hansen, Hemsky, Racevskis, Horn, Matual and Liaugminas (honorary) were among those responsible for many fascinating and illuminating experiences. The friendship of Ellen, Daniela and Todd has helped me through many rough spots since those days.

Many thanks are due to Dr. Fontaine and the physics faculty at the Université Claude Bernard in Lyon, France, and the friends I made there, for welcoming and sustaining me during my academic séjour there.

I dedicate this thesis to my father, whose interest in science was somehow contagious.

Table of Contents

1. Introduction and Summary *1*

1.1 The Upsilon System *1*

1.2 The Search for Rare Decay Modes of the Υ *2*

1.3 Υ Tagging via Hadronic Transitions from the Υ' *3*

1.4 Rare Upsilon Decays *6*

1.4.1 $\Upsilon \rightarrow$ *Unseen* *7*

1.4.2 $\Upsilon \rightarrow \gamma +$ *Unseen* *11*

1.5 Summary *21*

References *22*

2. The Crystal Ball Detector at DORIS II *25*

2.1 The Move to DORIS II *25*

2.2 Experimental Overview *27*

2.3 The Crystal Ball Detector *29*

2.3.1 *The Central Detector* *29*

2.3.2 *Tube Chambers* *32*

2.3.3 *Endcaps* *34*

2.3.4 *Luminosity Measurement* *36*

2.3.5 *Time of Flight System* *36*

References *38*

3. Data Acquisition and Initial Analysis *39*

3.1 Data Acquisition Chain *39*

3.2 Calibration *40*

3.3 Pre-selection and Production *42*

3.3.1 *Connected Regions* *43*

3.3.2 *Bumps* *43*

3.3.3 *Tracking* *44*

3.3.4 *ESORT* *45*

3.3.5 *TOF* *47*

3.4 Photon Identification *48*

3.5 π^0 and $\pi^0\pi^0$ Identification *49*

References *52*

4. Search for $\Upsilon' \to \pi^0\pi^0\Upsilon$, $\Upsilon \to$ Unseen *54*

4.1 Data Selection and Analysis *55*

4.1.1 *Pass 1 Cuts* *55*

4.1.2 *CONTAG* *55*

4.1.3 *Pass 2 Cuts* *57*

4.2 Analysis Efficiency Determination *58*

4.2.1 *Monte Carlo Event Samples* *58*

4.2.2 *Trigger Efficiency* *60*

4.2.3 *Pass 1 Analysis Efficiency* *60*

4.2.4 *CONTAG Charged Particle Efficiency* *61*

4.2.5 *Pass 2 Analysis Efficiency* *62*

4.2.6 *Final Detection and Analysis Efficiency* *62*

4.3 Results *64*

4.3.1 *Pion Mass Distributions* *64*

4.3.2 $\pi^0\pi^0$*Kinematic Distributions* *65*

4.3.3 *Angular Distributions* *65*

4.3.4 *Missing Mass Distributions* *69*

4.3.5 *Acceptance Correction* 79
4.4 Contribution from Other Processes 85
4.4.1 *Monte Carlo Estimate of* $\Upsilon \rightarrow$ *Lepton Pairs* 85
4.4.2 *Two-photon Acceptance* 88
4.5 Conclusion 91

References 94

5. Search for $\Upsilon' \rightarrow \pi^0\pi^0\Upsilon$, $\Upsilon \rightarrow \gamma$ + **Unseen.** 95
5.1 Data Selection and Analysis 95
5.2 Detection and Analysis Efficiency 96
5.3 Results 97
5.3.1 π^0*and* $\pi^0\pi^0$*System Angular and Kinematic Distributions.* . . 97
5.3.2 *Photon Energy Distributions* 102
5.4 Conclusions 105

6. Conclusions 107

Appendix A. Trigger System 109
A.1 Trigger System Overview 109
A.2 Trigger Electronics 111
A.2.1 *Event Timing* 113
A.3 Trigger Logic 114
A.3.1 *Total Energy* 114
A.3.2 *Back-To-Back Topology Condition* 114
A.3.3 *Major Triangle Multiplicity* 114
A.3.4 *Hemispherical Topology* 115
A.3.5 *Tunnel Veto* 115
A.4 Trigger Architecture 116
A.4.1 *NIM NMULT Trigger* 117
A.4.2 *NIM Topo Trigger* 117
A.4.3 *Random Beam-crossing Triggers* 121

References 123

Appendix B. Monte Carlo *124*
B.1 Organization *124*
B.2 Detector Simulation *125*
B.2.1 *DORIS II Endcaps* *126*
B.3 Trigger Simulation *130*
References *137*

Figure Captions

[1.1] Total visible hadronic cross section as a function of center of mass energy. 2

[1.2] 90% C.L. for BR($\Upsilon \rightarrow \gamma +$ Unseen) versus photon energy. 8

[1.3] Photon energy spectrum for the decay $\Upsilon \rightarrow \gamma\lambda\overline{\lambda}$. 12

[1.4] Kinematic factor K(y) (from eqn. [1.62]) as a function of the mass ratio $y = 2m_\lambda / M_{Q\overline{Q}}$. 19

[1.5] Lower limit on Λ_{ss} as a function of gravitino or goldstone fermion mass. 21

[2.1] The Semitrailer containing the Crystal Ball being loaded into a C-5A at Travis Air Force Base. 26

[2.2] DORIS II storage ring and feeder systems. 28

[2.3] Crystal Ball Detector components in DORIS II configuration. 29

[2.4] Geometrical structures employed in Crystal Ball nomenclature. 31

[2.5] The Crystal Ball tube chamber system. 33

[2.6] The Crystal Ball Endcap Array. 35

[3.1] Relationship between a NaI module and its surrounding modules. 44

[3.2] A 'flats' display of a multihadron event. 46

[3.3] Photon pattern cut energy ratios. 49

[4.1] Charged event probability distribution for a subset of Pass 1 data sample. 56

[4.2] $m_{\gamma\gamma}$ *vs* $m_{\gamma\gamma}$ scatterplot for events with $\geq$ 4 tracks (Final sample after PHYSAC kinematic fitting). 66

[4.3] $\pi^0\pi^0$ system mass distributions for the final event sample. *67*

[4.4] $cos\,\theta$ for pions found by PHYSAC. *68*

[4.5] cos $\theta_{\pi\pi}$ distribution for pion pairs found by PHYSAC. *68*

[4.6] Missing mass distribution for π^0pairs found by PHYSAC. *71*

[4.7] Gaussian Amplitudes and means for fixed MC width fits performed in table 4.3. . . . . *72*

[4.8] Fit to the Missing mass distribution of figure 4.6. . . . . *72*

[4.9] Fit to the Missing mass distribution of figure 4.6. . . . . *73*

[4.10] Fit to the Missing mass distribution of figure 4.6. . . . . *73*

[4.11] $\pi^0\pi^0$ system energy vs missing mass for events in the final data sample. *74*

[4.12] $\pi^0\pi^0$ system mass vs missing mass for events in the final data sample. *75*

[4.13] $\pi^0\pi^0$ system total momentum vs missing mass for events in the final data sample. *76*

[4.14] $\pi^0\pi^0$ system transverse momentum-squared vs missing mass for events in the final data sample. *77*

[4.15] $\pi^0\pi^0$ system transverse momentum-squared vs missing mass for Monte Carlo Events. *78*

[4.16] Detector + Analysis efficiency versus M_X. *81*

[4.17] Acceptance Corrected Missing Mass Distribution. *82*

[4.18] Fit to Acceptance Corrected Missing Mass Distribution. *83*

[4.19] Fit to Acceptance Corrected Missing Mass Distribution (+10 MeV Shift). *83*

[4.20] Fit to Acceptance Corrected Missing Mass Distribution (-10 MeV Shift). *84*

[4.21] $\pi^0\pi^0\pi^0$ System Mass Distribution. *88*

[4.22] $\pi^0\pi^0\pi^0$ System Mass Distribution $P_T^2 < 10000$. *89*

[5.1] Detector and Analysis Efficiency for the process $\Upsilon' \rightarrow \pi^0\pi^0\Upsilon$, $\Upsilon \rightarrow \gamma +$ Unseen. *98*

[5.2] $m_{\gamma\gamma}$ *vs* $m_{\gamma\gamma}$ scatterplot for NTOPO events with ≥ 5 tracks (Final sample after PHYSAC kinematic fitting). *99*

[5.4] $cos\,\theta$ for pions found by PHYSAC. *100*

[5.5] cos $\theta_{\pi\pi}$ distribution for pion pairs found by PHYSAC. *100*

[5.6] Dipion system mass distribution for NTOPO final sample five track events. *101*

[5.7] Missing mass distribution for NTOPO final sample five track events. *101*

[5.8] Missing mass versus unpaired photon energy for events passing cuts 7-9. . . . . *103*

[5.9] Missing Mass Distribution for $E_\gamma > 500$ MeV events passing cuts 7-9. . . . . *104*

[5.10] E_γ distribution for events with $9400 < m_{missing} < 9500$. *104*

[5.11] E_γ (0-1500 MeV) distribution for events with $9400 < m_{missing} < 9500$. *106*

[5.12] 90% C.L. Upper Limit for BR($\Upsilon \rightarrow \gamma$+Unseen) for $500 < E_\gamma < 5000$ MeV *106*

[A.1] Trigger System Timing Distributions. *113*

[A.2] Tunnel Region Energy Distribution. *116*

[A.3] NIM Trigger System Logic. *118*

[A.4] NIM NMULT Trigger efficiency versus total energy. *120*

[A.5] Background Energy Distribution. *122*

[B.1] Data Flow in the Crystal Ball Monte Carlo. *125*

[B.2] Orthogonal side view of +Z endcap stacking scheme. *128*

[B.3] Projective (top) and orthogonal (bottom) view of the +Z endcap array as seen from a particle emanating from the interaction point. *129*

[B.4] NIM Tunnel Module Veto discriminator efficiency curve. *131*

[B.5] NTOPO total energy discriminator efficiency curve. *132*

[B.6] NMULT total energy efficiency derived from software major triangle energy thresholds. *134*

[B.7] NMULT trigger major triangle 1-4 discriminator efficiency curves. *135*

[B.8] Measured (A) and derived (B) discriminator efficiency curves for major triangle #7. . . . . *136*

Chapter 1

Introduction and Summary

1.1 The Upsilon System

Two heavy quark-antiquark resonance systems are known to exist. The charmonium system, which consists of a charm quark bound to a charm antiquark, was the first to be discovered. The so called 1974 "November Revolution" in particle physics began with the near simultaneous announcement by two separate groups that an incredibly narrow resonance had been seen at a mass of 3.1 GeV. The signal was detected in an e^+e^- colliding beam experiment at the Stanford Linear Accelerator Center (SLAC) and in a proton-nucleon scattering experiment at the Brookhaven National Laboratory (BNL).[1]

The existence of the charm quark and the tau lepton led to speculations that still heavier quark species might exist.[2,3] In 1977, a group at the Fermi National Laboratory (FNAL) discovered peaks in the dimuon mass plot while investigating the reaction $p + Be \rightarrow \mu^+\mu^- + X$ at 400 GeV beam energies.[4] Initially two and eventually three peaks at 9.5, 10.0 and 10.4 GeV center-of-mass energies were resolved as more data was accumulated. The Upsilon was soon produced at the e^+e^- storage ring DORIS located at the Deutsches Electronen Synchrotronen Laboratory (DESY).[5] The lowest two peaks were measured to have masses of 9.46 and 10.02 GeV. In 1980, the CESR e^+e^- storage ring at Cornell University began operation and observed the third Upsilon state 890 MeV above the first.[6]

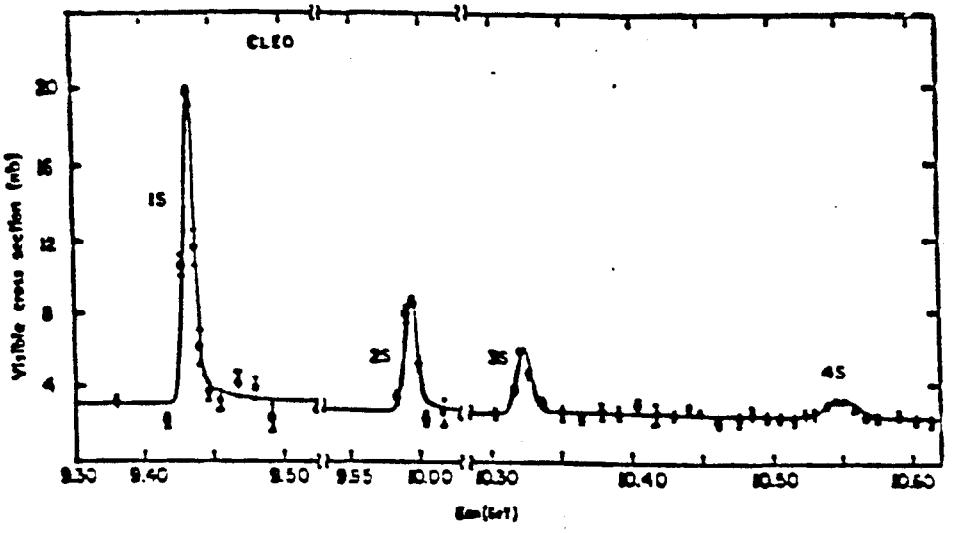

Fig. 1.1 Total visible hadronic cross section as a function of center of mass energy. Data are from the CLEO detector located at the CESR e^+e^- storage ring.

A fourth, broader, energy level was identified in the storage ring experiments at 10.55 GeV.[7] Figure 1.1 illustrates the Upsilon resonance as reported by the CLEO experiment at CESR.[8] It was quickly realized that the Upsilon system was a second example of a quark-antiquark resonance and that it was composed of a new heavy quark species, the bottom quark. As the $b\bar{b}$ system was studied, it became clear that it was quite similar to the $c\bar{c}$ system both in terms of the structure of its energy levels and in the transition modes between these levels.

1.2 The Search for Rare Decay Modes of the Υ

The Upsilon, which has a full width of about 45 KeV, is one of the narrowest quark bound states known to decay via the strong interaction. Due to their mass, the constituent bottom quarks are nonrelativistic with $\langle\beta^2\rangle \sim 0.08$. This fact allows calculation of the quark-antiquark interactions to proceed via the use of nonrelativistic methods. The relative ease of calculation in heavy quark systems

has allowed certain aspects of QCD, the theory of the strong interaction, to be experimentally tested for the first time. Predictions of hadronic and radiative transition rates between the upsilon states are of great interest and, as a result, have been extensively measured for both the $c\bar{c}$ and $b\bar{b}$ systems. The use of such transitions to the $c\bar{c}$ and $b\bar{b}$ $1\,^3S_1$ state was soon proposed[9] as a means of measuring decays to unobservable final state particles or decays which suffer from high backgrounds when measured via direct production processes. The narrowness of the Υ(1S) state and its large mass enhances the branching ratio of decay processes compared to a measurement involving a typical $q\bar{q}$ state having a full width thousands of times greater or the lighter $c\bar{c}$ system. Therefore the detection of decay processes involving partial widths on the order of a few eV or less into objects with masses as high as a few GeV is possible given a large enough data sample of Upsilon decays. This sensitivity provides a means to search for hitherto unobserved particle interactions involving small coupling constants. It is the goal of this thesis to utilize hadronic transitions from the Υ(2S) to the Υ(1S) in order to place an upper limit on the branching ratio for Υ(1S) direct or radiative decays into neutrino pairs, supersymmetric particles and "mirror" particles. These Upsilon decay processes have been proposed by various theorists to have partial widths in the range of 4-4000 eV. The next section will briefly describe the methodology employed for this study as well as the history of this approach, while the following section will detail the theoretical expectations for the studied processes.

1.3 Υ Tagging via Hadronic Transitions from the Υ'

The presence of transitions between the Upsilon states provides an interesting mechanism for the study of any state accessible by such a process. Basically, the idea is to make use of the transition process itself in order to determine that a given state was produced. For instance, the Υ(1S) is produced via the following decays:

$$
\begin{array}{lll}
(a) & \Upsilon(2S) \rightarrow \pi^+\pi^- & \Upsilon(1S). \\
(b) & \Upsilon(2S) \rightarrow \pi^0\pi^0 & \Upsilon(1S). \\
(c) & \Upsilon(2S) \rightarrow \gamma\, {}^3P_J & \\
 & \qquad\qquad \big\lfloor\!\!\longrightarrow \gamma\Upsilon(1S). & \\
(d) & \Upsilon(2S) \rightarrow \eta & \Upsilon(1S). \quad (Expected)
\end{array}
\qquad [1.1]
$$

These reactions have been ranked from highest to lowest branching ratio. Reaction (a,b,d) involve a hadronic transition from the Υ(2S) to the Υ(1S). In reaction (c), the Υ(2S) decays radiatively into one of its P-states which then repeats the process to produce an Υ(1S). Due to their low branching ratios ($< 2\%$) and possible confusion with background processes, reactions (c) and (d) are not good candidates for the production and tagging of Υ(1S) states. Reactions (a) and (b) involve branching ratios of 17% and 8% respectively. In the J/ψ system, the $\pi^+\pi^-$ and $\pi^0\pi^0$ transitions account for branching ratios of 33% and 17% respectively. Therefore the $\pi\pi$ hadronic transition mode is a natural choice as a means of producing a large sample of tagged J/ψ or Υ particles.

The Mark II collaboration has measured[10]

$$BR(J/\psi \rightarrow Unseen) < 7 \times 10^{-3}, \qquad (95\%\ \text{C.L.}) \qquad [1.2]$$

by means of the reaction $\psi' \rightarrow \pi^+\pi^-\, J/\psi$. The CLEO collaboration has studied the $\Upsilon' \rightarrow \pi^+\pi^-\Upsilon$ reaction and finds[11]

$$BR(\Upsilon \rightarrow Unseen) < 5 \times 10^{-2}. \qquad (95\%\ \text{C.L.}) \qquad [1.3]$$

The Υ(3S)$\rightarrow\pi^+\pi^-\Upsilon$(1S) transition was also studied by the CLEO collaboration and the obtained upper limit from this analysis was quoted as[11]

$$BR(\Upsilon \rightarrow Unseen) < 8 \times 10^{-2}. \qquad (95\%\ \text{C.L.}) \qquad [1.4]$$

The detection efficiency for $\Upsilon' \rightarrow \pi^+\pi^-\Upsilon$ events in this experiment was very low and was assigned a large fractional error such that

$$\epsilon^{2S}_{CLEO} = (0.7 \pm 0.4\%)\,. \qquad [1.5]$$

The Υ(3S) measurement detection efficiency was about 10 times better, primarily because the pions tended to have more energy, but the relative error was nearly the same.

At this point it is appropriate to discuss the issue of detector size. Assume that the reaction $\Upsilon \rightarrow$X occurs, where X refers to some combination of nearly noninteracting particles, and that it is desired to detect evidence for this reaction via the $\Upsilon \rightarrow$Unseen decay channel. The particles in the state X will fit the X→Unseen hypothesis only if all of the X particles have a decay length longer than the maximum extent of the fiducial volume utilized for this search by a particular detector. Therefore 'bigger' is not 'better' in the search for $\Upsilon \rightarrow$Unseen if the unseen state involves the creation of unstable particles because the added decay length of the larger detector allows more of the unseen particles to decay into particles with stronger interaction constants and the detection of these secondary particles will veto the assignment of $\Upsilon \rightarrow$Unseen to the event in question. Because the Crystal Ball is the most compact detector to perform this experiment, it is more sensitive to the detection of events in the tail of the X→interacting particle decay distribution than the larger CUSB, CLEO and Mark II experiments. Table 1.1 compares the maximum decay lengths available to particles in the Crystal Ball and the other detectors mentioned above. The table assumes that no particle decays within the central detector may be ignored. This issue will be further discussed in regard to the search for the reaction $\Upsilon \rightarrow \gamma +$ Unseen.

Detector	Decay Length (m)
Crystal Ball	.66
LENA	.80
CUSB	1.25
Mark II	2.
CLEO	> 3

Table 1.1 Maximum decay lengths available to unseen particles in five detectors.

1.4 Rare Upsilon Decays

It is the purpose of this thesis to study the following two decay modes of the Upsilon:

a) $\Upsilon \rightarrow Unseen,$

and

b) $\Upsilon \rightarrow \gamma + Unseen,$

by means of the reaction

$$\Upsilon(2S) \rightarrow \pi^0\pi^0\Upsilon(1S). \qquad [1.6]$$

The motivation for this effort is described in detail below. Reaction (a) is clearly unobservable by means of data taken directly at the Υ(1S) center-of-mass energy and reaction (b) would suffer from a potentially higher background level. The Crystal Ball particle detector was used to gather data for this project. Approximately 44 pb^{-1} of data at the Υ(2S) center-of-mass energy was collected for the analysis of reaction (a) and a bit more ($\sim$ 57 pb^{-1}) for reaction (b).

Due to the fact that the detector is nonmagnetic, it is not possible to determine the momentum of charged particles. Since full kinematic information about the pions is needed to tag Upsilons produced via $\pi\pi$ hadronic transitions, only neutral pions could be used in this study.

The Crystal Ball analysis presented in chapter 4 gives the result

$$BR(\Upsilon \rightarrow Unseen) < 12\% \qquad (90\% \text{ C.L.}). \qquad [1.7]$$

This result is higher than either the Mark II result (eqn. [1.2]) on the J/ψ system or the result for the $\Upsilon' \rightarrow \pi^+\pi^-\Upsilon$ transition measured by CLEO (eqn. [1.3]). The larger upper limit can be attributed to the following factors:

- The statistics on the Υ are limited as compared to the J/ψ result. [1.8]
- The final result is consistent with **but not necessarily indicative of** the observation of an $\Upsilon \rightarrow$Unseen particle signal. [1.9]
- The $\pi^0\pi^0$ hadronic transition channel yields half the rate of the $\pi^+\pi^-$ channel which may be utilized by a magnetic detector such as CLEO. [1.10]
- A large dipion background which is probably attributable to a photoproduction process was observed during this study. This background adds a large contribution to the error on the $\Upsilon \rightarrow$Unseen branching ratio. [1.11]

The search for reaction (b) has produced an upper limit on the branching ratio for $\Upsilon \rightarrow \gamma +$ Unseen which is plotted in figure 1.2. As pointed out below, this sets a limit on the coupling constant of the Goldstone fermion as a function of its mass. The high energy end of this spectra also sets a limit on axion production,

$$BR(\Upsilon(1S) \rightarrow \gamma\ axion) < 2.3 \times 10^{-3} \qquad (90\% \text{ C.L.}). \qquad [1.12]$$

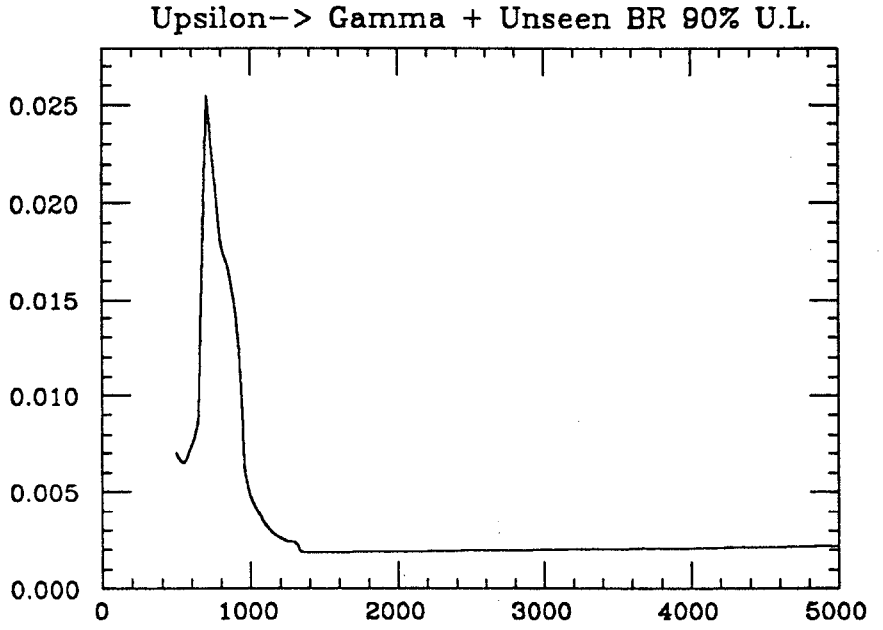

Fig. 1.2 90% C.L. for BR($\Upsilon \rightarrow \gamma +$ Unseen) versus photon energy.

1.4.1 $\Upsilon \rightarrow$ *Unseen*

Several mechanisms have been proposed which would lead to the process:

$$\Upsilon \rightarrow \textit{Unseen}.$$

For example, the following reactions would produce particles which would be unobserved in the Crystal Ball Detector.

1)	$\Upsilon \rightarrow \nu\overline{\nu}$.	(Ref. 13)	[1.13]
2)	$\Upsilon \rightarrow$ supersymmetric particle pairs .	(Ref. 9)	[1.14]
3)	$\Upsilon \rightarrow$ "mirror particles" .	(Ref. 18)	[1.15]

In reaction 1), the Upsilon couples to a virtual Z_0 particle which then decays into a neutrino pair. The coupling strength is proportional to the number of neutrino types (generations) with masses less than the Υ mass. The branching

ratio is given by[12] :

$$BR(\Upsilon \to \nu\overline{\nu}) = N_\nu \frac{9(\frac{1}{2} - \frac{2}{3}sin^2\theta_W)^2}{2(4sin^2\theta_W cos^2\theta_W)^2} \left(\frac{M_\Upsilon}{M_{Z_0}}\right)^4 BR(\Upsilon \to e^+e^-), \qquad [1.16]$$

where N_ν is the number of neutrino generations. It has been suggested[13] that this decay mode may be used to determine N_ν. Unfortunately, this branching ratio is extremely low. Taking $BR(\Upsilon \to e^+e^-)$ to be 2.5% and $sin^2\theta_W$ to be .22, gives:

$$BR(\Upsilon \to \nu\overline{\nu}) = 4 \times 10^{-6} N_\nu. \qquad [1.17]$$

The Crystal Ball branching ratio measurement implies

$$N_\nu < \frac{11. \times 10^{-2}}{(4 \times 10^{-6})} \quad (90\%\ C.L.), \qquad [1.18]$$

which results in

$$N_\nu < 3 \times 10^4\ (generations). \qquad [1.19]$$

As cosmological arguments set a limit of ≤ 4 generations,[14] this is a clear case of nonconfrontation with previous results. The determination of the BR($\Upsilon \to$Unseen) upper limit from this study will be discussed in chapter 5.

The use of hadronic transitions from the ψ' was suggested by Fayet[9] as a means of determining a lower limit on the mass of the gravitino. This particle is the partner of the graviton in supersymmetric theories. He suggests the use of decays into photinos and gravitinos via the reaction:

$$Q\overline{Q} \to \tilde{\gamma}\,\tilde{g}, \qquad [1.20]$$

where $\tilde{g}$ denotes a gravitino, which has a branching ratio[15] given by

$$\frac{BR(Q\overline{Q} \to \tilde{\gamma}\,\tilde{g})}{BR(Q\overline{Q} \to e^+e^-)} = \frac{G_{Newton} M^4_{Q\overline{Q}}}{3\alpha m^2_{\tilde{g}}}. \qquad [1.21]$$

An upper limit on the measured $Q\overline{Q}$ branching ratio into "inos", sets a lower limit on the gravitino mass. If the $Q\overline{Q}$ system mass is expressed in units of $\frac{GeV}{c^2}$,

$$m_{\tilde{g}} \geq 5.5 \times 10^{-10}\, M^2_{Q\overline{Q}} \left(\frac{BR(Q\overline{Q} \rightarrow e^+e^-)}{BR(Q\overline{Q} \rightarrow \text{ Unseen})}\right)^{\frac{1}{2}} \left(\frac{eV}{c^2}\right), \qquad [1.22]$$

where the gravitational coupling constant has the value

$$G_{Newton} = 6.7 \times 10^{-39} \left(\frac{GeV}{c^2}\right)^{-2}. \qquad [1.23]$$

The Mark II collaboration limit[10] of

$$BR(J/\psi \rightarrow Unseen) < 0.7\%, \qquad [1.24]$$

corresponds to

$$m_{\tilde{g}} > 1.5 \times 10^{-8} \left(\frac{eV}{c^2}\right). \qquad [1.25]$$

The CLEO collaboration result[11]

$$BR(\Upsilon \rightarrow Unseen) < 5\%, \qquad [1.26]$$

implies an upper limit of[11]

$$m_{\tilde{g}} > 3.0 \times 10^{-8} \left(\frac{eV}{c^2}\right). \qquad [1.27]$$

Based on a branching ratio upper limit of 12%, the limit from this analysis is

$$m_{\tilde{g}} > 2.2 \times 10^{-8} \left(\frac{eV}{c^2}\right). \qquad [1.28]$$

The idea of "mirror" particles which would be counterparts of the known particles was proposed in a paper by Lee and Yang[16] in 1956. This model was

designed to reestablish the symmetry between Left and Right which had been broken with the discovery of CP violation in Kaon decay. Ordinary (known) particles were deemed to be left-handed and mirror particles to be right-handed. According to the model, the two sets of particles do not interact via the Strong Nuclear Force or the Electroweak Force. The sets should have the same gravitational coupling, however, as well as a possible interaction via the exchange of particles which belong to both the mirror and ordinary particle schemes.[17] Neutrinos may be one example of such a particle and so vacuum transitions ("mirror oscillations") might occur between the degenerate mirror and ordinary matter states. Voloshin[18] has suggested that a measurement of BR(J/ψ→Unseen) or BR(Υ→Unseen) sets a limit on the coupling between mirror and ordinary particles. In particular, if oscillations occur between ordinary and mirror quarkonium states, he concludes:

$$\Gamma(Q\overline{Q} \rightarrow \text{ mirror } Q\overline{Q} \rightarrow \text{ unseen mirror particles}) \propto G_X^2 M_{Q\overline{Q}}^4 , \qquad [1.29]$$

where G_X is the coupling strength. On the basis of this relationship, he states that if

$$BR(\Upsilon \rightarrow Unseen) < 1\% , \qquad [1.30]$$

$G_X < 0.1 G_F$, with G_F being the Fermi constant. Presumably, this implies that the ratio of G_X and G_F is approximately given by

$$\frac{G_X}{G_F} \sim \sqrt{BR(\Upsilon \rightarrow Unseen)} . \qquad [1.31]$$

The Crystal Ball measurement of BR(Υ→Unseen) then sets the limit

$$G_X < 0.3\ G_F . \qquad [1.32]$$

A recent preprint by Glashow[19] excludes the possibility of a mirror particles by considering the effect mirror positronium would have on the well measured decay rate for normal orthopositronium.

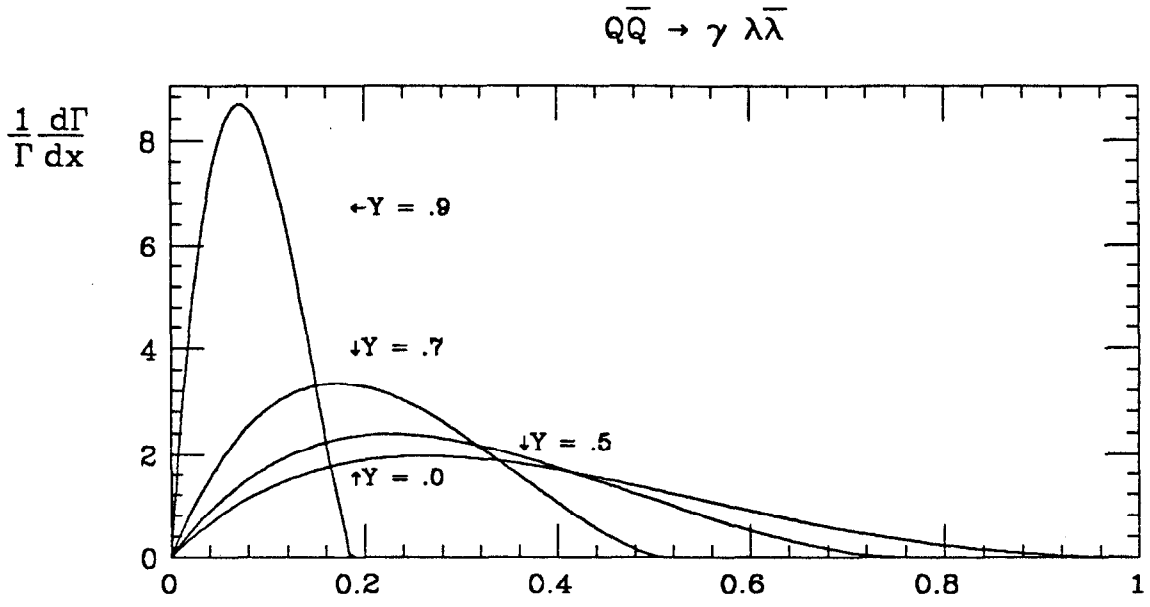

Fig. 1.3 Photon energy spectrum for the decay $\Upsilon \rightarrow \gamma\lambda\bar{\lambda}$. The abscissa is the scaled energy parameter, $x = \frac{2E_\gamma}{M_{Q\bar{Q}}}$. Spectra are shown for different values of m_λ which is parameterized as $y = \frac{2m_\lambda}{M_{Q\bar{Q}}}$ where $M_{Q\bar{Q}}$ is the mass of the quark-antiquark system. The figure is derived from ref. 29

1.4.2 $\Upsilon \rightarrow \gamma +$ *Unseen*

The observation of a fifth photon (the first four arise from π^0decays) from the tagged upsilon decay provides an additional constraint which is quite helpful in suppressing background processes. This decay mode would occur in the reactions:

1) $\Upsilon \rightarrow \gamma +$ axion (Ref. 25) [1.33]

and

2) $\Upsilon \rightarrow \gamma + \lambda\bar{\lambda}$. (Ref. 29) [1.34]

The first reaction involves the emission of a photon and an almost massless, neutral and pseudoscalar boson called the axion. The axion was postulated independently by Weinberg and Wilzcek.[20] This particle results from the breaking of a global U(1) symmetry introduced by Peccei and Quinn[21] to preserve CP

and time-reversal invariance in QCD despite the effects of instantons. In the proposed two body decay of the Upsilon into a photon and an axion, the photon energy would be given by[25]

$$E_\gamma = \frac{(M_\Upsilon^2 - m_a^2)}{2M_\Upsilon} \,. \qquad [1.35]$$

For axion masses below 1 GeV, the photon energy would be very close to $\frac{M_\Upsilon}{2}$. The standard axion is hypothesized to have a very small mass in the 100 KeV range and a long lifetime ($> 10^{-2}s$). The axion interacts very weakly with ordinary matter and therefore a long-lived axion would be unseen by a standard particle detector. The branching ratios of $c\bar{c}$ and $b\bar{b}$ states to an axion + photon have been collected in ref. 22. They are

$$\frac{BR(J/\psi \rightarrow \gamma + a)}{BR(J/\psi \rightarrow \mu^+\mu^-)} = \frac{G_F m_c^2}{\sqrt{2}\pi\alpha_{em}} \quad x^2, \qquad [1.36]$$

and

$$\frac{BR(\Upsilon \rightarrow \gamma + a)}{BR(\Upsilon \rightarrow \mu^+\mu^-)} = \frac{G_F m_b^2}{\sqrt{2}\pi\alpha_{em}} \quad \frac{1}{x^2}, \qquad [1.37]$$

where a refers to the axion, m_c and m_b to the respective quark masses and the free parameter x is the ratio of the vacuum expectation values of two Higgs fields in the theory. Because this parameter appears in the numerator in the $c\bar{c}$ case and in the denominator in the $b\bar{b}$ case, the product of equations [1.36] and [1.37] yields a branching ratio prediction which is independent of the x factor:

$$BR(J/\psi \rightarrow \gamma + a) \times BR(\Upsilon \rightarrow \gamma + a) = (1.4 \pm 0.3) \times 10^{-8} \,, \qquad [1.38]$$

as quoted in ref. 22 after substitution of the appropriate values for m_c, m_b, and the leptonic branching ratios.

The reactions $e^+e^- \rightarrow J/\psi$ and $e^+e^- \rightarrow \Upsilon$ have been used to measure the upper limit for BR($Q\overline{Q}\rightarrow\gamma+$ a), assuming a long-lived axion, at the 90%

confidence level:

$$\mathrm{BR}(J/\psi \rightarrow \gamma + axion) < 1.4 \times 10^{-5} \quad \text{(Crystal Ball)} \quad \text{(Ref. 23)} \quad [1.39]$$

and

$$\mathrm{BR}(\Upsilon \rightarrow \gamma + axion) < 9. \times 10^{-4} \quad \text{(LENA)} \quad \text{(Ref. 24)} \quad [1.42]$$

$$\mathrm{BR}(\Upsilon \rightarrow \gamma + axion) < 3.5 \times 10^{-4} \quad \text{(CUSB)} \quad \text{(Ref. 25)} \quad [1.40]$$

$$\mathrm{BR}(\Upsilon \rightarrow \gamma + axion) < 3.0 \times 10^{-4} \quad \text{(CLEO)} \quad \text{(Ref. 26)} \quad [1.41]$$

and via the $\pi^0\pi^0$ hadronic transition, this experiment obtains:

$$\mathrm{BR}(\Upsilon \rightarrow \gamma + axion) < 2.3 \times 10^{-3}\,. \quad [1.43]$$

If the known branching ratio for $J/\psi \rightarrow \mu^+\mu^-$ is inserted in equation [1.36], a 90% C.L. upper limit on x can be derived from the Crystal Ball J/ψ result.[23]

$$x < 0.6\,. \quad [1.44]$$

The product of the Crystal Ball J/ψ axion limit (eqn. [1.39]) and either of the CESR experiment limits (eqns. [1.40] or [1.41]) yields a number below the theory limit of equation [1.38] and thus the long-lived axion is excluded by experiment. It is possible to consider a heavy, shorter-lived axion however. The mass of the axion has been estimated to be[20]

$$m_a \sim 25N\left[x + \frac{1}{x}\right] keV \quad [1.45]$$

where N is the number of quark generations. This equation implies that $m_a \geq 150\ keV$ for $N = 3$. The axion decay rates into photon pairs and e^+e^- pairs are also given in ref. 22 as

$$\tau_{\gamma\gamma} \sim 0.7 \times 10^{-5}\left[\frac{1\ MeV}{m_a}\right]^5 \quad [1.46]$$

and for axions with mass $\geq m_e$,

$$\tau_{ee} = \frac{10^{-9} MeV^3}{m_a^2 (m_a^2 - 4m_e^2)^{\frac{1}{2}}} \quad x^2 \; sec. \qquad [1.47]$$

If the axion has mass below 1 MeV it will not decay via pair production and so the decay rate of equation [1.46] will apply. In this case the axion lifetime will be $> 10^{-5}$ sec. Axions which live this long will decay outside the calorimetric volume of the detectors represented in the above measurements and so are excluded by experiment.

The possibility that axions may be more massive than 1 MeV has become more intriguing with the recent results from two nuclear physics experiments at GSI Darmstadt involving the creation of subcritical (Z=163) to supercritical (z=188) nuclear states via heavy ion collisions.[27] If a nucleus is supercritical ($Z \geq 173$), it is energetically more favorable to create an e^+e^- pair out of the vacuum than to leave the lowest-lying orbit unfilled. The EPOS and Orange Spectrometers looked for the positron which would be created in this process. Theory predicted that the positron energy and intensity distribution would be an extremely strong function of Z. Instead a peak in the positron energy distribution was found at constant value of 300 keV regardless of Z with a narrow width of 70 keV. The narrowness of the peak may indicate that a relatively long-lived, hitherto unknown boson may have been created in these experiments with mass of approximately 1.6 MeV ($2m_e + 2 \times .3MeV$).* This particle might be an axion.

If the axion does have mass greater than 1 MeV, it is interesting to investigate what its properties might be in the minimal Peccei-Quinn model. A starting point is equation [1.45] which implies that

$$x^2 \sim \frac{5.6 \times 10^{-3}}{m_a^2} \quad MeV^2, \qquad [1.48]$$

---

* I am indebted to Kai Königsman for elucidating some of the implications of these measurements with regard to axion production.

for N=3. Equation [1.47] then becomes

$$\tau_{ee} = \frac{5.6 \times 10^{-12} MeV^5}{m_a^4 (m_a^2 - 4m_e^2)^{\frac{1}{2}}} \quad \text{sec.} \qquad [1.49]$$

In order to evaluate the fraction of $m_a > 1\,MeV$ axions that will be detectable by a given experiment, it is necessary to consider the mean decay length for these particles which is given by

$$l = \gamma c \tau_{ee} \quad , \qquad [1.50]$$

where γ refers to the boost of the axion. γ is just

$$\gamma = \frac{E_a}{m_a} \quad , \qquad [1.51]$$

where E_a is the total energy of the axion in the laboratory frame. Because $E_a = M_\Upsilon - E_\gamma$, equations [1.35] and [1.51] may be substituted into equation [1.50] to yield the mean decay length as a function of axion mass $> 1\ MeV$,

$$l = \gamma c \tau_{ee} = \frac{M_\Upsilon^2 + m_a^2}{M_\Upsilon} \frac{8.4 \times 10^{-4}}{m_a^5 (m_a^2 - 4m_e^2)^{\frac{1}{2}}} \quad (meters). \qquad [1.52]$$

The fraction of axions that will have not decayed after traversing s meters is given by

$$\epsilon = exp\frac{-s}{l} \quad . \qquad [1.53]$$

For a 1.6 MeV axion, l is .62 meters. From table 1.1 and equation [1.52] the fraction of detectable axions for the Crystal Ball, LENA, CUSB and CLEO experiments can be determined to be .34, .27, .13 and .01 respectively. If the LENA, CUSB, CLEO and Crystal Ball limits for light axions are divided by this

detection efficiency factor, the upper limits in equations [1.40]-[1.43] become:

$$BR(\Upsilon \rightarrow \gamma + axion_{1.6MeV}) < 2.7 \times 10^{-3} \quad (CUSB) \qquad [1.54]$$

$$BR(\Upsilon \rightarrow \gamma + axion_{1.6MeV}) < 3.3 \times 10^{-3} \quad (LENA) \qquad [1.55]$$

$$BR(\Upsilon \rightarrow \gamma + axion_{1.6MeV}) < 6.8 \times 10^{-3} \quad \text{(Crystal Ball)} \qquad [1.56]$$

$$BR(\Upsilon \rightarrow \gamma + axion_{1.6MeV}) < 3.0 \times 10^{-2} \quad (CLEO) \qquad [1.57]$$

The theoretical prediction is obtained by substituting the estimate for the axion mass (eqn. [1.48]) into equation [1.37].

$$\frac{BR(\Upsilon \rightarrow \gamma + a)}{BR(\Upsilon \rightarrow \mu^+\mu^-)} = \frac{G_F m_b^2}{\sqrt{2}\pi\alpha_{em}} \quad \frac{m_a^2}{5.6 \times 10^{-3}\ MeV}, \qquad [1.58]$$

Thus the predicted branching ratio is

$$\text{BR}(\Upsilon \rightarrow \gamma + a) = 3.1 \times BR(\Upsilon \rightarrow \mu^+\mu^-) = 7.8 \times 10^{-2} \qquad [1.59]$$

where $2.5 \pm .4\%$[30] was used for the Υ leptonic branching ratio. This value is an order of magnitude higher than the measured upper limit of equation [1.56]. The assumption of equation [1.48] thereby excludes a 1.6 MeV axion by the present experiment. It is possible once again to eliminate the parameter x by taking the product of equations [1.36] and [1.37]. Mukhopadhyay and Zehnder[28] utilize this product to derive a limit which is independent of x in the Peccei-Quinn model. They find that short-lived axions obey the relation

$$\frac{\tau_a}{m_a} < 2.6 \times 10^{-13}\ \text{s}\ MeV^{-1}, \qquad [1.60]$$

when they assume detector decay lengths of 30 cm. This limit is a factor of 2-10 larger given the actual sizes (table 1.1) of the detectors involved in this search. In any case, an axion that decays in less than a nanosecond or so will probably not be detectable by a typical size colliding beam experiment. It is also possible

that the axion coupling strength to b and c quarks is different and thus that the x used in equation [1.36] is not the same as the x in equations [1.37] and [1.45]. Such an effect could invalidate the above analysis.

The second $\Upsilon \rightarrow \gamma +$ Unseen reaction under consideration in this thesis was proposed by Nachtmann[29] to detect the existence of very weakly interacting goldstone fermions. The three body decay of the Upsilon particle produces a photon energy spectra which is dependent on the mass of the goldstone fermions, m_λ (see figure 1.3) . A failure to observe a peaked photon energy spectrum above a given energy value may be used to set an upper limit on the mass of the goldstone fermion. Nachtmann states that the decay rate of $Q\overline{Q}$ into a photon and a pair of goldstone fermions can be normalized by the electronic decay width of the $Q\overline{Q}$ state as follows:

$$\frac{\Gamma(Q\overline{Q} \rightarrow \gamma + \lambda + \lambda)}{\Gamma(Q\overline{Q} \rightarrow e^+e^-)} = \frac{\kappa^2 M_{Q\overline{Q}}^8}{2^{10}\pi^3\alpha} \cdot K(y) \qquad [1.61]$$

where $M_{Q\overline{Q}}$ is the $Q\overline{Q}$ system mass and the kinematic factor K(y) is given by the equation

$$K(y) = (\frac{22}{75} - \frac{82}{225}y^2 - \frac{164}{225}y^4 - \frac{7}{120}y^6 - \frac{3}{160}y^8 - \frac{3}{64}y^{10}) \cdot (1-y^2)^{\frac{1}{2}} + y^6 \cdot (1 - \frac{1}{24}y^2 + \frac{1}{80}y^4\frac{3}{64}y^6) \cdot \ln\left(\frac{1+(1-y^2)^{\frac{1}{2}}}{y}\right) , \qquad [1.62]$$

with $y = \frac{2m_\lambda}{M_{Q\overline{Q}}}$ in the range $0 \leq y \leq 1$. The functional form of K(y) is plotted in figure 1.4.

Equation [1.62] implies that a limit can be placed on the coupling constant of the Goldstone fermion. Manipulation of this equation leads to:

$$\kappa^2 = \frac{2^{10}\pi^3\alpha}{M_{Q\overline{Q}}^8 K(y)} \cdot \frac{BR(\Upsilon \rightarrow \gamma\lambda\lambda)}{BR(\Upsilon \rightarrow e^+e^-)} . \qquad [1.63]$$

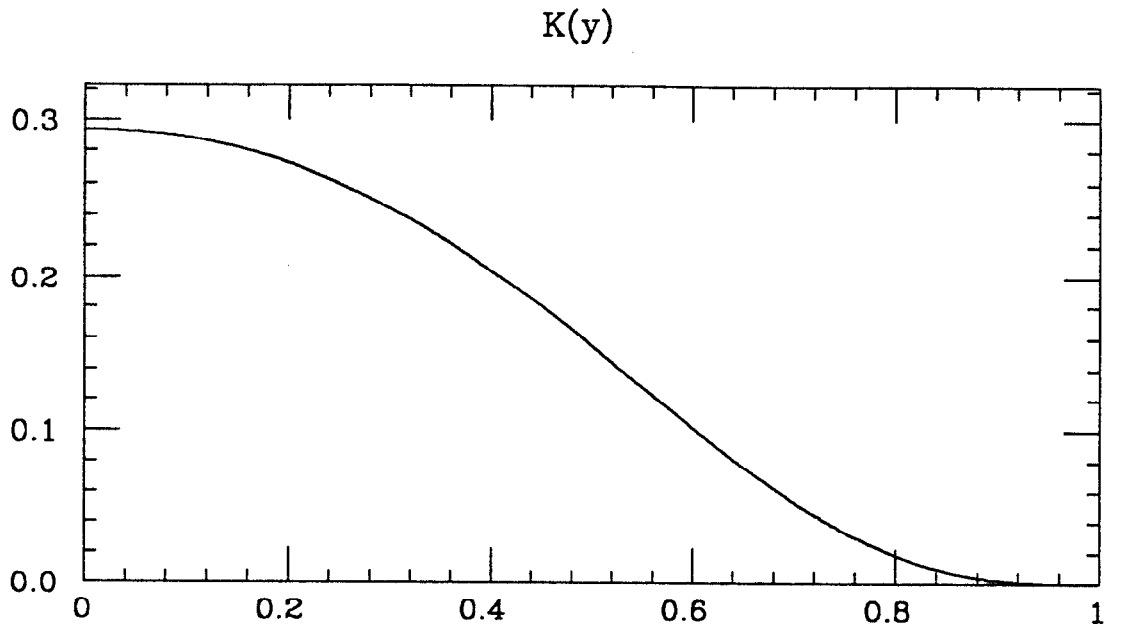

Fig. 1.4 Kinematic factor K(y) (from eqn. [1.62]) as a function of the mass ratio $y = 2m_\lambda/M_{Q\overline{Q}}$.

By figure 1.3, a minimum of roughly half of the Goldstone fermion events with $m_\lambda < .7\ m_b$ should be associated with photons of energy greater than 1 GeV (x= .2). The minimum value of K(y) in the interval $0 \leq y \leq .7$ is .05. Therefore the upper limit on κ can be derived from the present measurement of $\mathrm{BR}(\Upsilon \rightarrow \gamma + Unseen) < 2.3 \times 10^{-3}$ for $E_\gamma > 1\ GeV$.

$$\kappa = \left[\frac{2^{10}\pi^3\alpha}{m^8_{Q\overline{Q}} K(y)} \cdot \frac{2 \times \mathrm{BR}(\Upsilon \rightarrow \gamma + \text{ Unseen })}{\mathrm{BR}(\Upsilon \rightarrow e^+e^-)} \right]^{\frac{1}{2}}, \qquad [1.64]$$

$$< 3.6 \times 10^{-3} \quad GeV^{-4}$$

assuming $\mathrm{BR}(\Upsilon \rightarrow e^+e^-) = 2.5 \pm .4\ \%$[30] .

The supersymmetric models used by Fayet[9] and Nachtmann[29] both generate massive gauge particles (gravitinos or goldstone fermions) by means of spontaneous supersymmetry breaking. The mass of the gauge particles can be related to the mass scale, Λ_{ss}, at which spontaneous supersymmetry breaking

occurs. In the Fayet model, unseen decays of the Upsilon are due to the process, $\Upsilon \rightarrow$gravitino + antiphotino, or $\Upsilon \rightarrow$antigravitino + photino. If the ratio of unseen Upsilon decays to electronic decays is given by the upper limit:

$$R_F \leq \frac{U.L.\ \mathrm{BR}(\Upsilon \rightarrow Unseen)}{\mathrm{BR}(\Upsilon \rightarrow e^+e^-)} \quad , \qquad [1.65]$$

and the photino is assumed to be massless, the lower limit on Λ_{ss} may be estimated by means of[31]

$$\Lambda_{ss} \geq \left[\frac{M_\Upsilon^4}{4\pi\alpha R_F} \left(1 - \frac{m_{\tilde{g}}^2}{M_\Upsilon^2} \right) \right]^{\frac{1}{4}} \quad , \qquad [1.66]$$

where $m_{\tilde{g}}$ is the gravitino mass. The coupling used in the Nachtmann model is related to Λ_{ss} by $\kappa = \Lambda_{ss}^{-4}$. The upper limit for BR($\Upsilon \rightarrow \gamma +$ Unseen) may then be used to set the lower limit

$$\Lambda_{ss} \geq \left[\frac{M_\Upsilon^8}{2^{10}\pi^3\alpha R_N} \cdot K\left(\frac{2m_\lambda}{M_\Upsilon} \right) \right]^{\frac{1}{8}} \quad , \qquad [1.67]$$

where m_λ is the goldstone fermion mass, $K(\frac{2m_\lambda}{M_\Upsilon})$ is defined in eqn. [1.62], and R_N is given by

$$R_N = \frac{U.L.\ BR(\Upsilon \rightarrow \gamma + Unseen)}{BR(\Upsilon \rightarrow e^+e^-)} \quad . \qquad [1.68]$$

The resulting lower limits on Λ_{ss} for this analysis as a function of gravitino or goldstone fermion mass are shown in figure 1.5.

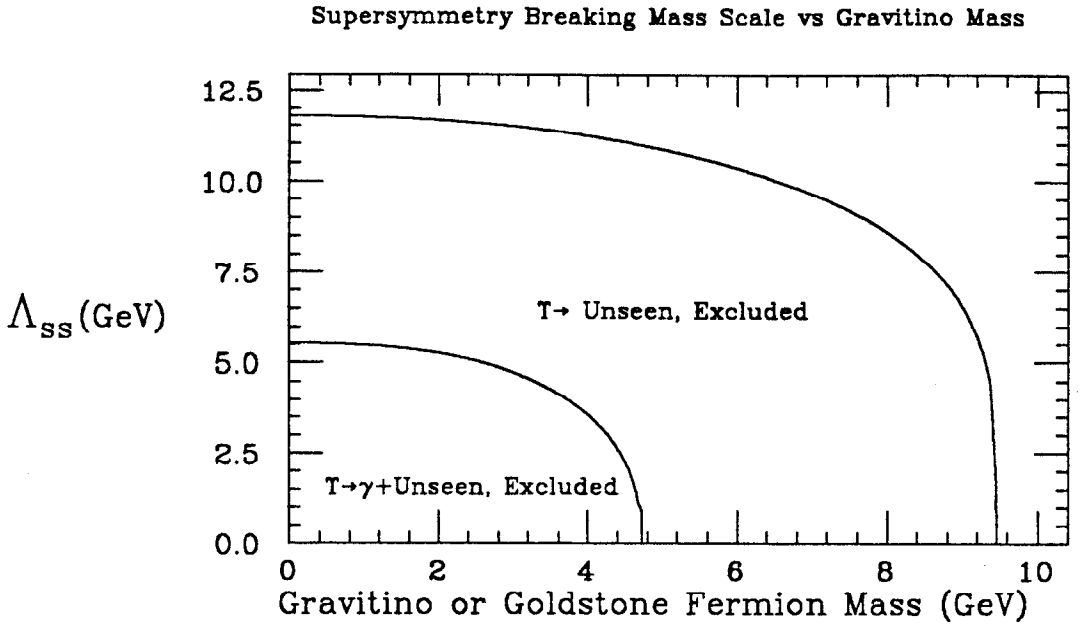

Fig. 1.5 Lower limit on Λ_{ss} as a function of gravitino or goldstone fermion mass.

1.5 Summary

The production of tagged Upsilons via the $\Upsilon' \rightarrow \pi^0\pi^0\Upsilon$ hadronic transition allows the detection of several speculative physics processes involving conjectured or weakly coupled interactions. The approach used in this thesis contributes a new data analysis channel to this study. The detection and analysis efficiency for the process $\Upsilon \rightarrow$Unseen is higher than for the previously published result and the smaller volume may allow the tagging of nearly noninteracting particles which would decay within a larger detector volume. Chapter 2 of this thesis will describe the experimental apparatus involved in this study. Chapter 3 details the initial data acquisition and analysis of Crystal Ball data. Chapter 4 will cover the specific data analysis involved in the search for $\Upsilon \rightarrow$Unseen, and chapter 5 will review the analysis of $\Upsilon \rightarrow \gamma +$ Unseen. Final conclusions from this work will be offered in chapter 6.

References

1) J. Augustin, *et al. Phys. Rev. Lett.* **33**, 1406 (1974)
   J. Aubert, *et al. Phys. Rev. Lett.* **33**, 1404 (1974)
2) R. Barnett, *Phys. Rev. Lett.* **36**, 1163 (1976)
3) E. Eichten and K. Gottfried, *Phys. Lett.* **66**, 286 (1977)
4) S.W. Herb, *et al. Phys. Rev. Lett.* **39**, 252 (1977)
   W.R. Innes, *et al. Phys. Rev. Lett.* **39**, 1240 (1977)
   K. Ueno, *et al. Phys. Rev. Lett.* **42**, 486 (1979)
5) Ch. Berger, *et al. Phys. Lett.* **76B**, 243 (1978)
   C. Darden, *et al. Phys. Lett.* **76B**, 246 (1978)
   J. Bienlein *et al. Phys. Lett.* **78B**, 360 (1978)
   C. Darden *et al. Phys. Lett.* **78B**, 364 (1978)
6) D. Andrews *et al. Phys. Rev. Lett.* **44**, 1108 (1980)
   T. Böhringer *et al. Phys. Rev. Lett.* **44**, 1110 (1980)
7) D. Andrews *et al. Phys. Rev. Lett.* **45**, 219 (1980)
   G. Finocchiaro *et al. Phys. Rev. Lett.* **45**, 222 (1980)
8) A. Silverman, Recent Results from CESR, Proc. of the 1981 Int. Symp. on Lepton and Photon Interaction at High Energies, Ed. W. Pfeil (Physikalisches Institut Universität Bonn, Bonn, 1981).
9) P. Fayet, *Phys. Lett.*,**84B**, 421 (1979)
10) The Mark II result is quoted as a private communication in ref. 9.
11) D. Besson, *Phys. Rev. D*, **30**, 1433 (1984)

12) This formula was brought to my attention by Boris Kayser. It is derivable from a more general formula (2.17)

$$\frac{\Gamma(Q\overline{Q} \to Z_0 \to \nu\overline{\nu})}{\Gamma(Q\overline{Q} \to e^+e^-)} = \frac{G_F^2 M_{Q\overline{Q}}^4}{64\pi^2\alpha^2 {e_Q}^2}(1 - 4 \mid e_Q \mid sin^2\theta_W)^2 \times N_\nu$$

where e_Q is the quark charge, found in
J. Ellis, Proc. of Summer Institute on Particle Physics, 1978. Ed. M. Zipf, SLAC Report No. 215, 1978.

13) J. Rich and D.R. Winn, *Phys. Rev. D.*, **14**, 1283 (1976)

T. Ghosh, *J. Phys. G*, **2**, 471 (1976)

V. Barger and D.V. Nanopoulos, *Nucl. Phys.*, **B124**, 426 (1977)

J. Ellis, Proc. of Summer Institute on Particle Physics, 1978. Ed. M. Zipf, SLAC Report No. 215, 1978.

G. Barbiellini, Proc. 14'th Rencontre de Moriond, Ed. J. Tran Thanh Van, Editions Frontières, 1979.

V.A. Novikov and M.A. Shifman, *Z. Phys. C*, **8**, 43 (1981)

V. Barger, W. Keung and R. Phillips, *Phys. Rev. D.*,**25**, 677 (1982)

14) D. Schramm and G. Steigman, *Phys. Lett.*, **141B**, 337 (1984)

15) C. Newman Holmes, Crystal Ball Note 414, Aug. 83,SLAC.

16) T.D. Lee and C.N. Yang, *Phys. Rev.*, **104**, 254 (1956)

17) I. Yu. Kobzarev, *et al. Soviet J. of Nucl. Phys.*, **3**, 837 (1966)

18) Voloshin is referred to in L.B. Okun, "On a Search for Mirror Particles", ITEP-149-1983, Moscow, 1983.

M. Voloshin, "Remarks on $b\bar{b}$ and B Physics", ARGUS collaboration Meeting at DESY, Sep. 26,1985.

19) S. L. Glashow, "Positronium vs. the Mirror Universe," Nov. 1985, Harvard University, HUTP-85/A079.

20) S. Weinberg, *Phys. Rev. Lett.*, **40**, 223 (1978).

F. Wilczek, *Phys. Rev. Lett.*, **40**, 279 (1978).

21) R. D. Peccei and H.R. Quinn, *Phys. Rev. Lett.*, **38**, 1440 (1977).

22) F. Porter and K. Kõnigsmann, *Phys. Rev. D.*, **25**, 1993 (1982)

23) C. Edwards, *et al. Phys. Rev. Lett.*, **48**, 903 (1982)

24) B. Nicyporuk, *et al. Z. Phys*, **C17**, 197 (1983)

25) M. Sivertz, *et al. Phys. Rev. D.*, **26**, 717 (1982), erratum: *Phys. Rev. D.*, **26**, 2534 (1982)

26) M. Alam, *et al. Phys. Rev. D.*, **27**, 1665 (1983)

27) J. Schweppe, *et al.*, *Phys. Rev. Lett.*, **51**, 2261 (1983).

M. Clemente, *et al.*, *Phys. Lett.*, **137B**, 41 (1984).

28) N. Mukhopadhyay and A. Zehnder, "Model Independent Constraints on Axion Parameters from the Radiative J/ψ and Υ Decays," Sub. to Phys. Lett., SIN preprint SIN-PR-86-02, Jan. 86.

29) O. Nachtmann, A. Reiter, and M. Wirbel, *Z. Phys C*, **23**, 199 (1984)

30) D. Prindle, Ph.D. Thesis, "Measurement of the Resonance Parameters of the Υ and Υ' Mesons," Carnegie-Mellon U., 1985. Unpublished.

31) This formula is based on eqn. 18 in ref. 9 where $\Lambda_{ss} = d^{-2}$, and the factor $(1 - \frac{m_{\tilde{g}}^2}{M_\Upsilon^2})$ arises from two body phase space. M. Peskin, private communication.

Chapter 2

The Crystal Ball Detector at DORIS II

2.1 The Move to DORIS II

The Crystal Ball experiment was originally located at the SPEAR e^+e^- storage ring at SLAC where it had been installed in 1978. The construction and initial assembly of the detector are extensively described in ref. 1. At SPEAR, the Crystal Ball had been able to clarify the spectroscopy of the charmonium system (See ref. 2 and 3 for details). For this reason and because it seemed possible to transport the detector due to its small size, a joint proposal by members of the (SPEAR) Crystal Ball and LENA collaborations was made to take data on the Upsilon system at the upgraded DORIS II storage ring. The proposal was approved by the DESY management in September, 1981.

The logistics involved in transporting the detector components to Germany were impressive. The detector was taken out of SPEAR in late December 1981. Photomultiplier tubes were removed thereafter and each hemisphere was separately crated. Because the NaI crystals within each hemisphere are hygroscopic and very fragile as well, the crates were designed to maintain an internal nitrogen atmosphere and to cushion against shocks. Two semitrailers were purchased to transport the detector components. One of them was filled with the computer hardware, electronic racks and other electrical equipment used in the data acquisition system. This trailer was sent via container ship to Hamburg. The other

Fig. 2.1 The Semitrailer containing the Crystal Ball being loaded into a C-5A at Travis Air Force Base. (April 1982)

trailer, which was fitted with special air-shocks, carried the crates containing the two hemispheres. It was also filled with equipment and gas cylinders used to monitor and maintain the crystal humidity and temperature as well as the gas pressure within the hemispheres. In April 1982, this trailer was skillfully loaded onboard an Air Force C-5A based at Travis Air Force Base north of San Francisco (See fig. 2.1) and flown nonstop (utilizing in-air refueling) to Rhein-Main Air Force Base in Frankfurt, Germany. From there the trailer was driven north to Hamburg. The detector reassembly was completed in June 1982 in time for the start-up of DORIS II.

2.2 Experimental Overview

The DORIS II e^+e^- storage ring became operational in June 1982 following modification of the original DORIS to increase the available energy and luminosity as well as to lower the power consumption. This was accomplished by converting the device from a double to a single ring configuration and by replacing magnets and RF power supplies. In addition, the specific luminosity of the machine was enhanced by inserting mini-β final focus magnets in the two interaction regions. Stored current was initially limited to 10 mA per beam. This restriction was gradually overcome as the machine control parameters were better understood, the vacuum improved and the final focus system was more finely tuned. By the end of the $\Upsilon(2S)$ running in the winter of 1984, currents of 50 mA per beam were routinely injected into the machine. This corresponds to an integrated daily luminosity of 1000 nb^{-1} compared to approximately 100 nb^{-1} per day achieved with the lower currents. The record was 1600 nb^{-1} delivered in a single day at the $\Upsilon(2S)$ center of mass energy.

Figure 2.2 schematically identifies the major components of the storage ring and its feeder systems. Linac I provides electrons of up to 40 MeV to the DESY synchrotron. Similarly, Linac II supplies 400 MeV positrons which are first accumulated in the small PIA ring before transfer to the synchrotron. The DESY

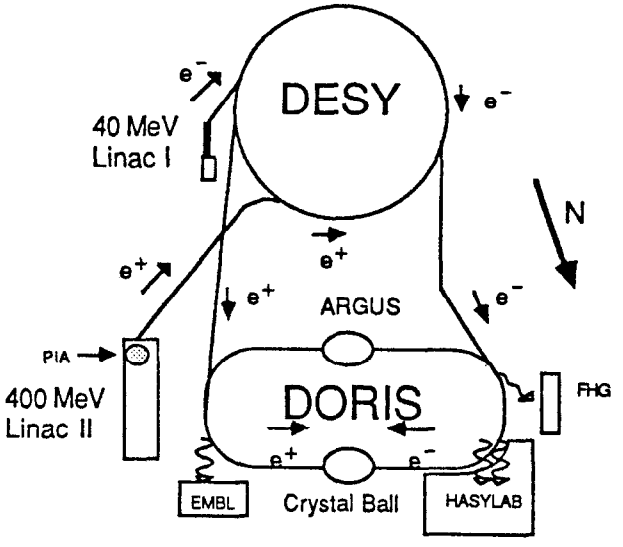

Fig. 2.2 DORIS II storage ring and feeder systems. Linac I and II supply electrons and positrons to the DESY synchrotron which accelerates them to the DORIS II injection energy.

ring ramps electrons and positrons up to either the DORIS II or the PETRA e^+e^- colliding ring injection energies before transferring the particles. The Crystal Ball particle detector is installed in the north interaction region of DORIS II. The ARGUS experiment occupies the south pit. The 300 m circumference storage ring is housed in a large experimental hall which provides easy access to both experiments. Portals in the beam line provide synchrotron radiation from the stored beams to the HASYLAB, FHG and EMBL facilities which perform materials research. The particle detector groups operate the storage ring in single bunch mode while taking data. The beams have a gaussian distributed bunch length of about 2 cm while the horizontal (vertical) dispersion is on the order of $1(\ll 1)$ mm.

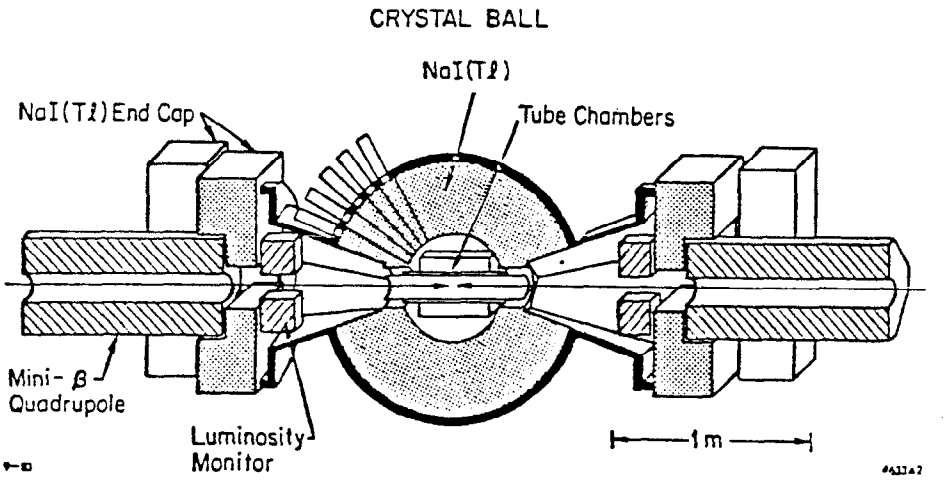

Fig. 2.3 Crystal Ball Detector components in DORIS II configuration.

2.3 The Crystal Ball Detector

The Crystal Ball experiment is a nonmagnetic device which utilizes a NaI scintillator array for particle detection and identification. The array is formed by a projective geometry stacking of 672 NaI scintillator crystals within two separable hemispherical shells. Tube chambers for charged particle tagging occupy most of the volume between the beampipe and the inner radius of the two hemispheres. An endcap array increases the covered solid angle from 93% to 98%. A luminosity monitor is located on the beampipe between the tube chambers and the endcaps. Time-of-flight (TOF) plastic scintillator counters provide partial coverage as an aid to cosmic ray rejection. Figure 2.3 illustrates the major components of the detector with the exception of the TOF counters.

2.3.1 *The Central Detector*

The sodium iodide crystal array provides calorimetric coverage of 93% of 4π steradians. Within that volume, the crystal segmentation provides information

on the direction and nature of the particles traversing the detector. The main ball is composed of two hemispherical shells which provide mechanical support and environmental protection for the fragile and hygroscopic sodium iodide crystals. The shells may be separated vertically to a distance of six feet in order to provide access to the tube chambers. This feature is also useful in preventing unnecessary exposure of the scintillator crystals to harmful radiation in the plane of the storage ring during stored beam injection. When the ball is in the closed position for data taking, a gap of .5 mm remains between the shells at the inner radius of 10 inches. This gap increases to 8 mm at the outer radius of 26 inches. The inner radius dome and equator plane washer of each hemispherical "can" was formed of $\frac{1}{16}$ inch thick stainless-steel. The outer radius dome was constructed from $\frac{7}{8}$ inch thick aluminum. The radial and planar geometry of the cans was altered by a hexagonal cut made at both the inner and outer radii to allow enough room for the beam pipe to pass through the main ball. Crystals which lie on the border formed by this cut are said to be in the "tunnel region" and are referred to as "tunnel modules."

Fabrication of the NaI crystals was performed in collaboration with the Harshaw Chemical Company at their plant in Solon, Ohio.[1] The crystals are stacked according to an icosahedral geometry. That is to say that the crystals form 20 major triangular faces. A complete "major triangle" comprises 36 NaI modules. Because of the beampipe cut, four of the major triangles are incomplete. Each major triangle is further subdivided into four "minor triangles." Minor triangles contain 9 crystals. Figure 2.4 illustrates the various subdivisions of the central detector into the major triangle, minor triangle and individual module levels.

The crystals are formed of thallium doped sodium iodide scintillators. Each NaI module is 16 inches long which presents 16 radiation lengths of material to electromagnetically showering particles. The modules were individually machined to form triangular prisms having 2 inch edges at the inner face and 5 inch edges at the outer face. Each crystal was polished or sanded as necessary

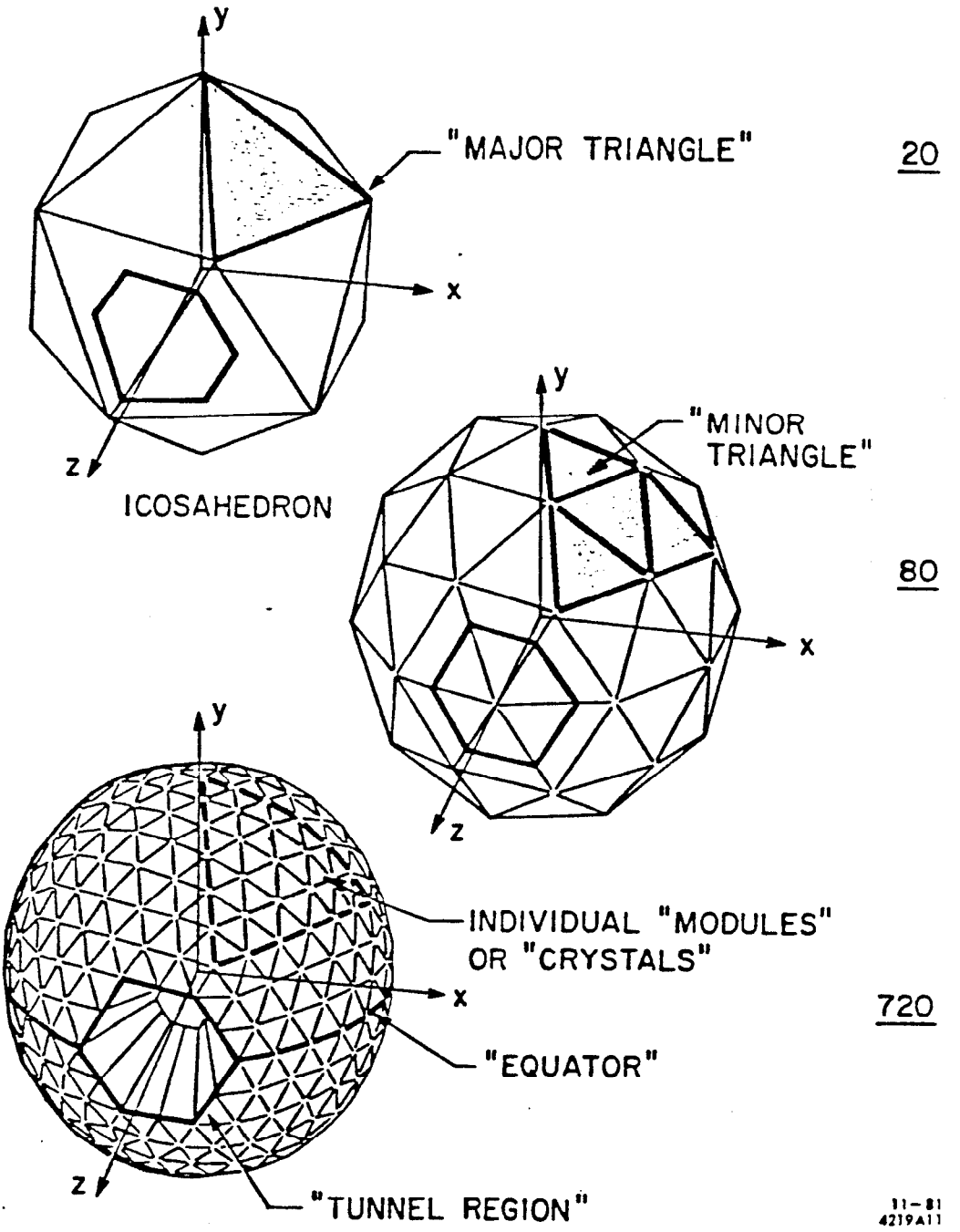

Fig. 2.4 Geometrical structures employed in Crystal Ball nomenclature. The top figure indicates the twentyfold division of the ball into the major triangle which contains 36 NaI modules. The next division is the minor triangle which contains 9 modules. Finally, the individual module level is shown in the bottom figure. Note the tunnel region which borders the beam pipe opening.

to provide uniform light output as a cesium source was transported along its length. The modules are optically isolated from one another by means of paper and mylar foil. Photomultiplier tubes view each crystal through a .5 inch window separated by a two inch air-gap from its outer face.

The output from each photomultiplier tube was integrated by means of RC circuits and the result presented to the trigger system electronics. A decision to trigger the experimental data acquisition caused the photomultiplier tube signal levels to be recorded by a PDP 11 controlled scanning ADC. The Crystal Ball data acquisition system has been extensively described.[4] Because of the difficulty of detecting the $\Upsilon' \rightarrow \pi^0\pi^0\Upsilon$ transition when $\Upsilon \rightarrow$ Unseen, a special trigger, called the NMULT trigger, was installed in order to sample this process. Appendix A describes the Crystal Ball trigger system.

The energy resolution for electromagnetically showering particles (photons, electrons and positrons) is given by

$$\frac{\sigma(E)}{E} = \frac{2.7 \pm 0.2\%}{E^{\frac{1}{4}}}$$

when the particle energy is measured in GeV. The angular resolution is between 1 and 3 degrees with the higher directional uncertainty at low energy.

2.3.2 *Tube Chambers*

The Crystal Ball Tube Chamber system is used in this analysis to exclude the misidentification of charged particles as photons. The system consisted of 3 double layers of proportional tubes with 50μ diameter stainless-steel wires to provide charge division readout. Figure 2.5 presents a cut-away view of the tube chamber system. The tube chambers are situated in the cavity between the beampipe and the inner radius domes formed by the hemispherical NaI cans. The inner, middle and outer double layers covered 98%, 96% and 75% of 4π solid angle respectively. Two configurations were employed during the course of

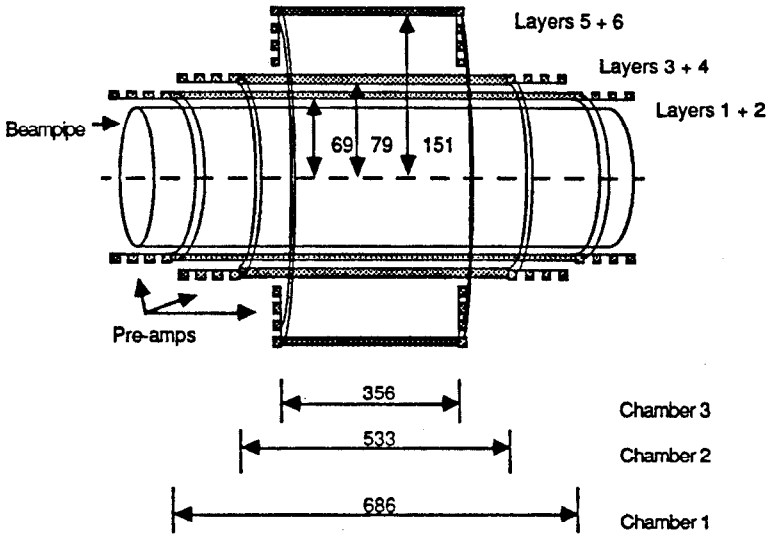

Fig. 2.5 The Crystal Ball tube chamber system. Three double layers are seen. Dimensions are given in millimeters. Drawing is not to scale.

the $\Upsilon(2S)$ data taking. The initial configuration consisted of proportional tubes within 3 mil thick aluminum cylindrical walls. "Magic gas" (20% Isobutane, 4% Methylal, .25% Freon 13B1, and 75% Argon) was utilized to produce large pulses regardless of the ionization deposited. This configuration had been used at SPEAR in the Fall of 1981 and operated unchanged at DORIS II from July 1982 to June 1983.

It was decided to replace the inner two double layers because of problems encountered with the deposition of organic compounds on the wires. These problems lead to a degradation of the high voltage plateau and hence inefficient operation of the chambers. The second configuration was installed in June of 1983. The inner two chamber double layers, which had experienced the greatest decline in performance, were replaced. The wall thickness of the new chambers was increased to 7 mils of aluminum to make the system more rugged. In the initial configuration, each double layer had employed a different diameter tube

size. The tube (outer) diameter was standardized at .236 inches in the new configuration. Because of this, the number of tubes in the inner double layer was reduced from 80 per layer to 64. The number of tubes in the middle double layer was also reduced to 76 per layer from the original 80. The outer double layer remained unchanged with 160 tubes in each layer. The gas was then changed from magic gas to a 20% CO_2, 1% Methane, and 79% Argon mixture.[5] This operating gas does not create organic depositions during operation of the chambers.

2.3.3 *Endcaps*

The presence of mini-β final focus quadrupole magnets in the DORIS II interaction regions necessitated a redesign of the Crystal Ball endcap array from its configuration at SPEAR. The previous design utilized a nearly projective stacking of 30 hexagonal NaI(Tl) crystals. The crystals were 20 inches long with 2 inch hexagonal faces and each crystal was individually encased in a 20 mil thick steel can. Two magnetostrictive spark chamber layers were installed in front of the endcap crystals in order to tag charged particles. See fig. 2.6a.

The DORIS II design accommodated the octagonal mini-β magnets, which were located close in to the central detector, by horizontally and vertically stacking the endcap crystals around them. See fig. 2.6b. This configuration provides for 20 crystals in each endcap arranged so that most of the available solid angle is covered by approximately 10 radiation lengths of NaI. The projective geometry and charged particle tagging of the SPEAR design was lost due to these changes. This diminishes the possibility of identifying particles that enter the endcap region. Because the DORIS II endcaps lack the particle identification and calorimetric properties of the central detector, they are used only to verify the absence of particles in the region they cover.

For convenience, the endcap crystals are ordered spatially into minor and major triangles even though their arrangement does not correspond to the central

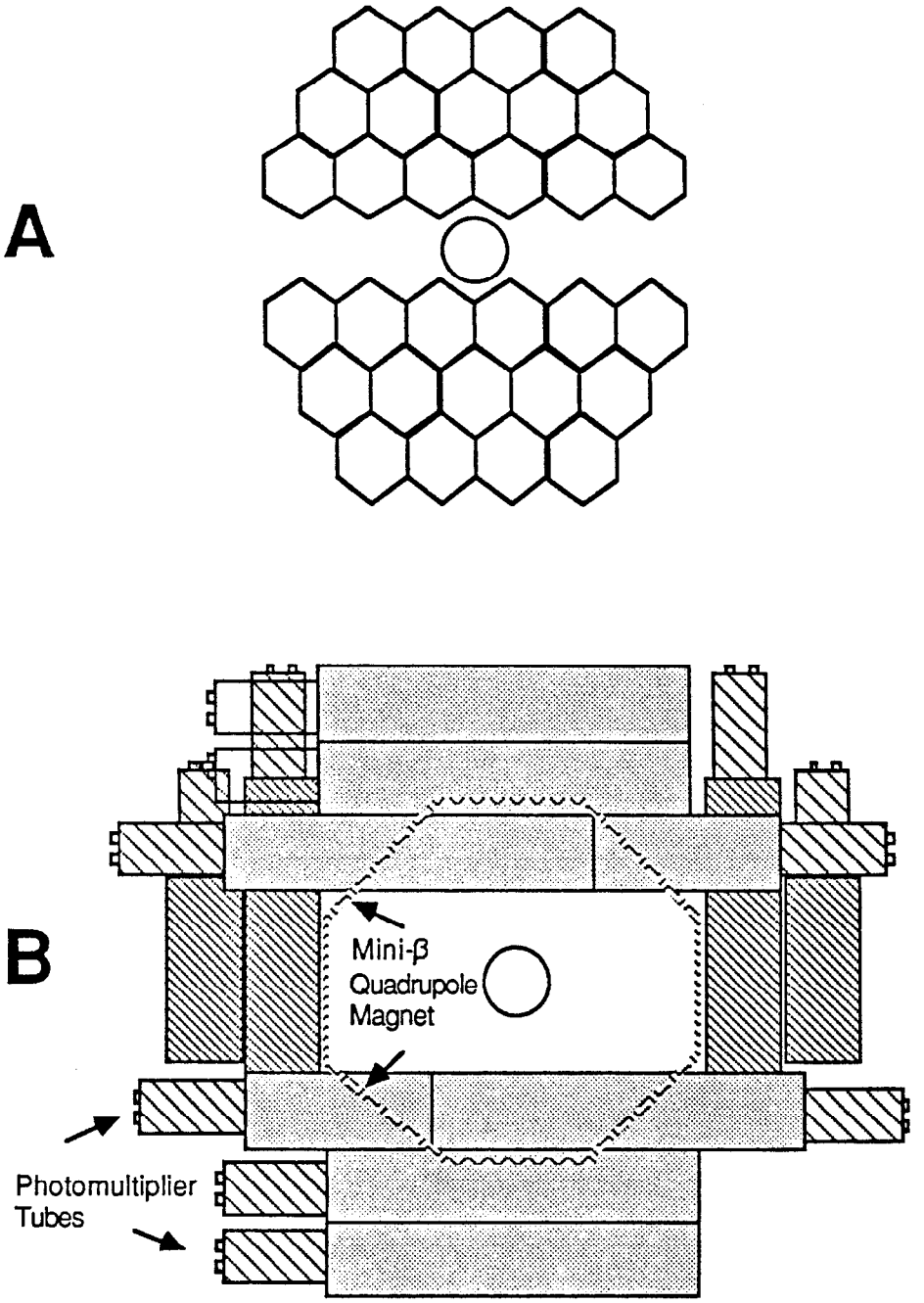

Fig. 2.6 The Crystal Ball Endcap Array. Figure A illustrates the SPEAR projective crystal stacking. Figure B illustrates the corresponding structure as implemented at DORIS II. Views are of the +Z endcap viewed from the center of the detector.

detector geometry. The solid angle covered by the central detector plus endcaps is 98% of 4π.

2.3.4 *Luminosity Measurement*

Colliding beam luminosity is computed by measuring the cross section for Bhabha ($e^+e^- \rightarrow e^+e^-$) scattering in two ways. Electron-positron pairs at small angles to the beam direction are detected by means of a luminosity monitor mounted on the beam pipe between the central detector and the endcaps. The luminosity monitor consists of 4 sets of shower counters of known position and dimension. The Bhabha cross section can be integrated over the solid angle covered by the luminosity monitor to determine a constant which can be used to relate the number of observed Bhabha pairs to the actual integrated luminosity. The luminosity monitor provides immediate feedback which can be used to diagnose problems in the detector or the collision process.

Because the central detector is able to accurately detect Bhabha pairs, an online estimate of the integrated luminosity is available for comparison with the luminosity monitor. Since the detected Bhabha pairs are at larger angles from the beam direction than the sample used by the luminosity monitor, the counting rate is lower, however, and the initial statistical errors are greater. After the data has been calibrated and fully analyzed off-line, the large angle luminosity derived from central detector Bhabha pairs gives a more accurate value than that derived from the luminosity monitor. For that reason, this thesis will quote the measured large angle luminosity.

2.3.5 *Time of Flight System*

A system of plastic scintillators used to provide time-of-flight information to aid in cosmic rejection was installed at DORIS. The TOF system covered 50% of the 2π solid angle above the ground floor. The scintillators were installed outside

of the environmental enclosure (dryhouse) around the central detector. They are not used in this analysis. Detailed information may be found in ref. 6.

References

1) M. Oreglia, Ph.D. Thesis, "A Study of the Reactions $\psi' \rightarrow \gamma\gamma\psi$," Stanford U., 1980. SLAC Report-236. Unpublished.

2) E. Bloom and C. Peck, "Physics with the Crystal Ball Detector," *Ann. Rev. Nucl. Part. Sci.*, **33**, 143 (1983)

3) J. Gaiser, Ph.D. Thesis, "Charmonium Spectroscopy from Radiative Decays of the J/ψ and ψ'," Stanford U.,1982. SLAC Report-255. Unpublished.

4) R. Lee, Ph.D. Thesis, "Radiative Decays of the Psi Prime to All-photon Final States," Stanford U., 1985. SLAC Report-282. Unpublished.

   See also ref. 1.

5) The use of this gas mixture is based on experience gained by the HRS collaboration at SLAC. See
   D. Rubin, *et al. Nucl. Inst. and Methods*, **203**, 119 (1982).

6) D. Prindle, Ph.D. Thesis, "Measurement of the Resonance Parameters of the Υ and Υ' Mesons," Carnegie-Mellon U., 1985. Unpublished.

Chapter 3

Data Acquisition and Initial Analysis

This chapter details the acquisition and initial processing of Crystal Ball Data. During this procedure, raw pulse height information from photomultipliers and tube chambers is converted into particle 4-vectors which can then be further analyzed. The basic techniques used in this thesis work for identifying photons, π^0s and events containing multiple pions are also described.

3.1 Data Acquisition Chain

Crystal Ball data is initially acquired by means of a PDP 11/T55 controlled CAMAC system. Event processing is commenced within 300 nanoseconds of an electron-positron beam crossing if a trigger signal is asserted. Appendix A describes the trigger system. Each phototube is attached through a twisted pair cable to a resistive divider circuit which drives separate large pulse height ("high channel") and low pulse height ("low channel") RC circuits. These circuits integrate and store the signal from the NaI modules. The pulse presented to the high channel is reduced by a factor of 21. The use of two RC circuits for each crystal channel increases the dynamic range available to a 13 bit ADC which sequentially scans each channel by means of FET switches at the peak of the integrated pulse. The Crystal Ball data acquisition system has been extensively described in ref. 1-6.

Tube chamber information is handled in a similar fashion to the crystal

information. A single channel for each of the two preamps attached to every wire integrates the tube chamber pulse heights. A second scanning ADC digitizes these values and is read out whenever a trigger is asserted. Major triangle and hemisphere energy sums are monitored by dedicated ADCs. Constant-fraction discriminators connected to TDCs generate timing signals based on these energy sums. These additional signals are collected by interrogating CAMAC modules.

At the SPEAR storage ring, the raw data had been immediately written to 1600 BPI tape by the PDP 11 minicomputer. For the DORIS running, the computer system was modified to allow transmission of the data via a fast link to the DESY IBM 3081 mainframe. The data was accumulated on disk and then dumped to 6250 BPI tape. Approximately 30 million triggered events were eventually written to tape during the $\Upsilon(2S)$ running.

Because of the presence of computer resources and personnel experienced with Crystal Ball data analysis, raw data tapes were airfreighted from DESY to SLAC for "production." The production process involved the creation and use of calibration constants to obtain actual energies and pulse heights from the crystal and tube chamber ADCs. The crystal and chamber information was then interpreted in order to identify charged and neutral particle track energies and directions.

3.2 Calibration

The raw low and high energy channel signals recorded via the scanning crystal ADC must be converted to real energies. This process assumes a linear relationship between the recorded pulse heights and the deposited energy in each crystal. The reading for each channel may then be converted to an energy by measuring a slope and pedestal for that channel. The operation of DORIS II was interrupted for eight hours once every two weeks in order to measure pedestals and perform the first two steps of the slope determination procedure. This access also served as a means of finding problems and monitoring changes in the

detector electronics.

Pedestals were measured by utilizing a pulser to trigger the data acquisition system when beams were not present in the machine. This method yields the number of ADC counts to be expected even when energy is not deposited in a given NaI module.

Slopes are determined by means of an iterative procedure which makes use of three inputs:

- .66 MeV photons from a Cs^{137} source.
- 6.1 MeV photons from a fluorine target bombarded by 450 KeV protons produced by a Van de Graaf generator via the reaction:

$$\begin{array}{l} {}^{19}\mathrm{F} + \mathrm{p} \rightarrow {}^{20}\mathrm{Ne}^{*} \rightarrow {}^{16}\mathrm{O}^{*} + \alpha \\ \qquad\qquad\qquad\qquad\quad \big\lfloor\!\!\longrightarrow \ {}^{16}\mathrm{O} + \gamma(6.131\ \mathrm{MeV}) \end{array} \qquad [3.1]$$

- 4-5 GeV electrons and positrons from the QED Bhabha reaction: $e^{+}e^{-} \rightarrow e^{+}e^{-}$.

The cesium source and Van de Graaf measurements are typically performed during the bi-weekly access period. They are used to make the initial estimate of the low channel slopes which is used to locate the Bhabha energy peak for each crystal. The location of the Bhabha energy peak then determines the slope assigned to each channel. The QED events employed in this analysis are culled from colliding beam raw data taken during the period for which a calibration is desired. The complete calibration procedure including the determination of slopes is well described in references 4 and 6.

The assumption of complete linearity between the crystal energies and recorded ADC counts in the calibration and production procedure was found to be

somewhat in error during the study of the process:

$$\begin{array}{l} \Upsilon' \rightarrow \pi^0\pi^0\Upsilon \\ \qquad\qquad\quad \Big\lfloor\!\!\longrightarrow\ l^+l^-\ (l = \mu \text{ or } e)\,, \end{array} \qquad [3.2]$$

as reported in ref. 6. Deviations of up to 5% from linearity were seen in the energy of photons used to reconstruct π^0s. A correction which will be referred to as ELOG was applied to photon energies to account for this problem. This correction yields the correct π^0 mass and $\pi^0\pi^0$ system mass distribution. The ad hoc ELOG correction is given by

$$E_{ELOG} = \frac{E_\gamma}{1 + .0137\ ln\frac{E_\gamma}{E_{beam}}}\,. \qquad [3.3]$$

This correction will be applied to the final data samples used in this study.

3.3 Pre-selection and Production

Once the calibration constants for a given data sample (usually two weeks worth of running) have been determined via the calibration procedure, production takes place. The production process involves the maintenance of several large data sets. One of these is the Runlog which records the beam energy, luminosity and running conditions for specific runs. Large calibration files must also be built and maintained. To complicate this enterprise, Υ(2S) production took place simultaneously on the SLAC IBM 3081 mainframe and a VAX 780 made available for this purpose by the Princeton members of the collaboration. Tape and data formatting routines had to be developed to ensure that data processed on one machine could be read by the other.

Due primarily to the use of higher energy beams, a greater mix of triggers, and a lower resonance cross section, a larger percentage of beam-related background events was encountered at DORIS II than at SPEAR. In order to optimize

the use of computer resources and physicist's time, it was decided to implement a data pre-selection process which would determine which events would be put through the complete production procedure. An event was selected for production if an initial analysis showed that it satisfied loose cuts for at least one of 17 possible physics process categories. The initial determination of whether or not to keep an event required an average of 30% of the computer time needed for the full production of that event. The EOTAP pre-selection program passed roughly 70% of the $\Upsilon(2S)$ raw events. These events were subsequently fully analyzed. Information on the physics categories employed and details of the selection process may be found in ref. 7.

The production analysis process can be separated into the connected regions, bumps, tracking, energy sorting, and time-of-flight steps. A summary of these steps is presented below. Full information may be found in ref. 8.

3.3.1 *Connected Regions*

"Connected regions" are identified after the crystal energies are determined by applying the calibration constants to the raw crystal pulse heights. A connected region is defined to be a set of contiguous crystals each with at least 10 MeV of deposited energy. Two crystals are contiguous if they share a face or vertex.

3.3.2 *Bumps*

A connected region is presumed to contain the energy deposited by one or more incident particles. It is the job of the bumps step to determine the number and approximate position of these particles. The bumps algorithm attempts to do this by finding local energy maxima within a connected region. The algorithm commences by labelling the highest energy crystal in a connected region as a bump module. The three nearest neighbor crystals (See figure 3.1) are immediately associated with this bump module. The remaining crystals within the

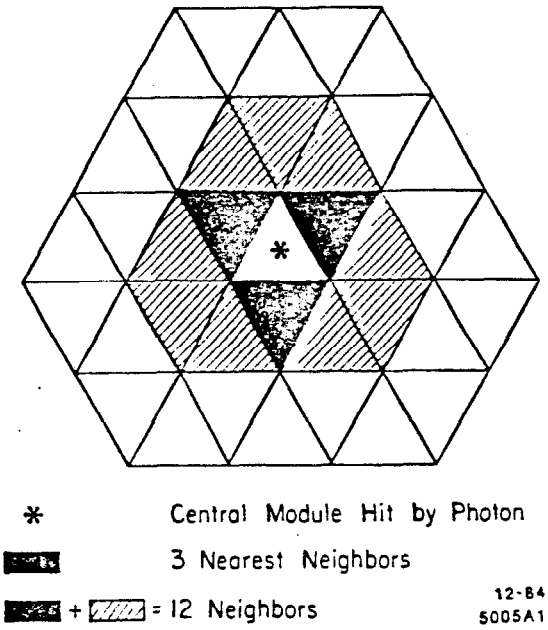

Fig. 3.1 Relationship between a NaI module and its surrounding modules.

connected region are also associated with the first bump module if they satisfy the condition:[9]

$$E_i < E_{bump} \times 0.72e^{-9.4(1-\cos\theta_i)} \quad \text{for } 15° < \theta_i < 45° \qquad [3.4]$$

or

$$\theta_i < 15° \quad , \qquad [3.5]$$

where E_i is the energy of the i^{th} module and θ_i is the angle between that module and the bump module. This formula was developed empirically during analysis of SPEAR data and found to work well with the higher energy DORIS data. If crystals remain unassociated with a bump module after this test is applied, a new pass is begun. The highest energy crystal remaining is labelled as a bump module, its nearest neighbors are associated with it, the bumps test is applied and the cycle continues until all crystals within a connected region are accounted for. The preselection cuts described above are applied at this point in the analysis.

3.3.3 *Tracking*

Tube chamber information is now correlated with the bumps found in the previous production step. Charged particles are identified and particle track 4-vectors are constructed. Raw pulse heights are available from the two preamps on the ends of each chamber wire. This information allows the determination of the ϕ and z-axis (beamline) coordinates of each "hit" in the chambers. Particle tracks are fitted using these coordinates. If a bump module is congruent with one of these tracks, the track associated with that bump will use the fitted track directions. These tracks are referred to as "IR" tracks. A track may also be 'tagged' as coming from a charged particle if one or more chamber hits falls within a certain $\Delta\ \phi$ or Δz window of a bump module direction. The direction of tagged and neutral tracks are derived from the radius vector to the centroid of the bump module. Figure 3.2 presents a Mercator display of a typical Crystal Ball event. This type of display is a two dimensional mapping of the crystal energies. Track bank information appears on the left side of the figure.

3.3.4 *ESORT*

Energies derived from the bumps step are assigned to particle tracks in this step. To first order, the energy assigned to a track is based on the energy contained in the bump module and its 12 nearest neighbors. This energy is referred to as the 'sum of thirteen', $E_{\Sigma_{13}}$, and is subject to two corrections. The first correction occurs because the 13 crystals do not fully contain the lateral extent of the energy deposited by electromagnetically showering particles. The mean energy fraction missed by $E_{\Sigma_{13}}$has been determined to be 2.25% (with large fluctuations) by studying $e^+e^- \rightarrow e^+e^-$ events. The second adjustment to $E_{\Sigma_{13}}$is the PCORR correction:

Because the Crystal ball is not a homogeneous structure, the energy deposited by a particle depends in part on its point of entry within the ball. Particles that

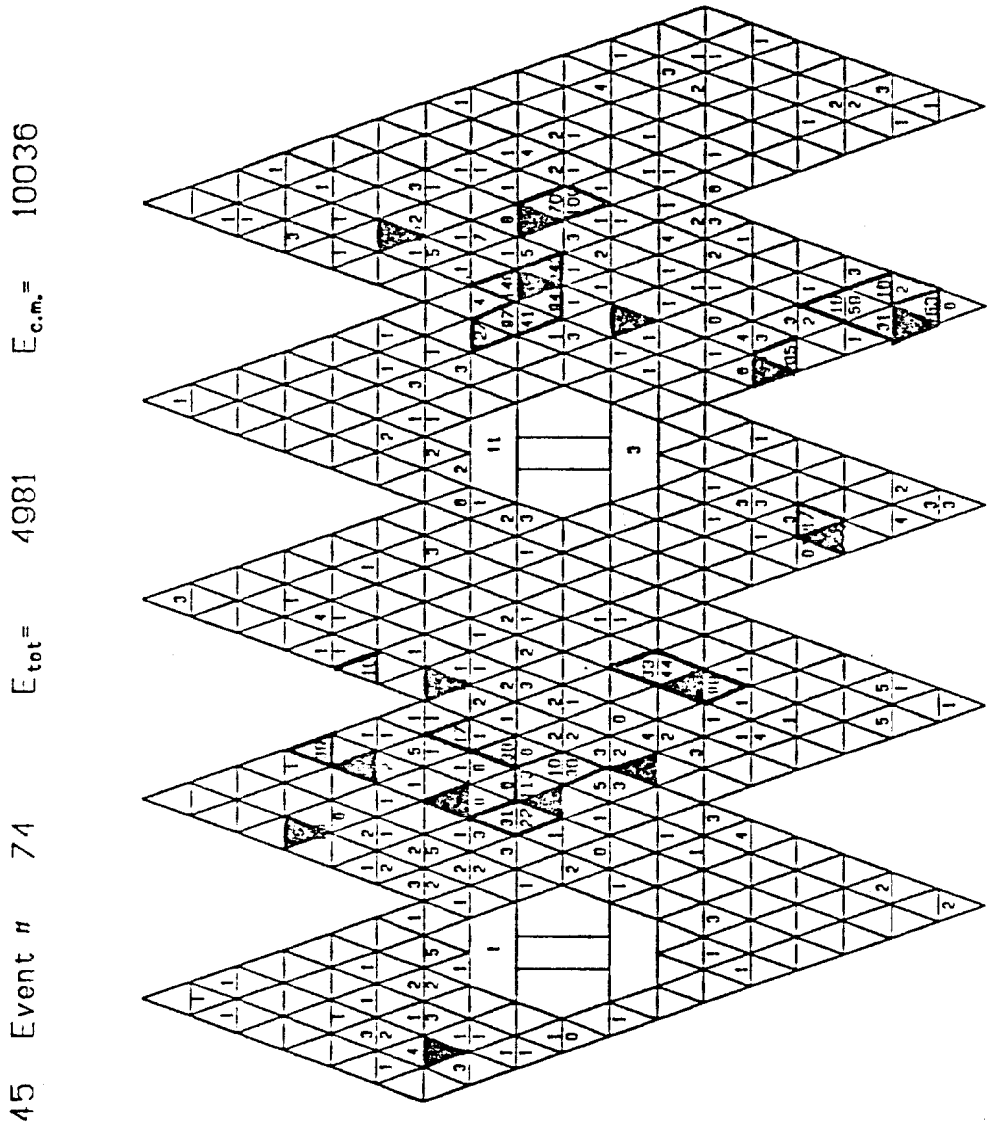

Fig. 3.2 A 'flats' display of a multihadron event. Bump modules connected with the 15 tracks are shaded. Connected region boundaries are also indicated. The +Z and -Z endcap energies are 1 and 14 MeV respectively.

enter a crystal near one of its vertices or faces will deposit a larger fraction of energy in crystal wrapping or structural material than a particle that is incident near the center. The light collection efficiency is also degraded for particles away from the crystal center. An approximate correction for this effect as a function of the ratio $\frac{E_{bump}}{E_{\Sigma_{13}}}$ was determined from Bhabha events.[4] The final value for the energy assigned to the track is given by

$$E_{13} = E_{\Sigma_{13}} \times 1.0225 \times \mathrm{PCORR}\left(\frac{E_{bump}}{E_{\Sigma_{13}}}\right) \quad , \qquad [3.6]$$

where $PCORR\left(\frac{E_{bump}}{E_{\Sigma_{13}}}\right)$ is the position correction.

A second effort is made in this step to better determine the direction of neutral particles. For this purpose, each bump module is considered to be composed of 16 triangular submodules. Monte Carlo generated shower functions are used to determine an energy allocation scheme amongst the submodules which can best account for the energy deposited in the bump module and its three nearest neighbors. The centroid of the highest energy submodule is used to define the direction of the neutral particle track. This use of this method implies that all neutral particle tracks have quantized directions. The angular resolution for neutral tracks is approximately 30 milliradians.

3.3.5 *TOF*

The TOF step compares track bank directions to signals in the time-of-flight counters. Timing information is available for particle tracks that are associated with hits in the TOF counters. This information is useful in separating events which have their origin in cosmic ray interactions from annihilation events. The TOF counter information is not directly used in this study. Further details may be found in ref. 5.

3.4 Photon Identification

The track bank generated during the production process may now be scanned to determine which tracks correspond to photons. Photons are identified by demanding that the track be neutral and that the distribution of energies in the sum of 13 modules be characteristic of an electromagnetically showering particle as determined by a 'pattern cut.' Various photon pattern cuts have been developed for use in the Crystal Ball by means of Monte Carlo simulation of the detector. (The Crystal Ball Monte Carlo simulation is described in appendix B.) The pattern cuts are used to reject tracks corresponding to untagged minimum ionizing particles. They are also useful in excluding particles that do not traverse the detector radially but which may arise from interacting hadrons, cosmic rays or beam gas. These pattern cuts usually specify an acceptance window on the ratios $\frac{E_1}{E_4}$ and $\frac{E_4}{E_{13}}$ where

- $E_1 = E_{bump}$,
- $E_4 = E_{bump}$+ sum of three nearest neighbors,
  and
- $E_{13} = E_{bump}$+ sum of twelve nearest neighbors. (Corrected as described above.)

  In this analysis, the following pattern cut has been used:

$$\frac{E_1}{E_4} \geq 0.4 \quad \text{and} \quad \frac{E_4}{E_{13}} \geq .56 \quad . \qquad [3.7]$$

This pattern cut was designed to be very nearly 100% efficient for accepting low energy photons from the reaction: $\Upsilon' \rightarrow \pi^0\pi^0\Upsilon(\Upsilon \rightarrow \text{Unseen})$, where the pions then decay via the process $\pi^0 \rightarrow \gamma\gamma$. Figure 3.3 shows the $\frac{E_1}{E_4}$ and $\frac{E_4}{E_{13}}$ distributions for low energy photons as determined via Monte Carlo simulation of the detector.

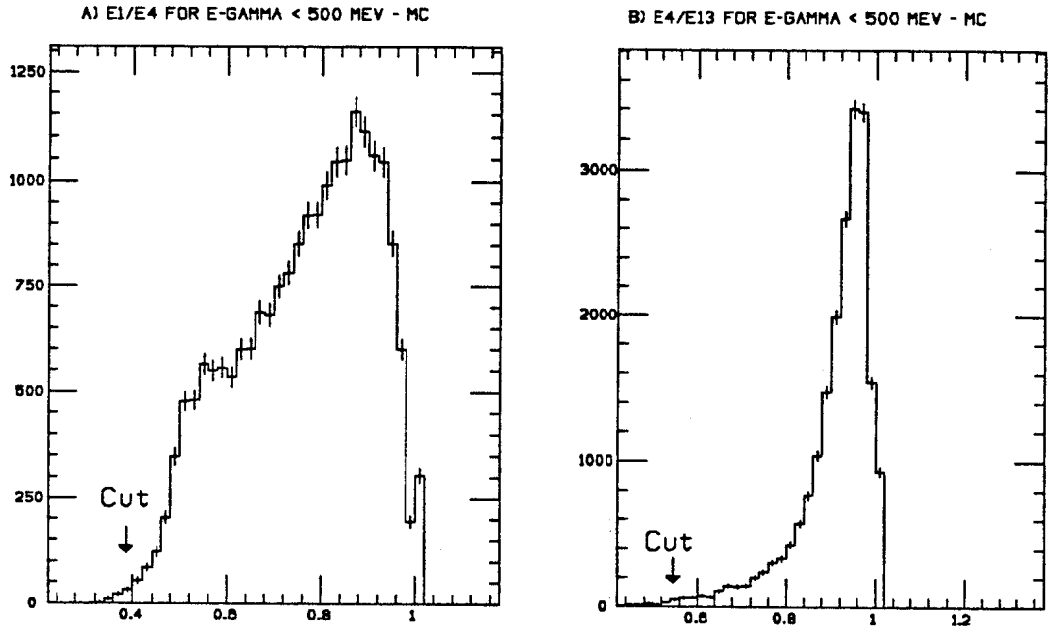

Fig. 3.3 Photon pattern cut energy ratios. Figure A shows the distribution of the ratio of $\frac{E_1}{E_4}$ for photons generated in the Monte Carlo detector simulation. Figure B shows the $\frac{E_4}{E_{13}}$ distribution for these photons.

3.5 π^0 and $\pi^0\pi^0$ Identification

π^0s were reconstructed by pairing identified photons through the relation:

$$m_{\gamma\gamma}^2 = 4E_1E_2sin^2\left(\frac{\theta_{\gamma\gamma}}{2}\right) \quad , \qquad [3.8]$$

where E_1 and E_2 are the energies of the two photons under consideration and $\theta_{\gamma\gamma}$ is the angle between them.

The PHYSAC program[10] was employed to find the best π^0 candidates by pairing all photons found in an event. The routine worked as follows:

1) User supplies a set of photon 4-vectors.

2) PHYSAC calculates the invariant mass of every possible pair using the above relation.

3) Every pair is associated with a possible mass hypothesis provided by the user. (e.g. $m_{\gamma\gamma} = m_{\pi^0}$, m_η, etc.)

4) Every pair is fitted to the appropriate mass hypothesis. During the fit, the photon energies and directions may be varied. A χ^2 value for the fit is determined.

5) All pairs with $\chi^2 > \chi^2_{max}$ are rejected. χ^2_{max} is furnished by user.

6) All surviving pairs are scanned to find 'configurations' with the maximum number of pairs in which no photon is used more than once.

7) Configurations are rejected if a confidence level based on the total χ^2 of the photon pairs is less than a user supplied minimum value, CL_{min}.

8) In this analysis, the configuration with the minimum total χ^2 is retained.

Events in which PHYSAC found a configuration with more than 2 π^0s were also accepted in the initial analysis stages. In particular, it was desired to see evidence of the two photon process:

$$e^+e^- \rightarrow e^+e^-\gamma\gamma \rightarrow e^+e^-\eta \qquad \eta \rightarrow \pi^0\pi^0\pi^0 \quad , \qquad [3.9]$$

(where the final state e^+e^- disappears down the beampipe) as a means of monitoring the analysis and detection efficiency for the $\pi^0\pi^0$ hadronic transition. The invariant mass, energy and momentum of the system formed from all π^0s found in the favored configuration was computed using both the original unfitted photon and PHYSAC fit 4-vectors. This furnished both an unfitted and fit pion system mass and energy. In the case of a two pion configuration, the dipion system can be assumed to arise via the decay:

$$\Upsilon' \rightarrow A_{\pi^0\pi^0} + X \qquad A_{\pi^0\pi^0} \rightarrow \pi^0\pi^0, \qquad [3.10]$$

where A acts as a pseudoparticle with varying mass, $m_{\pi\pi}$. In this case, the properties of X may also be determined to be:

$$E_X = M_{\Upsilon'} - E_{\pi\pi} \quad , \qquad [3.11]$$

$$\vec{P_X} = -\vec{P_{\pi\pi}} \quad , \qquad [3.12]$$

and

$$M_X = \sqrt{E_X^2 - \vec{P_X}^2} \quad . \qquad [3.13]$$

A plot of M_X for $\Upsilon(2S)$ decay events in which only two pions are detected is expected to yield a peak in the 'missing mass' distribution at the value $M_X = M_\Upsilon$. The measurement of this peak will be discussed in the next chapter.

References

1) Operational details of the Crystal Ball data acquisition system are given in:

R. Chestnut, *et al.* , *IEEE Trans. Nucl. Science*,NS-26, 4395 (1979).

G. Oxoby, "A Fast LAM Handler for the PDP-11," Crystal Ball Note 114, SLAC 1976.

G. Godfrey, "Integrate and Hold Module," Crystal Ball Note 121, SLAC 1976.

G. Godfrey, "Back-to-Back 36'er," Crystal Ball Note 122, SLAC 1976.

C. Kiesling, "Some Considerations about the Crystal Ball Online System (CBOLS)," Crystal Ball Note 124, SLAC 1976.

2) M. Oreglia, Ph.D. Thesis, "A Study of the Reactions $\psi' \rightarrow \gamma\gamma\psi$," Stanford U., 1980. SLAC Report-236. Unpublished.

3) J. Gaiser, Ph.D. Thesis, "Charmonium Spectroscopy from Radiative Decays of the J/ψ and ψ'," Stanford U.,1982. SLAC Report-255. Unpublished.

4) R. Lee, Ph.D. Thesis, "Radiative Decays of the Psi Prime to All-photon Final States," Stanford U., 1985. SLAC Report-282. Unpublished.

5) D. Prindle, Ph.D. Thesis, "Measurement of the Resonance Parameters of the Υ and Υ' Mesons," Carnegie-Mellon U., 1985. Unpublished.

6) D. Gelphman Ph.D. Thesis, Measurement of the Decay $\Upsilon(2S) \rightarrow \pi^0\pi^0\Upsilon$, Stanford U. 1985, SLAC Report 286. Unpublished.

7) J. Gaiser, D. Gelphman, J. Irion, B. Lockman, and J. Tompkins, Crystal Ball note 167. SLAC 1983.

8) See ref. 2. Also

Crystal Ball Offline Workshop. SLAC 1983.

9) R. Partridge, Crystal Ball note 6, SLAC Feb. 1979.

10) The PHYSAC routine was written by John Tompkins of the Crystal Ball Collaboration. Information on the routine is contained in two internal Crystal Ball memorandums.

"Notes on the Use of the "Global" Pair Reconstruction Routines," J. Tompkins, 15 March 1979.

"Modifications to PHYSAC Routines," J. Tompkins, 11 May 1984.

Chapter 4

Search for $\Upsilon' \rightarrow \pi^0\pi^0\Upsilon$, $\Upsilon \rightarrow$ Unseen

The $\Upsilon(2S)$ data set used in this thesis was taken from November 1982 to February 1984. Approximately 193,000 $\Upsilon(2S)$ events were produced in 61.7 pb^{-1} of integrated luminosity. The highest luminosity running occurred at the end of this period and as a result 40% of these events were taken in January and February of 1984.[1] Because the NMULT trigger had to be specially designed and implemented in order to detect the process studied in this chapter, much of this data was taken before its installation. The integrated luminosity available for this study is 44.1 pb^{-1}. This corresponds to 141,000 produced $\Upsilon(2S)$ resonance decays.

This chapter describes the steps taken in the analysis of this data in the search for $\Upsilon' \rightarrow \pi^0\pi^0\Upsilon$ where the Upsilon decay is unseen by the detector. Data selection and analysis stages are treated in the first section. The next sections estimate the efficiency of this analysis for finding examples of this reaction in the data, give the results of this analysis and consider possible backgrounds to the desired reaction. The last section then presents the final conclusion from this study.

4.1 Data Selection and Analysis

The previous chapter has described the data acquisition and production processes as well as the methodology employed to identify photons and reconstruct π^0s. At the end of the production process, $\Upsilon(2S)$ data tapes containing 30 million events were available for further analysis. The analysis of this data will be described in this section. Because it was impractical to fully analyze the entire data set at one time, the data analysis task was divided into a series of passes through a subsequently diminishing amount of data. Loose cuts to select events containing more than one π^0 were made in pass 1. Events with charged tracks were then eliminated in a separate pass and the final analysis was performed in pass 2. The data analysis and selection cuts in each pass are outlined in the following sections.

4.1.1 *Pass 1 Cuts*

The initial selection procedure was based on the following cuts:

1) Events were triggered by the NMULT or NTOPO triggers. [4.1]

2) Events pass data preselection cuts (EOTAP) during production. [4.2]

3) Events must contain ≥ 3 connected regions of energy deposition. [4.3]
The energy within each connected region must be ≥ 20 MeV.

4) Four or more photon candidates must be found from [4.4]
neutral tracks which pass the photon pattern cut.

5) PHYSAC finds a photon pair configuration with $\geq 2\pi^0$s. [4.5]

Cut (3) was designed to reject low multiplicity cosmic ray events at an early stage of the analysis. During this analysis step, 269 produced data input tapes were read. The resulting output was written in a compressed format to 5 summary tapes containing information on approximately 300k events of which there were about 135k NMULT trigger events and 197k NTOPO triggers.

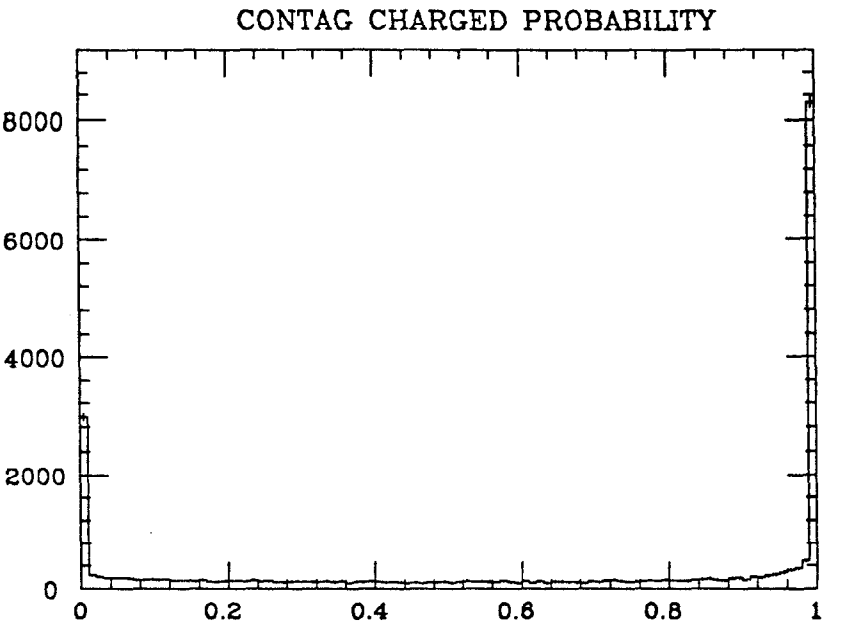

Fig. 4.1 Charged event probability distribution for a subset of Pass 1 data sample. Unambiguously neutral or charged events are assigned to the $P_{charged} = 0$ or 1 bins, respectively.

4.1.2 *CONTAG*

A routine to assess the probability that a (NaI) track is charged was developed during the analysis of DORIS II data[2] . This routine assigns a charged probability to a track by considering the distance from the track to all hits in the chamber system.* Because this probability is not quantized in the way that the production software charged/neutral decision is, it is possible to plot charged probability distributions and to use these continuous distributions to define cuts. The probability that an event contains a charged track can also be defined by

---

* Gaussian sigmas for a chamber hit in Z (beam axis) and ϕ and for the NaI track direction ($\pm 2°$) are used to calculate a χ^2 for each chamber hit with respect to the NaI track of interest. The confidence level of this χ^2 is said to be the "probability this hit makes the NaI track charged." The probabilities from all chamber hits are combined to form the probability that the track is charged.

means of:

$$P_{charged} = 1. - \Pi_i(1. - P_{ct}^i) \qquad [4.6]$$

where P_{ct}^i is the probability that the i^{th} track is charged. At this point in the analysis, the Pass 1 tapes were scanned using the CONTAG routine to select events containing all neutral particles. Events were accepted if:

6) $P_{charged} < 0.2$ [4.7]

Figure 4.1 shows a plot of the charged event probability for a subset of data before this cut.

4.1.3 *Pass 2 Cuts*

The events which survived both the Pass 1 and CONTAG cuts were further analyzed with the following cuts after making the ELOG correction (eqn. 3.2) on the photon energies.

7) # photons = 4,
where photons are required to satisfy the conditions *:
$E_{13} > 20$ MeV and $|\cos\theta_{track}| < .85$. [4.8]

8) # π^0s found by PHYSAC = 2. [4.9]

Cut (7) demands that all photons used in the analysis be well within the solid angle of the central detector. This cut excludes photons too near the tunnel modules surrounding the beampipe as well as those having very low energy. Cut (8) then requires that the four remaining photons have been used by PHYSAC to reconstruct exactly two π^0 candidates.

---

* The solid angle acceptance of $|\cos\theta| < .85$ was chosen such that only photons detected within the central detector and safely away from the solid angle covered by the trigger vetoed tunnel region modules ($.85 < |\cos\theta| < .93$) would be considered by the π^0 kinematic fit program. The solid angle covered by the tunnel region is not available to interacting particles assuming efficient operation of the trigger veto (see appendix A for further details).

4.2 Analysis Efficiency Determination

Because of fundamental limitations, the process studied in this chapter can not be detected with 100% efficiency. These limitations are due partly to the fact that the detector does not cover 4π solid angle. Another factor is that trigger energy thresholds must be set high enough to limit the data acquisition rate to reasonable levels. This requirement results in tighter constraints on accepted events. These constraints exclude some fraction of the desired events. In practice, a trade-off must be made between raising the sampling efficiency of the trigger and increasing the raw trigger rate.

The data analysis steps presented in the previous section also suffer from inefficiencies. The efficiency of the analysis stages is determined with the aid of pseudo-events generated by means of a detector Monte Carlo simulation. These events also allow the evaluation of trigger efficiencies. Appendix B describes the Crystal Ball detector simulation program. The charged particle cut efficiency is estimated by means of two photon interaction events culled from data.

4.2.1 *Monte Carlo Event Samples*

Monte Carlo 4-vectors for the decay $\Upsilon' \to \pi^0\pi^0\Upsilon$ were generated by means of a model which treats the $\pi^0\pi^0$ transition as a two body decay of the Υ' into a pseudoparticle and an Υ by means of gluon emission. The gluons which form the pseudoparticle then fragment to form light hadrons according to the reaction:

$$\begin{array}{l} \Upsilon' \to A_{\pi^0\pi^0} + \Upsilon \\ \qquad\quad \Big\lfloor\!\!\longrightarrow \pi^0\pi^0, \end{array} \qquad [4.10]$$

In this model, A acts as a pseudoparticle with mass, $m_{\pi\pi}$. The exact processes involved in this reaction are as yet not completely understood but the PCAC formalism and current algebra have been used to place constraints on the interaction

matrix element. The $m_{\pi\pi}$ distribution is given by[3]

$$\frac{d\,N}{d\,m_{\pi\pi}} \propto K \cdot (m_{\pi\pi}^2 - \lambda m_{\pi^0}^2)^2 \qquad [4.11]$$

where the phase space factor is

$$K = \left[\left((M_{\Upsilon'} + M_{\Upsilon})^2 - m_{\pi\pi}^2\right)\left((M_{\Upsilon'} - M_{\Upsilon})^2 - m_{\pi\pi}^2\right)\left(m_{\pi\pi}^2 - 4m_{\pi^0}^2\right)\right]^{\frac{1}{2}}. \qquad [4.12]$$

$\lambda = 2$ is expected if the dipion system is produced completely isotropically. The value used in the model was based on a CLEO result[4] of $\lambda = 3.2 \pm 0.4$.

The Monte Carlo event generator allowed the Upsilon particles to decay into charged lepton or neutrino pairs. The neutrino pairs effectively simulated the $\Upsilon \rightarrow$Unseen condition. Because the Upsilon has little kinetic energy, the e^+e^-, $\mu^+\mu^-$, and $\tau^+\tau^-$ pairs are produced almost back-to-back. It is therefore expected that some lepton pairs produced via this reaction will disappear into the solid angle not covered by the central detector and thus mimic the $\Upsilon \rightarrow$Unseen signal. Because the dipion system is produced in a spin 0 state, the original polarization of the $\Upsilon(2S)$ is retained by the $\Upsilon(1S)$. The angular distribution of the lepton pairs will then be of the form:

$$1 + \cos^2\theta + \eta_{pol}^2 \sin^2\theta \cos 2\phi \qquad [4.13]$$

where η_{pol}^2 refers to the fraction of transverse polarization present. The transverse beam polarization at DORIS II has been measured to be in the range 70-80%.[7] The Monte Carlo data sets used in this analysis were generated with 70% polarization.

The generated 4-vectors are then passed to the detector simulation part of the Monte Carlo. This program determines the energy that would be deposited by incident particles in the Crystal Ball based on the particle type, energy, location, and direction. Photons, electrons and muons are treated by means of a modified

version of the EGS program.[5] Monte Carlo events generated in this way are produced in the same manner as data but with an energy correction step[6] which replaces the calibration/ energy correction discussed earlier in this chapter.

4.2.2 *Trigger Efficiency*

Trigger efficiencies for the NMULT and NTOPO triggers were obtained by means of the trigger simulator program described in appendix B. Monte Carlo events were evaluated by this program which would then determine whether or not a given trigger would have been asserted or not based on measured discriminator efficiency curves.

Monte Carlo events from the four processes:

$\Upsilon' \rightarrow \pi^0\pi^0\Upsilon$	NMULT Trigger Efficiency	
$\longrightarrow$ *Unseen*	(22.2%)	[4.14]
$\longrightarrow$ e^+e^-	(1.9%)	[4.16]
$\longrightarrow$ $\mu^+\mu^-$	(6.0%)	[4.15]
$\longrightarrow$ $\tau^+\tau^-$	(1.0%)	[4.17]

generated as described above were passed through the NMULT trigger software simulation. The resulting efficiencies are indicated in parentheses. The number of Monte Carlo events which satisfied the NMULT and NTOPO triggers for each process is indicated in table 4.1.

4.2.3 *Pass 1 Analysis Efficiency*

The efficiency of the Pass 1 cuts is estimated by making the same cuts on Monte Carlo events which pass the NMULT trigger simulation. 14.8% of the initial $\Upsilon \rightarrow$Unseen Monte Carlo events remain after the trigger simulation and Pass 1 cuts. Table 4.1 summarizes this information for all four Monte Carlo data

Selection	$\Upsilon \rightarrow$Unseen	$\Upsilon \rightarrow e^+e^-$	$\Upsilon \rightarrow \mu^+\mu^-$	$\Upsilon \rightarrow \tau^+\tau^-$
Initial	5000	5000	5000	5000
NMULT	1110	96	302	50
NTOPO	0	1864	2242	1873
Either Trigger	1110	1960	2489	1916
Pass 1	741	482	1060	920
Pass 2	667	52	58	7

Table 4.1 Monte Carlo event selection for four Upsilon decay processes via the hadronic transition: $\Upsilon' \rightarrow \pi^0\pi^0\Upsilon$.

sets. The electron and muon events have different efficiencies until the number of tracks in the main detector is limited to 4. This is attributable to the fact that the electrons which enter the central detector will deposit most of their energy in the detector which will normally exceed the NMULT trigger energy window and this energy will be distributed in a broad transverse shower. The second effect will tend to reduce the solid angle available in which π^0 decay photons can be identified. The e^+e^- and $\mu^+\mu^-$ events remaining after Pass 2 are due, for the most part, to gaps in the solid angle acceptance of the detector. The τ s will tend to decay in flight and their decay products have some probability of depositing energy in the detector and thereby generating additional tracks.

4.2.4 *CONTAG Charged Particle Efficiency*

The efficiency for the CONTAG charged particle cut was determined by selecting NMULT or NTOPO trigger events which fit the criteria for the two photon processes:

$$e^+e^- \rightarrow \gamma\gamma e^+e^- \rightarrow e^+e^- \qquad \begin{array}{l} f(1270) \\ \quad \big\lfloor \!\!\rightarrow \pi^0\pi^0 \end{array} \qquad [4.18]$$

or

$$e^+e^- \rightarrow \gamma\gamma e^+e^- \rightarrow e^+e^- \qquad \begin{array}{l} \eta(550) \\ \big\lfloor\!\!\longrightarrow \pi^0\pi^0\pi^0 \end{array} , \qquad [4.19]$$

where the e^+e^- pair disappear down the beampipe.

Four or six track events were selected since the π^0s decay predominantly via photon pairs. Because these reactions produce neutral events, the charged particle cut inefficiency is due either to photon conversions in the beampipe ($\gamma \rightarrow e^+e^-$) or accidental hits in the chambers. 1034 f(1270) events were found before the CONTAG cut and 949 after. The estimated efficiency based on the f channel is then

$$\epsilon_{Charge}^{4Track} = 91.8 \pm 4.7\ \%. \qquad [4.20]$$

59 $\eta(550)$ events were found before the CONTAG cut and 49 after it, yielding an efficiency of

$$\epsilon_{Charge}^{6Track} = 84.2 \pm 13.0\ \%. \qquad [4.21]$$

The efficiency for neutral five track events to pass this cut is assumed to be intermediate between the four and six track results or

$$\epsilon_{Charge}^{5Track} = 88.0 \pm 8.8\ \%. \qquad [4.22]$$

4.2.5 *Pass 2 Analysis Efficiency*

The Monte Carlo events which survived the Pass 1 step were used to estimate the efficiency of the Pass 2 cuts. Table 4.1 indicates the resulting efficiency. Because simulated NMULT triggers were initially required in the Monte Carlo data sample, this result gives the final efficiency estimate.

Selection	$\Upsilon \rightarrow$Unseen	$\Upsilon \rightarrow e^+e^-$	$\Upsilon \rightarrow \mu^+\mu^-$	$\Upsilon \rightarrow \tau^+\tau^-$
MC Efficiency	12.2%	1.0%	1.1%	.1%

Table 4.2 Detection and analysis efficiencies for four Upsilon decay processes via the hadronic transition: $\Upsilon' \rightarrow \pi^0\pi^0\Upsilon$.

4.2.6 *Final Detection and Analysis Efficiency*

The detection and analysis efficiency for the process $\Upsilon' \rightarrow \pi^0\pi^0\Upsilon$ where $\Upsilon \rightarrow$Unseen, may now be estimated. From table 4.1, it is seen that 667 Monte Carlo events are triggered by the NMULT trigger and survive all the analysis cuts. The detection and analysis efficiency for this process based on the Monte Carlo is therefore:

$$\epsilon_{MC} = \frac{667}{5000} = 13.3 \pm .5\%. \qquad [4.23]$$

The CONTAG charged particle cut will eliminate some of these 4 track neutral events so the final efficiency for the detection and analysis of the process

$$\Upsilon' \rightarrow \pi^0\pi^0 Unseen$$

is given by

$$\epsilon_{Analysis} = \epsilon_{Charge} \times \epsilon_{MC} = (.918 \pm .047)(.133 \pm .005) = 12.2 \pm 1.1\% \qquad [4.24]$$

This result and the corresponding results for the other Monte Carlo data sets are indicated in table 4.2.

4.3 Results

Analysis results for the $\Upsilon(2S)$ data are presented in this section. During this analysis, a large number of events satisfying the $\pi^0\pi^0$ selection was observed to populate the entire kinematic region allowed by the NMULT trigger. The source of these events is unknown. It is possible that they may arise from two photon reactions in which one or more particles are unseen because of holes in the detector acceptance. A more likely possibility is that a photoproduction process occurs in the gas within the beampipe. One example of this might be the reaction:

$$\begin{array}{l} \gamma + p \rightarrow \pi^0 + \Delta^+(1232) \\ \qquad\qquad\quad \Big\lfloor\!\!\longrightarrow \pi^0 + p \end{array} \qquad [4.25]$$

Because of the nature of this analysis, only a limited number of options such as cuts on transverse momentum or more severe charged particle cuts were available for rejecting these events. These methods were found to either introduce a recoil mass dependence in the shape of the background or unacceptably reduce the acceptance for the process searched for in this chapter. No cut was found which drastically improved the signal-to-noise ratio for events with missing mass near M_Υ without changing the background shape or smoothness. The final result for BR($\Upsilon\rightarrow$Unseen) will therefore be derived from the missing mass plot based on the analysis steps detailed above.

Because this analysis is dependent on the identification of π^0 pairs, distributions obtained from candidate π^0s and $\pi^0\pi^0$ pairs in the $\Upsilon(2S)$ data are presented and compared to Monte Carlo results. These candidate $\pi^0\pi^0$ pairs then lead to the missing mass plot used to estimate the desired branching ratio.

4.3.1 *Pion Mass Distributions*

In order to verify the operation of the kinematic fitting program, PHYSAC, all unique combinations of four neutral tracks within an event (assumed to be

photons for this purpose) were used to plot

$$m_{\gamma_1\gamma_2} \; vs \; m_{\gamma_3\gamma_4} \quad , \qquad [4.26]$$

making use of uncorrected track energies and directions. Figure 4.2 presents this scatter plot for a subset of the selected events in the final sample. A π^0 peak is clearly seen in each of the projections. A fit to these projections using the uncorrected track energies and directions gives $m_{\pi^0} = 130.4 \; MeV$.

4.3.2 $\pi^0\pi^0$ *Kinematic Distributions*

The PHYSAC routine fits selected photon pairs to a π^0 hypothesis. The pions so constructed are then combined to form a $\pi^0\pi^0$ system. The mass distribution of this system for data and Monte Carlo events is shown in figure 4.3.

4.3.3 *Angular Distributions*

The cos θ distribution for the pions used by the PHYSAC program is plotted in figure 4.4 for both Υ(2S) and Monte Carlo data. The Υ(2S) data are slightly peaked toward $\cos\theta = -1$. This effect suggests that an asymmetric background process is producing some of the photons used by PHYSAC to reconstruct π^0s. The angle between the π^0 momentum vectors may also be plotted. Since the $\pi^0\pi^0$ system mass distribution peaks at high mass values for the $\Upsilon' \rightarrow \pi^0\pi^0\Upsilon$ hadronic transition, the pions tend to be back-to-back. This is seen clearly in the Monte Carlo data and is suggested in the Υ(2S) data. Figure 4.5 shows these two angular distributions. A tendency to peak at $\cos\theta_{\pi\pi} = -1$ is seen in both plots.

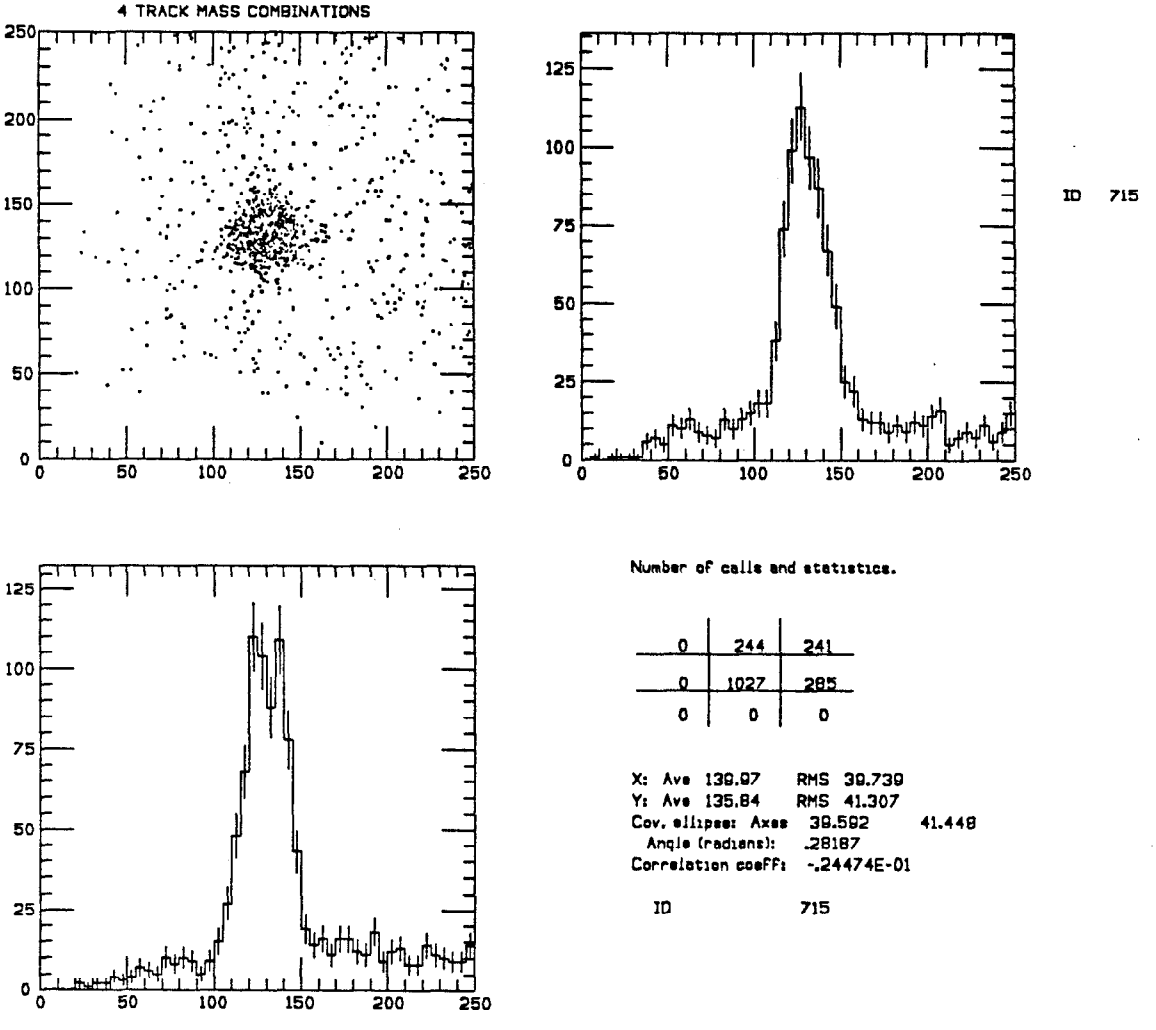

Fig. 4.2 $m_{\gamma\gamma}$ *vs* $m_{\gamma\gamma}$ scatterplot for events with ≥ 4 tracks (Final sample after PHYSAC kinematic fitting). $m_{\gamma\gamma}$ projections are shown. A matrix indicates the number of events within the scatterplot as well as the number of events with $m_{\gamma\gamma} > 250$ MeV on the vertical or horizontal axis. Unfitted photon energies and directions are used to form the paired photon masses.

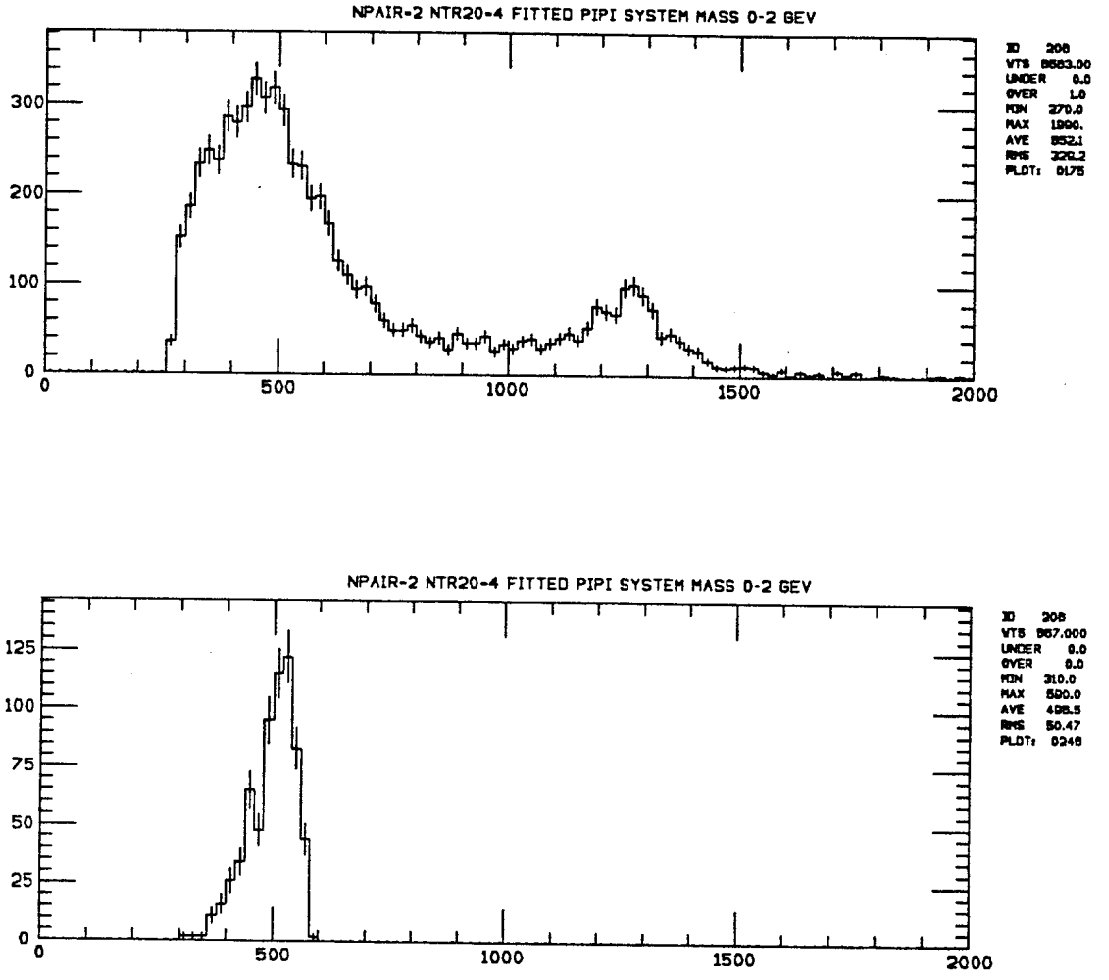

Fig. 4.3 $\pi^0\pi^0$ system mass distributions for the final event sample. The top figure indicates the mass distribution for the final event sample and the bottom shows the corresponding distribution used in the Monte Carlo. Events with $M_{\pi\pi} > 700 - 800$ MeV are triggered only by the NTOPO trigger and do not contribute to the missing mass distribution in the Upsilon mass region. An enhancement near the f(1270) mass is seen for these events. Conversely, events below this range satisfy the NMULT trigger total energy window and contribute to the missing mass distribution in the Υ mass region. The number of Monte Carlo events in the lower plot is not normalized to the data.

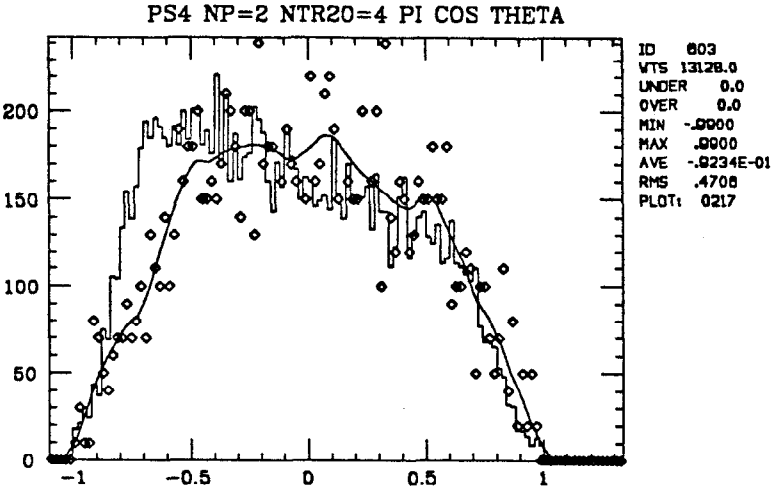

Fig. 4.4 $\cos\theta$ for pions found by PHYSAC. The distribution obtained from the final $\Upsilon(2S)$ data sample is histogrammed. The corresponding Monte Carlo distribution which has been normalized to the number of data events is indicated by $\diamond$s. A smoothing function was used to join the Monte Carlo points as a guide to the eye.

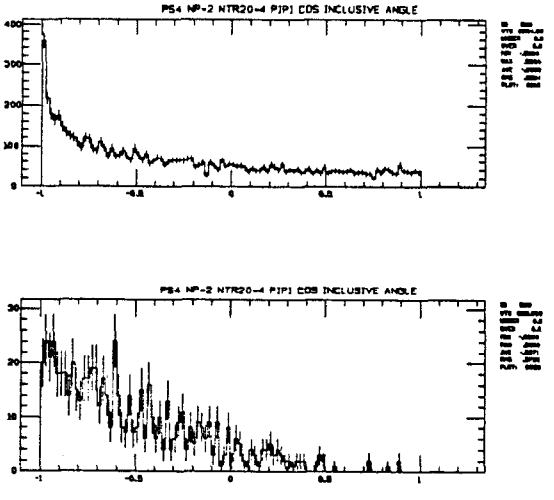

Fig. 4.5 cos $\theta_{\pi\pi}$ distribution for pion pairs found by PHYSAC. The top plot shows the distribution obtained from the final $\Upsilon(2S)$ data sample. The bottom plot gives the corresponding distribution for Monte Carlo events.

4.3.4 *Missing Mass Distributions*

The missing mass distribution for the final data sample and Monte Carlo $\Upsilon' \rightarrow \pi^0\pi^0\Upsilon(\Upsilon \rightarrow \text{unseen})$ is plotted in figure 4.6. This is the recoil mass opposite to the observed $\pi^0\pi^0$ system. The computed energy and momentum of this system is based on the fitted π^0 directions and energies as determined by the PHYSAC routine. In this work, the Υ' was assumed to have a mass of 10022. MeV. The measured mass is now known to be $10023.1 \pm .4$ MeV.[7] The appropriate formula for the missing mass is then:

$$M_X = \sqrt{(M_{\Upsilon'} - E_{\pi\pi})^2 - \vec{P}_{\pi\pi}^{\,2}} \qquad [4.27]$$

A peak is observed in the region suggested by the Monte Carlo distribution. Many fits to this peak were made assuming a flat background, a linear background and a quadratic background. All of these backgrounds can be fit to the data with $\chi^2/d.f. < 1$. Table 4.3 presents the results of fits to the distribution in figure 4.6 for flat, linear and quadratic backgrounds in which the width and mass of the peak were free parameters or were constrained to the Monte Carlo values. Figure 4.7 graphically illustrates the relationship between the gaussian amplitudes and means for the Monte Carlo fixed-width fits performed in this table. The three fits with free gaussian means and fixed widths are presented in figures 4.8-4.10. The fit with a quadratic background and fixed Monte Carlo width (fig. 4.10) will be used to estimate the number of observed events in the Upsilon missing mass region due to its small ratio of χ^2 to degrees-of-freedom and the fact that its amplitude is consistent with the values obtained from the other fits in table 4.3. The number of $\Upsilon \rightarrow$Unseen decay events is then

$$N_{\Upsilon \rightarrow Unseen} = 141. \pm 36. \quad . \qquad [4.28]$$

Fit	Mass (MeV)	Width (MeV)	Events	$\chi^2/d.f$
Flat Background				
MC mean,width	$9452. \pm .0$	$13.0 \pm .0$	$154. \pm 33.$	.58
MC width	$9445. \pm 4.$	$13.0 \pm .0$	$168. \pm 33.$	.38
Free	$9443. \pm 4.$	17.3 ± 5.1	$203. \pm 58.$	.34
Linear Background				
MC mean,width	$9452. \pm .0$	$13.0 \pm .0$	$146. \pm 28.$	.53
MC width	$9444. \pm 4.$	$13.0 \pm .0$	$160. \pm 33.$	.32
Free	$9443. \pm 4.$	17.2 ± 5.0	$196. \pm 57.$	.28
Quadratic Background				
MC mean,width	$9452. \pm .0$	$13.0 \pm .0$	$125. \pm 35.$	.39
MC width	$9445. \pm 4.$	$13.0 \pm .0$	$141. \pm 36.$	.24
Free	$9444. \pm 5.$	15.0 ± 5.0	$159. \pm 56.$	.24

Table 4.3 Gaussian fit to missing mass distributions for final event sample events. Flat, linear and quadratic backgrounds are assumed in these fits. The gaussian mean (mass) and width are either free parameters or constrained to the Monte Carlo values. The last column indicates the χ^2 for the fit divided by the number of degrees-of-freedom.

The mass of the peak is about 2σ away from the expected location of the Υ from Monte Carlo events when the gaussian mean is allowed to go free. This may be an indication that the peak does not, in fact, correspond to the process $\Upsilon' \rightarrow \pi^0\pi^0\Upsilon$, $\Upsilon \rightarrow$Unseen, or the mass difference may just be due to a statistical fluctuation. Figures 4.11,4.12 and 4.13 illustrate the relationship between the missing mass and the $\pi\pi$ system energy, mass and total momentum. The transverse momentum distribution versus missing mass is shown in figure 4.14. The Monte Carlo event distribution is consistent with this plot in the signal missing mass range as seen in figure 4.15.

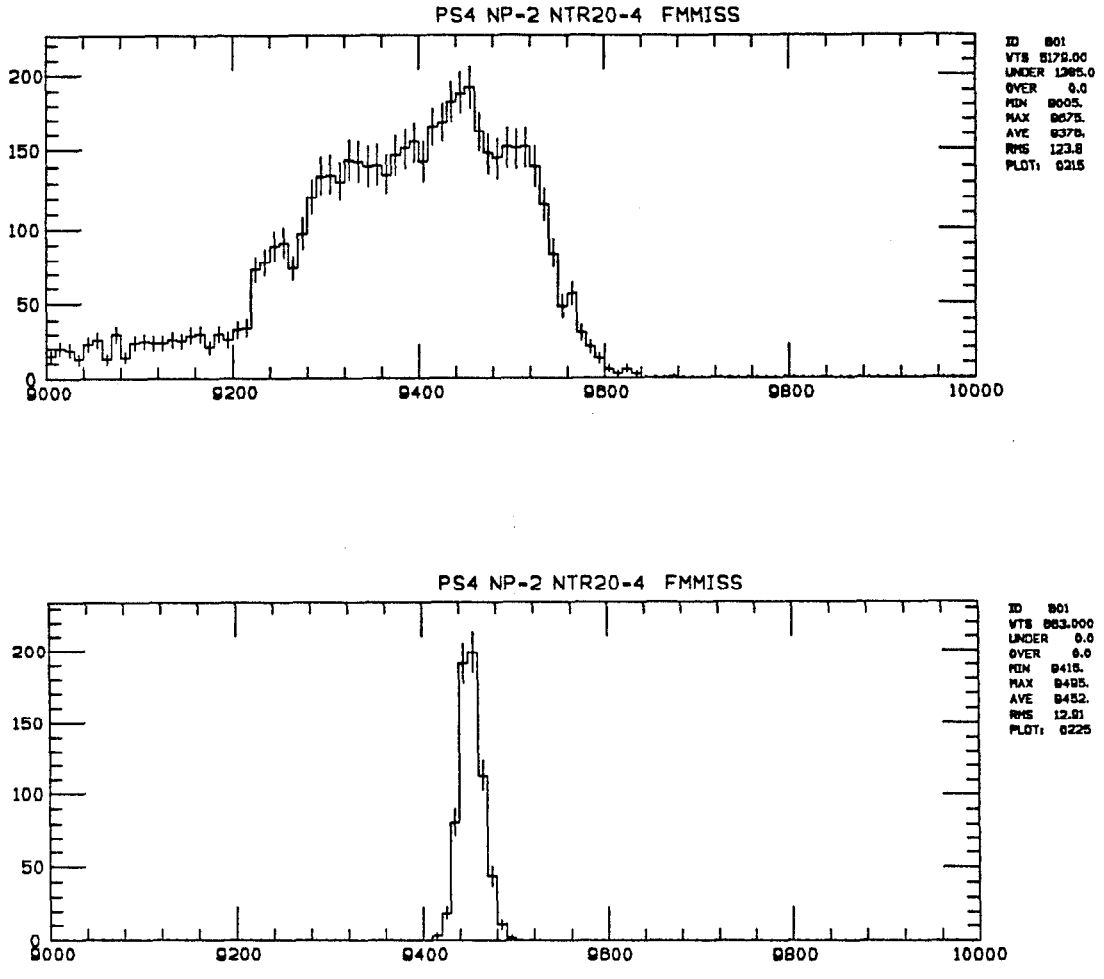

Fig. 4.6 Missing mass distribution for π^0pairs found by PHYSAC. The top plot shows the distribution obtained from the final $\Upsilon(2S)$ data sample. The bottom plot gives the corresponding distribution for Monte Carlo events. The number of Monte Carlo events is not normalized to the data.

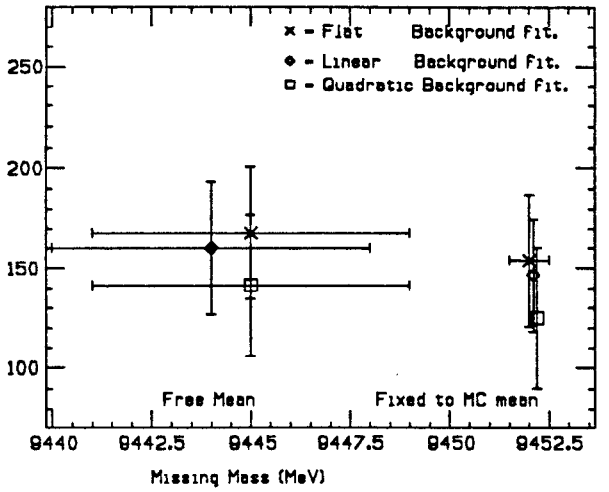

Fig. 4.7 Gaussian Amplitudes and means for fixed MC width fits performed in table 4.3. The ordinate indicates the gaussian amplitude of a given fit. The vertical scale has been truncated and does not include zero amplitude. (See table 4.3 for fit details.)

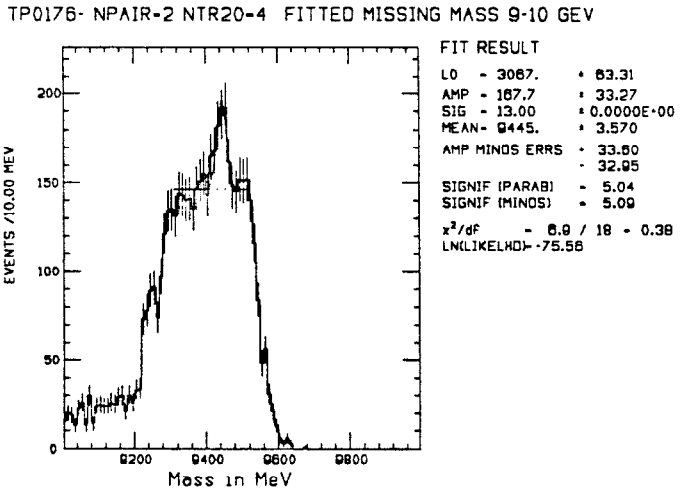

Fig. 4.8 Fit to the Missing mass distribution of figure 4.6. A flat background distribution is assumed and the gaussian width is fixed to the Monte Carlo value.

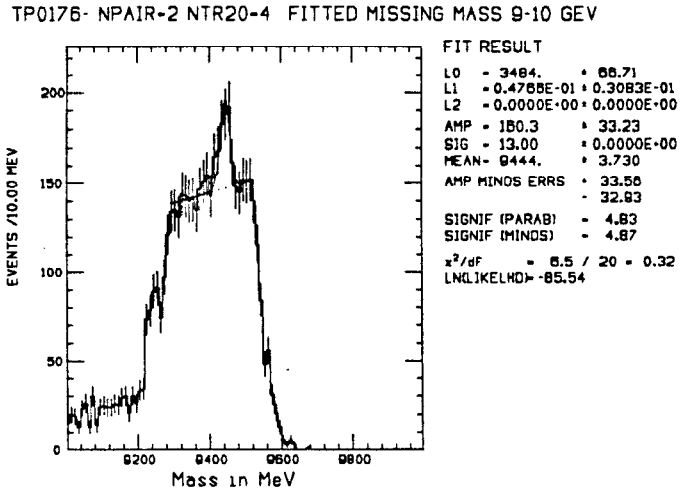

Fig. 4.9 Fit to the Missing mass distribution of figure 4.6. A linear background distribution is assumed and the gaussian width is fixed to the Monte Carlo value.

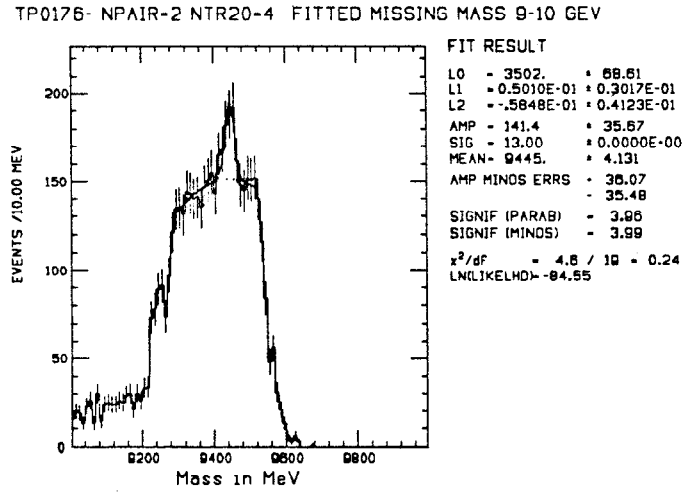

Fig. 4.10 Fit to the Missing mass distribution of figure 4.6. A quadratic background distribution is assumed and the gaussian width is fixed to the Monte Carlo value.

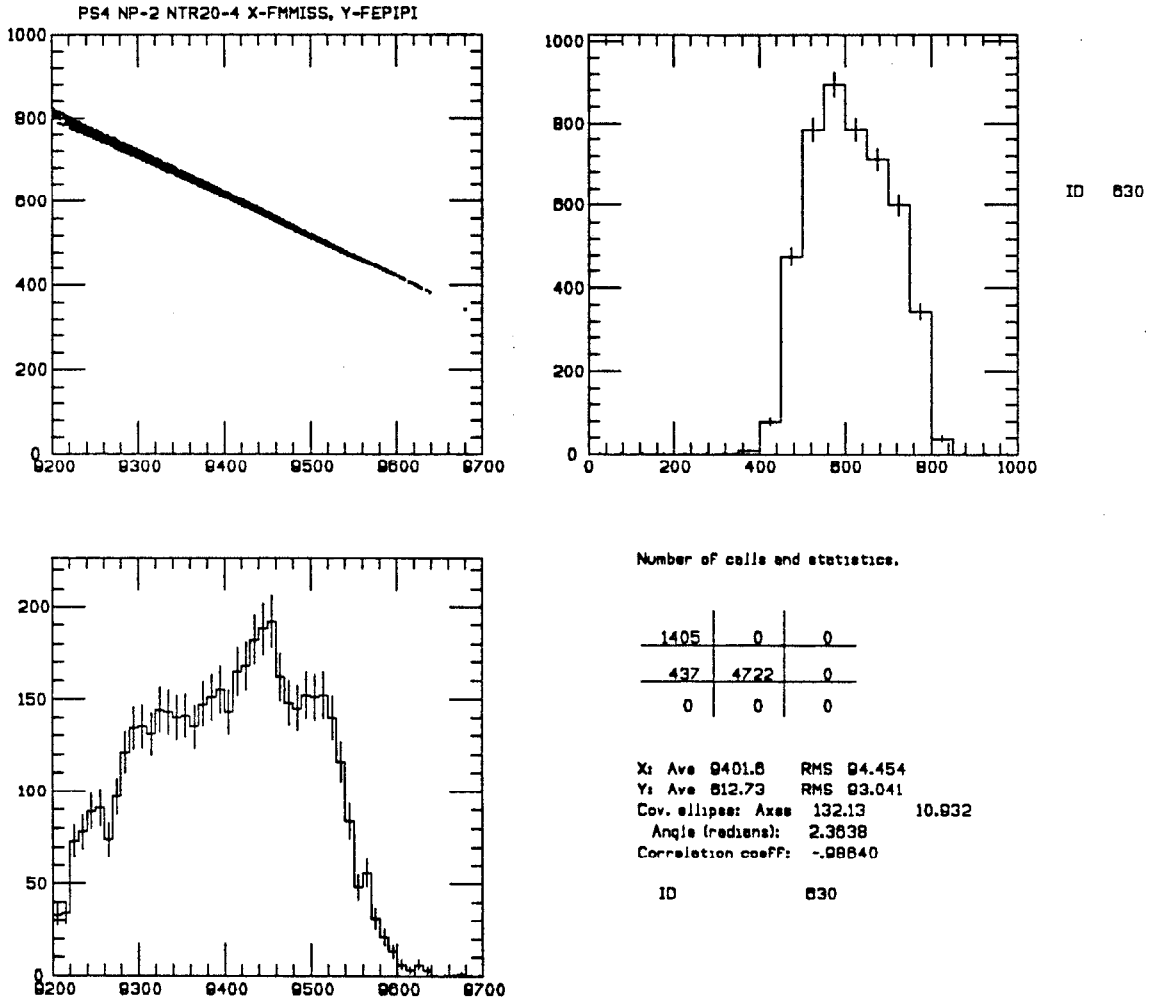

Fig. 4.11 $\pi^0\pi^0$ system energy vs missing mass for events in the final data sample. Energy is plotted on the y-axis and missing mass on the x-axis. All energies or masses are given in MeV.

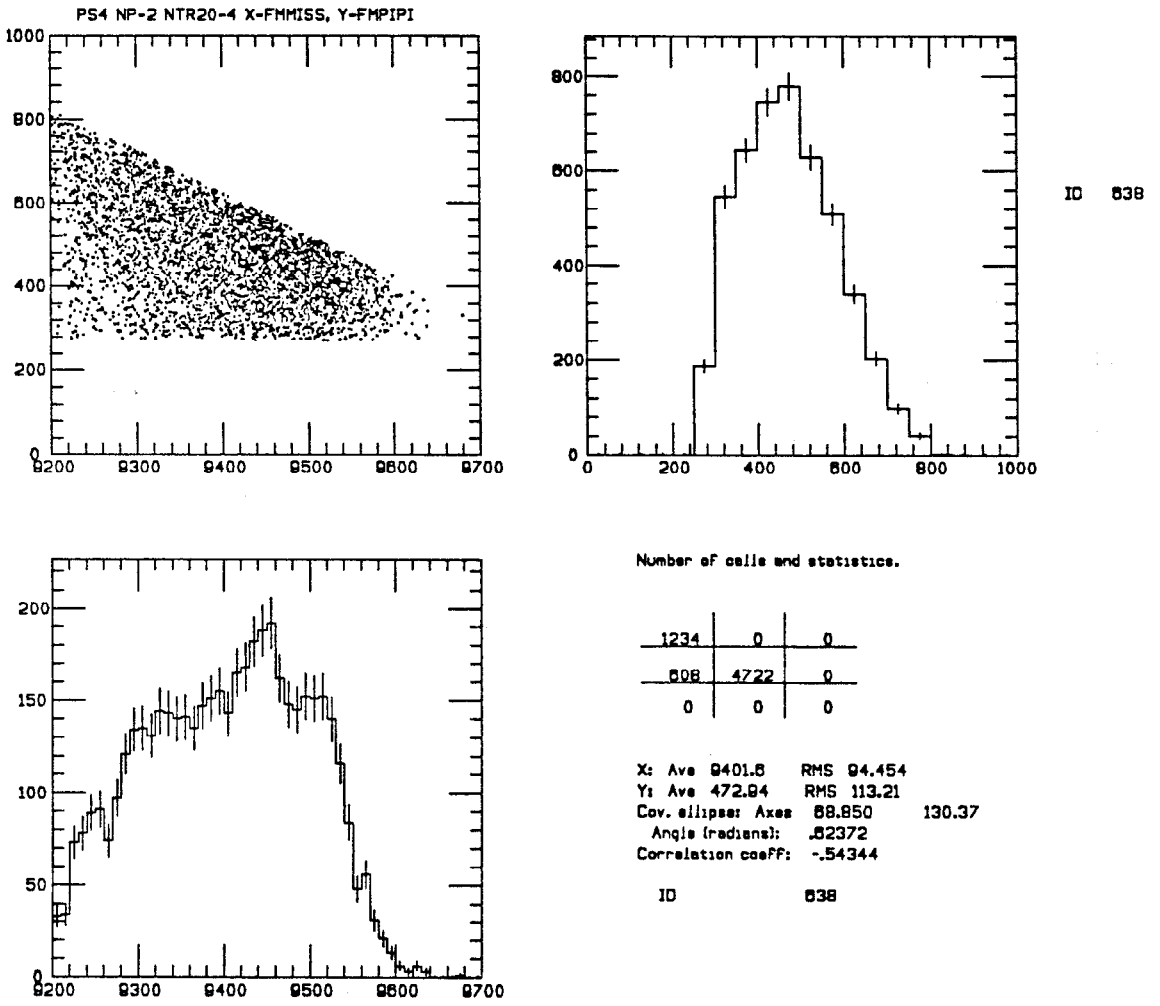

Fig. 4.12 $\pi^0\pi^0$ system mass vs missing mass for events in the final data sample. $M_{\pi\pi}$ is plotted on the y-axis and missing mass on the x-axis. All masses are given in MeV.

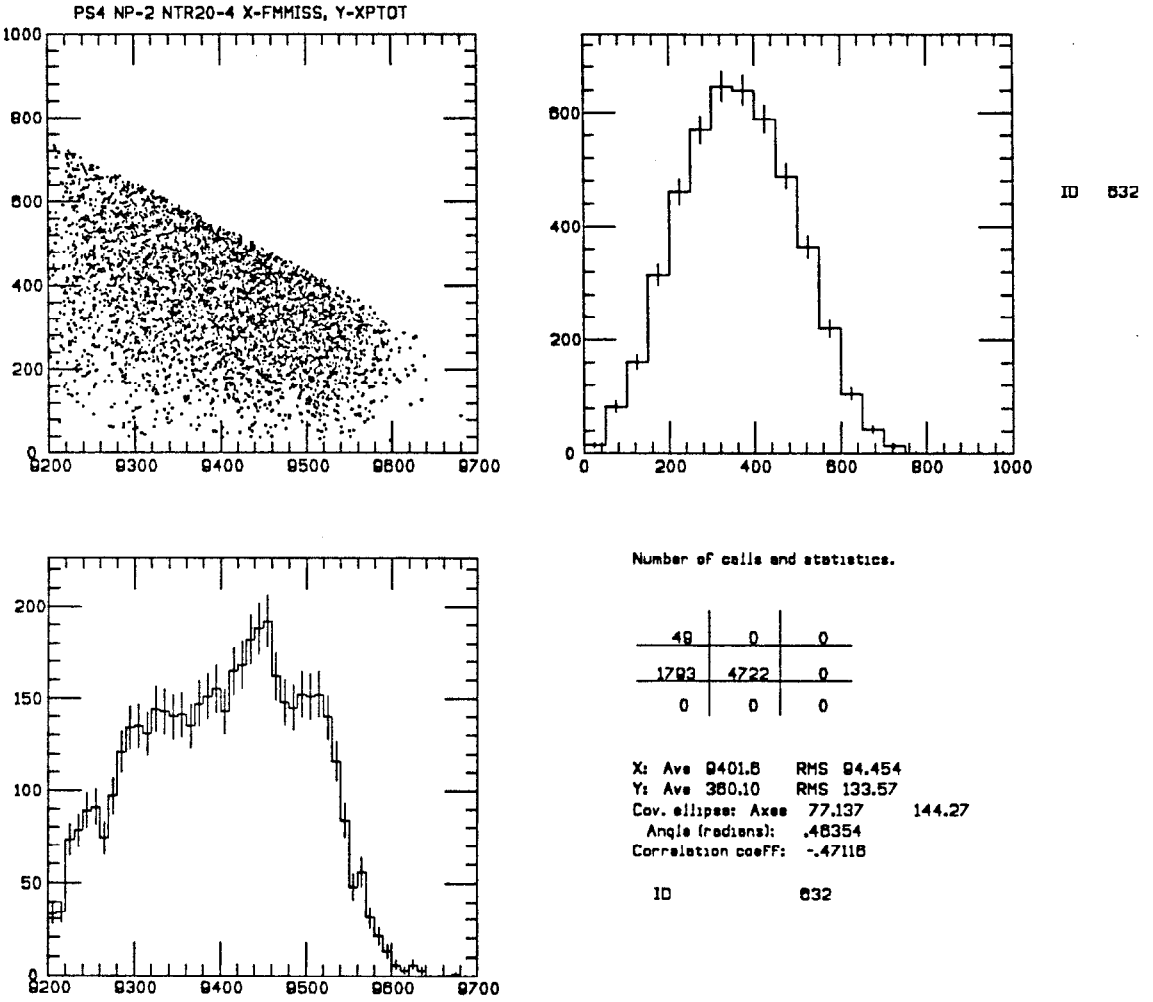

Fig. 4.13 $\pi^0\pi^0$ system total momentum vs missing mass for events in the final data sample. Momentum (MeV/c) is plotted on the y-axis and missing mass (MeV/c^2) on the x-axis.

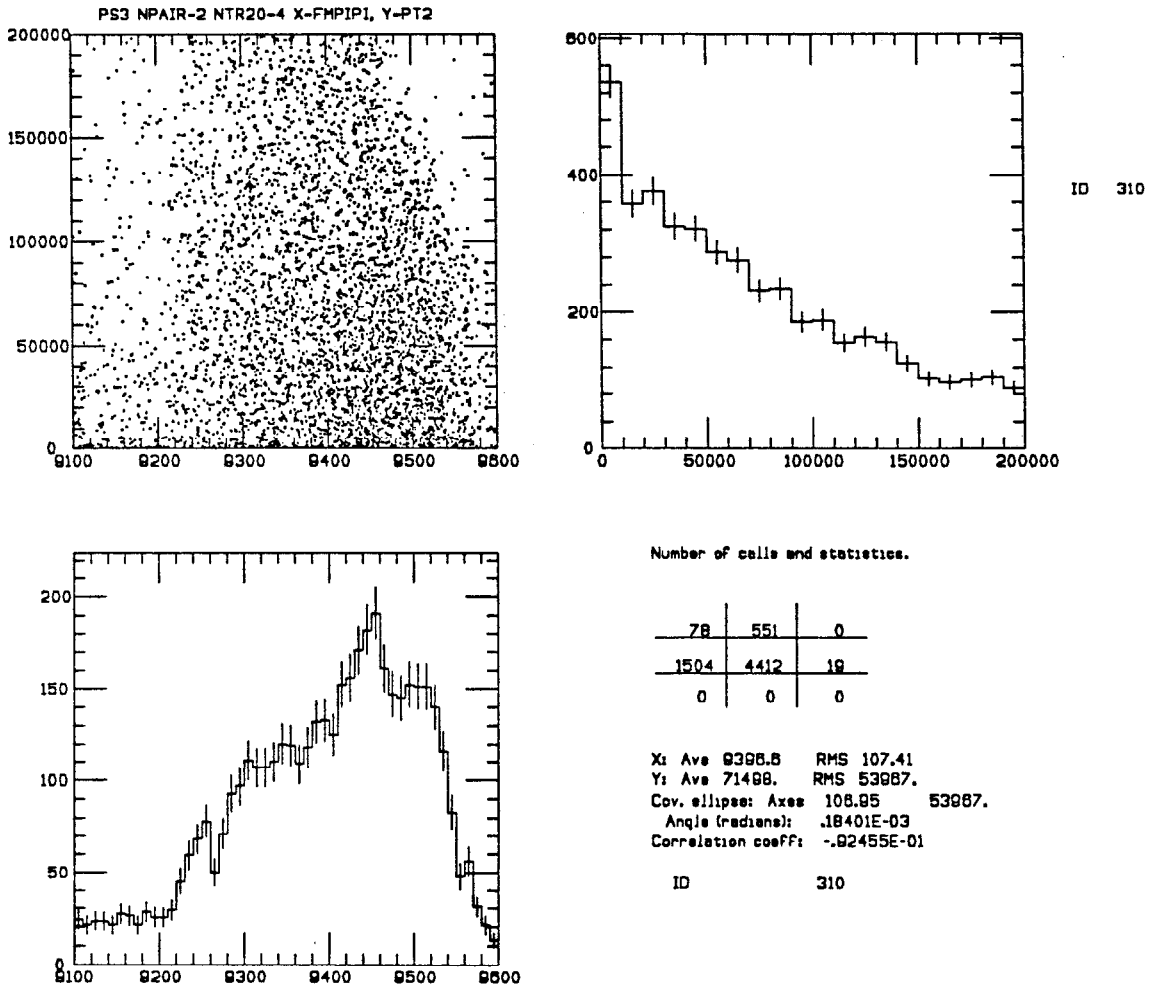

Fig. 4.14 $\pi^0\pi^0$ system transverse momentum-squared vs missing mass for events in the final data sample. Momentum-squared $(MeV/c)^2$ is plotted on the y-axis and missing mass (MeV/c^2) on the x-axis. The events populating the low recoil mass part of the distribution tend to have higher transverse momentum and so are depleted by the arbitrary limit of $P_T^2 < 200000.$ $(MeV/c)^2$ on the vertical scatterplot axis.

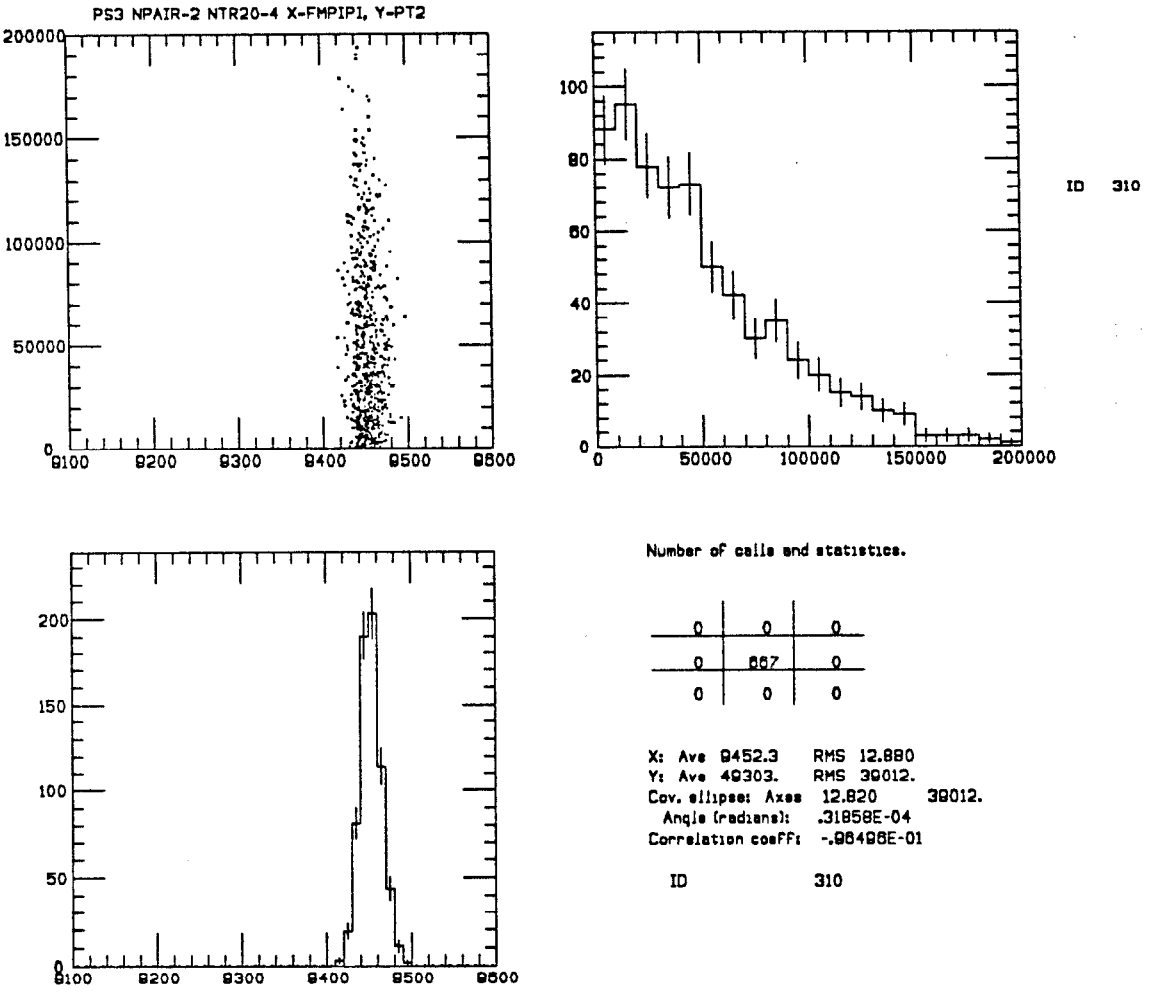

Fig. 4.15 $\pi^0\pi^0$ system transverse momentum-squared vs missing mass for Monte Carlo Events. Momentum-squared $(MeV/c)^2$ for $\Upsilon' \rightarrow \pi^0\pi^0\Upsilon$, $\Upsilon \rightarrow$Unseen Monte Carlo events is plotted on the y-axis and missing mass (MeV/c^2) on the x-axis.

4.3.5 *Acceptance Correction*

In order to model the acceptance of the analysis programs and trigger system as a function of missing mass, seven Monte Carlo data sets were generated according to the process:

$$\Upsilon' \rightarrow \pi^0\pi^0 X \qquad X \rightarrow \text{Unseen} \qquad [4.29]$$

where the mass of the unseen particle X was fixed at 40 MeV intervals from 9280 to 9520 MeV. These Monte Carlo events were used to calculate the analysis + detector efficiency as shown in figure 4.16. The obtained curve indicates that the analysis + detection efficiency decreases extremely rapidly in the missing mass region near the Upsilon mass. The acceptance corrected missing mass distribution was derived from this curve giving the result seen in figure 4.17. A gaussian peak was fitted to this distribution giving a peak amplitude of 1627 ± 840 events as seen in table 4.4. In order to evaluate the possible effect of an energy scale shift on trigger and analysis calculations, the acceptance-correction function was shifted by ± 10 MeV and the two resulting acceptance-corrected missing-mass distributions were then refit to determine the change in χ^2. The results of these fits are included in table 4.4 and the fits are shown in figures 4.18-4.20.

	Energy Shift		
Result	-10 MeV	0 MeV	+10 MeV
Mean Mass (MeV)	9446.± 5.	9446.± 4.	9446.± 4.
Amplitude (Events)	1035.± 302.	1153.± 323.	1352.± 335.
Significance (σ)	3.4	3.6	3.9
χ^2	4.4	4.7	5.9

Table 4.4 Gaussian fit to the acceptance-corrected missing mass distribution. The correction function is translated by ±10 MeV in order to investigate the sensitivity of the analysis and trigger system to variations in the energy scale. The correction does not include the efficiency of the charged particle cut.

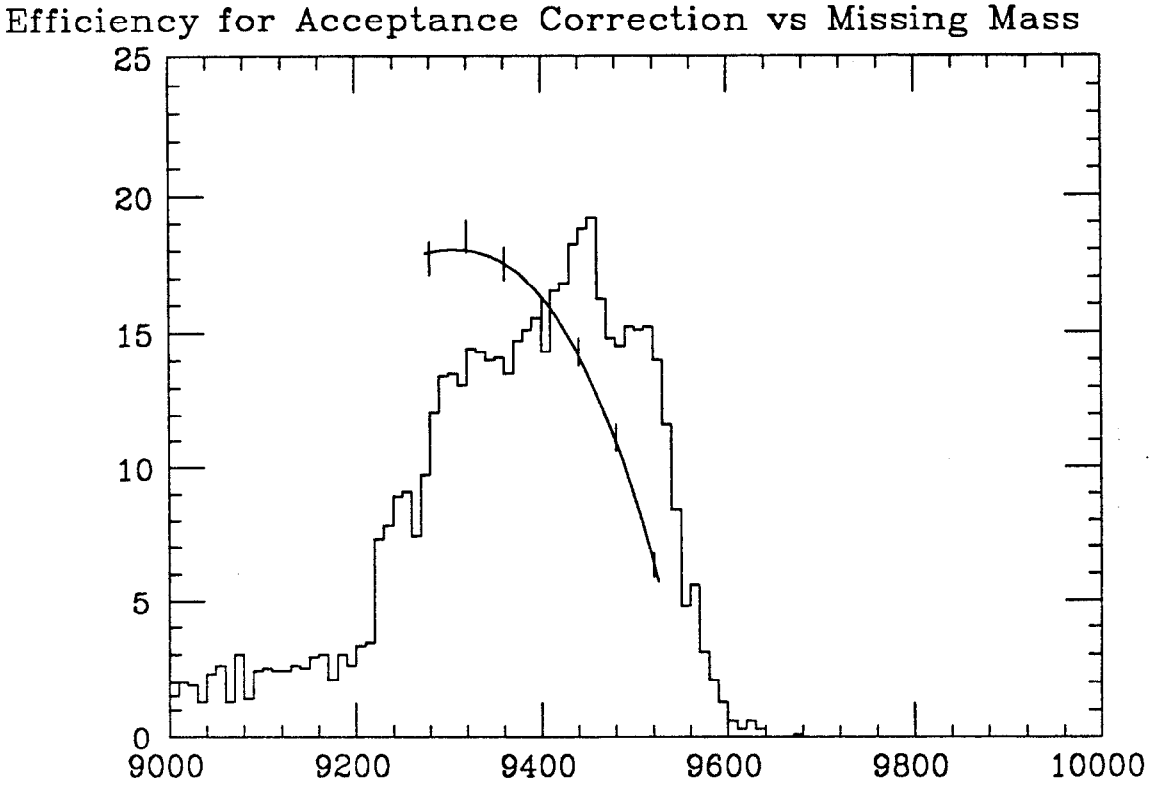

Fig. 4.16 Detector + Analysis efficiency versus M_X. The efficiency for the process $\Upsilon' \rightarrow \pi^0\pi^0$ X, where X is unseen, is plotted as a function of M_X in %. Missing mass is indicated in MeV/c^2. The missing mass histogram has an arbitrary scale factor. It shown as an indication of the change in efficiency over the missing mass range in question. The efficiency for the charged particle cut has not been included.

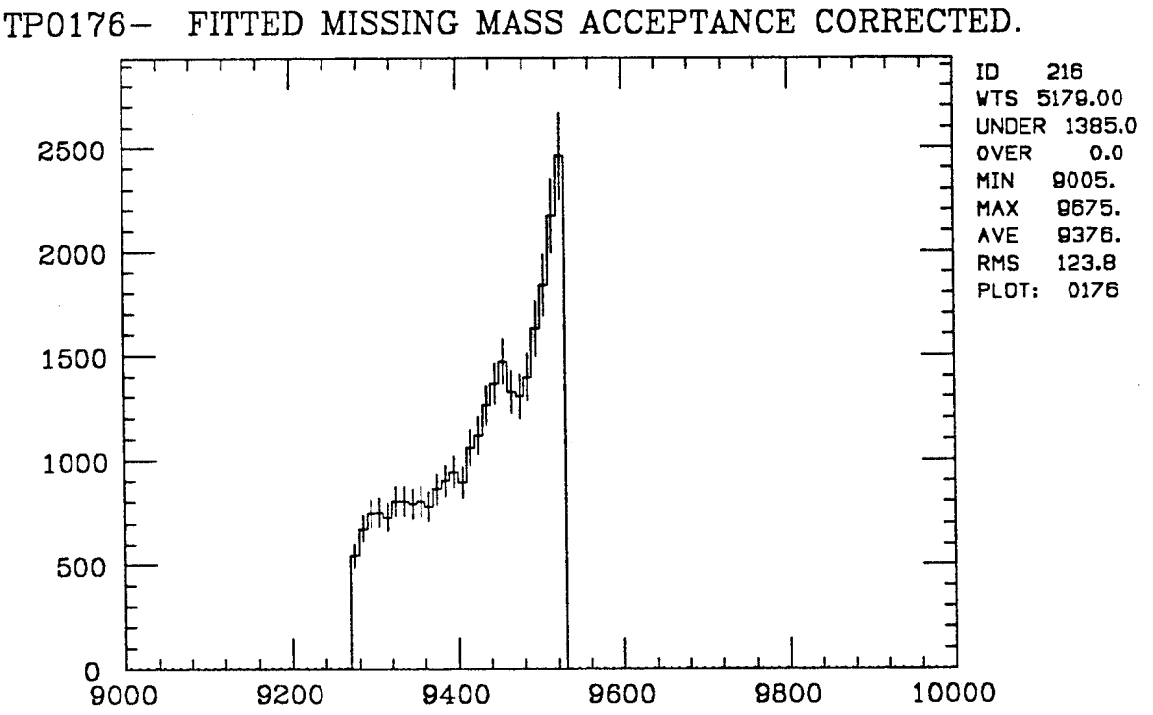

Fig. 4.17 Acceptance Corrected Missing Mass Distribution. Mass is given in MeV. The detector + analysis efficiency plotted in fig. 4.16 has been used to estimate the acceptance corrected event distribution. No correction was included for the charged particle cut. The error bar assigned to each bin is linearly weighted by the correction function for that bin.

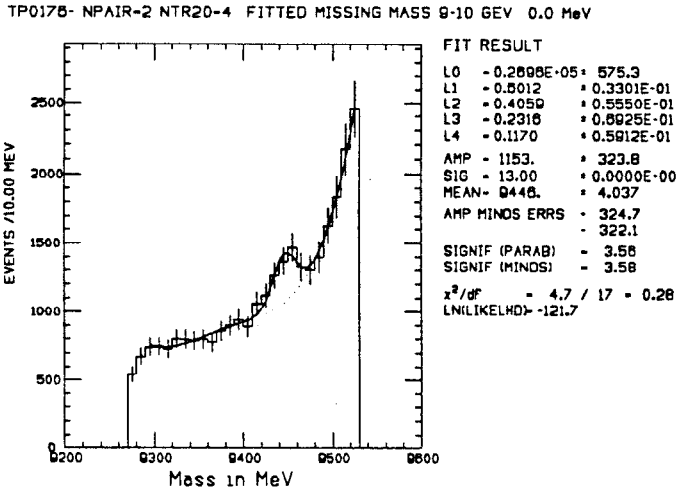

Fig. 4.18 Fit to Acceptance Corrected Missing Mass Distribution. The distribution obtained in figure 4.17 has been fitted to a gaussian peak plus a 5 term legendre polynomial background. The number of events obtained includes the Monte Carlo efficiency but no correction was included for the charged particle cut.

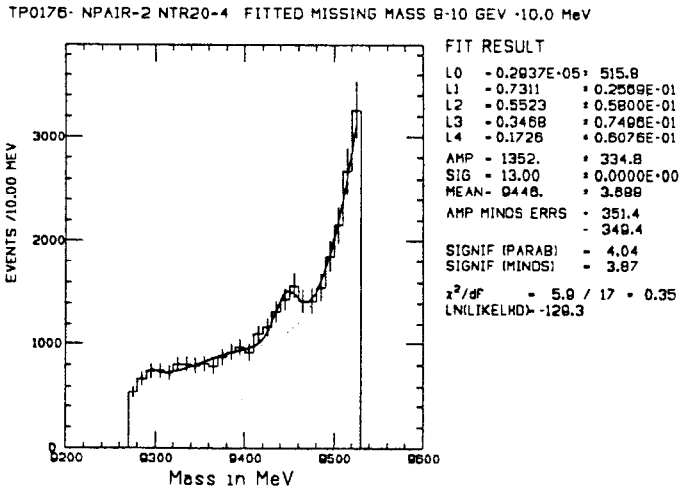

Fig. 4.19 Fit to Acceptance Corrected Missing Mass Distribution (+10 MeV Shift). The distribution obtained in figure 4.17 has been fitted to a gaussian peak plus a 5 term legendre polynomial background. The number of events obtained includes the Monte Carlo efficiency but no correction was included for the charged particle cut. The acceptance-correction function has been shifted by +10 MeV.

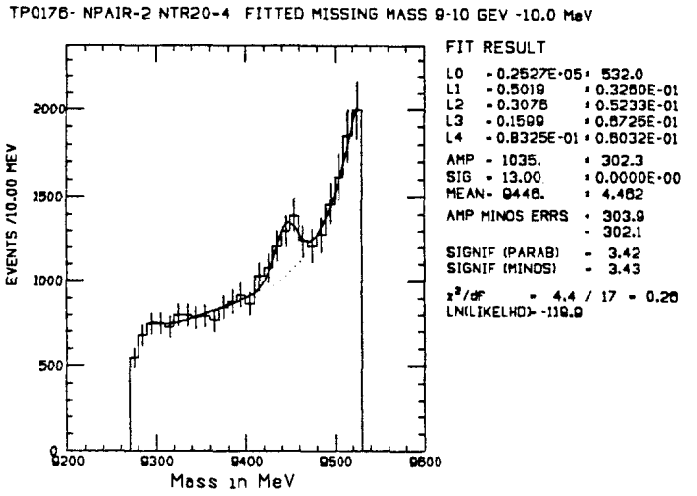

Fig. 4.20 Fit to Acceptance Corrected Missing Mass Distribution (-10 MeV Shift). The distribution obtained in figure 4.17 has been fitted to a gaussian peak plus a 5 term legendre polynomial background. The number of events obtained includes the Monte Carlo efficiency but no correction was included for the charged particle cut. The acceptance-correction function has been shifted by -10 MeV.

4.4 Contribution from Other Processes

In this section, decays of the Υ to lepton pairs will be considered as a contributing process to the observed $\Upsilon \rightarrow$Unseen signal as well as the possible contribution due to two photon continuum production of the η and $\eta\prime$ mesons.

4.4.1 *Monte Carlo Estimate of* $\Upsilon \rightarrow$ *Lepton Pairs*

The major contribution to the $\Upsilon \rightarrow$Unseen signal is expected to be from the process:

$$\begin{array}{l} \Upsilon' \rightarrow \pi^0\pi^0\Upsilon \\ \qquad\qquad\quad \Big\lfloor\!\!\longrightarrow l^+l^- \quad , \end{array} \qquad [4.30]$$

where $l^+l^- = e^+e^-, \mu^+\mu^-$, or $\tau^+\tau^-$. Since the lepton pairs will be created nearly back-to-back with a $1+\cos^2\theta$ angular distribution, there is some possibility that neither lepton will enter the central detector. If the lepton pair or daughter particles (in the case of τ decays) are contained within $|\cos\theta| > .93$, they will either continue out the beampipe or enter the endcaps. In this case the event may be included in the final event sample. From table 4.1, 117 Monte Carlo $\Upsilon' \rightarrow \pi^0\pi^0\Upsilon$, $\Upsilon \rightarrow l^+l^-$ events survive the final sample cuts out of 15000 generated events. The average efficiency for detecting $\Upsilon \rightarrow l^+l^-$ events may then be obtained by taking the ratio of these two numbers. This gives an detection and analysis efficiency for $\pi^0\pi^0 l^+l^-$ events of

$$\epsilon^{MC}_{l^+l^-} = .0078 \pm .0007\,. \qquad [4.31]$$

The expected number of these events based on the Monte Carlo simulation from 141,000 Υ' events is then:

$$\begin{aligned} N^{MC}_{ll} &= N_{\Upsilon'} \times BR(\Upsilon' \rightarrow \pi^0\pi^0\Upsilon) \times 3. \times BR(\Upsilon \rightarrow e^+e^-) \times \epsilon^{MC}_{l^+l^-} \\ &= 9.2 \pm 2.4 \quad , \end{aligned} \qquad [4.32]$$

where

$$N_{\Upsilon'} = (141. \pm 7.) \times 10^3 \ , \qquad [4.33]$$

$$BR(\Upsilon' \to \pi^0\pi^0\Upsilon) = .53 \times (18.8 \pm 1.0) \times 10^{-2} \qquad (Ref.\ 1) \qquad [4.34]$$
$$= (10.0 \pm .5) \times 10^{-2} \ ,$$

and

$$BR(\Upsilon \to e^+e^-) = (2.8 \pm .2) \times 10^{-2} \ . \qquad (Ref.\ 8) \qquad [4.35]$$

The calculation in eqn. [4.34] takes the world average of BR($\Upsilon' \to \pi^+\pi^-\Upsilon$) and assumes isopin conservation plus some phase space weighting of the $\pi^0\pi^0$ decay mode.[1] The Monte Carlo simulation therefore predicts that no more than 9 of the 140+ events in figure 4.6 (**before acceptance correction**) can be accounted for by means of leptonic decays of the Υ.

An order of magnitude estimate of this number is obtained by considering the available solid angle for escaping lepton pairs. The fraction of lepton pairs which are produced within the solid angle from $.93 < |\cos\theta| \leq 1.0$ can be obtained by integrating the $1 + \cos^2\theta$ angular dependence. The solid angle fraction is then

$$\Delta\Omega \sim 10\% \quad . \qquad [4.36]$$

Assuming that the analysis and trigger efficiency for the resulting π^0 pair is less than 20% (generously above the MC efficiency estimate of 12.2% from table 4.2) the expected number of lepton pair events is no more than

$$N_{ll}^{tunnel} = N_{\Upsilon'} \times BR(\Upsilon' \to \pi^0\pi^0\Upsilon) \times 3. \times BR(\Upsilon \to e^+e^-) \times \epsilon_{\pi\pi}^{Analysis} \times \Delta\Omega$$
$$= 18.9 \text{ events.} \qquad [4.37]$$

Thus the solid angle of the hole region (within $|\cos\theta| < .93$) is inadequate to explain the large number of $\Upsilon \to$Unseen candidate events. (As mentionned earlier, energy deposition ($>\sim 40MeV$) in the solid angle covered by the tunnel region crystals is vetoed at the trigger level. See appendix A for details.)

The acceptance for escaping lepton pairs also includes the gap between the two hemispheres of the central detector. The Monte Carlo simulation used in this study incorporates an air gap of 3 mm. It allows as well for each hemisphere's $\frac{1}{16}$ inch equator washer. At the inner radius of 25 cm, the Monte Carlo gap is equivalent to

$$\Delta^{MC}\phi = .02 \quad \text{(radians)}. \qquad [4.38]$$

Particles within this angular range will probably not be detected with reasonable efficiency. Because the angles assigned to charged tracks are derived from the tube chamber information, they can be used to determine the relationship between ϕ and energy deposition in the central detector. For this reason, charged tracks with more than 1. GeV energy in the $\Upsilon(2S)$ data were used to study the extent of the inter-hemisphere gap. The result was that

$$\Delta^{2S}\phi \sim .03 \quad \text{(radians)}. \qquad [4.39]$$

Although this figure is slightly higher than that used in the Monte Carlo it represents only 1% of the total solid angle and so does not appreciably add to the result derived above.

An additional check for the decay $\Upsilon \rightarrow l^+l^-$ is to look for events in the final data sample in which high energy particles interact with the endcaps. Unfortunately the transversely stacked endcap crystals present at most 5 radiation lengths of material in the range $.99 <| \cos\theta |< .97$[9] and, on average, less. This implies that the electrons from the decay $\Upsilon' \rightarrow e^+e^-$ will typically deposit 1.5 GeV in an endcap and minimum ionizing muons from a leptonic decay will deposit less than 70 MeV in this region. This factor makes it difficult to separate high energy electrons from the ambient background of lower energy particles due to beam-related interactions. The endcaps furnish up to 10 radiation lengths of material in part of the region above $| \cos\theta |= .97$. Particles which interact in this region will be much more clearly separated from background.

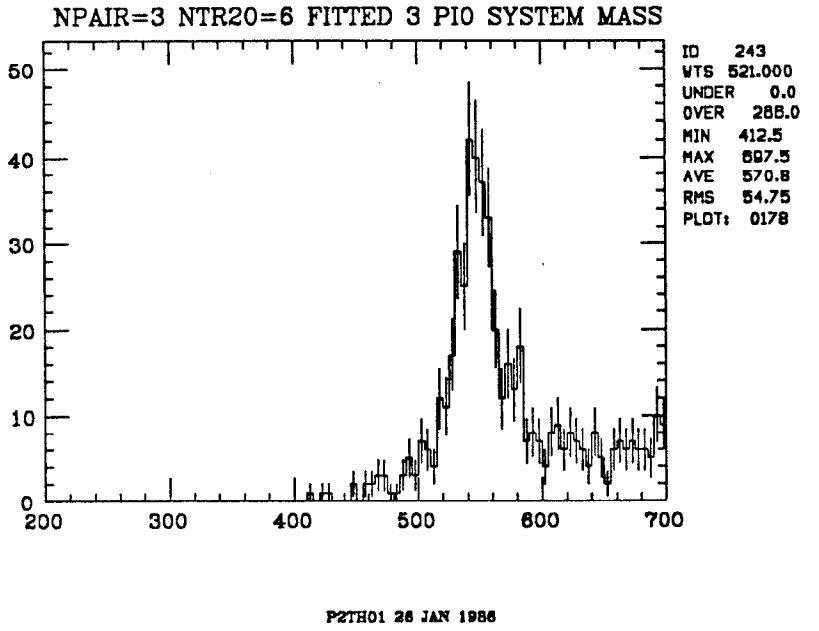

Fig. 4.21 $\pi^0\pi^0\pi^0$System Mass Distribution. Mass is given in MeV.

In the final data sample, only one event was found with more than 1 GeV in one of the endcap arrays. The Monte Carlo sample of 5000 $\Upsilon' \rightarrow \pi^0\pi^0 e^+e^-$ events also yielded one candidate event with more than 1 GeV in the endcap after detector simulation and final analysis cuts. This Monte Carlo event sample corresponds to 140 times the integrated luminosity in the final data sample which implies that endcap bhabha pairs from the $\pi^0\pi^0$ hadronic transition can not be efficiently detected. A sample of 48k random beam-crossing events taken during $\Upsilon(2S)$ running contained 5 events with more than 1 GeV. Since the final data set for this study includes 6500 beam-crossings (events), the unique endcap event is statistically compatible with the known background conditions at DORIS II.

4.4.2 *Two-photon Acceptance*

The reaction $\eta \rightarrow \pi^0\pi^0\pi^0$, where the η is produced via a two photon process, was used as a check of the experimental acceptance. Events in which PHYSAC found 3 π^0s and six tracks satisfying the same cuts (eqn. [4.8]) as those used in the four track final event sample were selected during the Pass 2 process. The mass

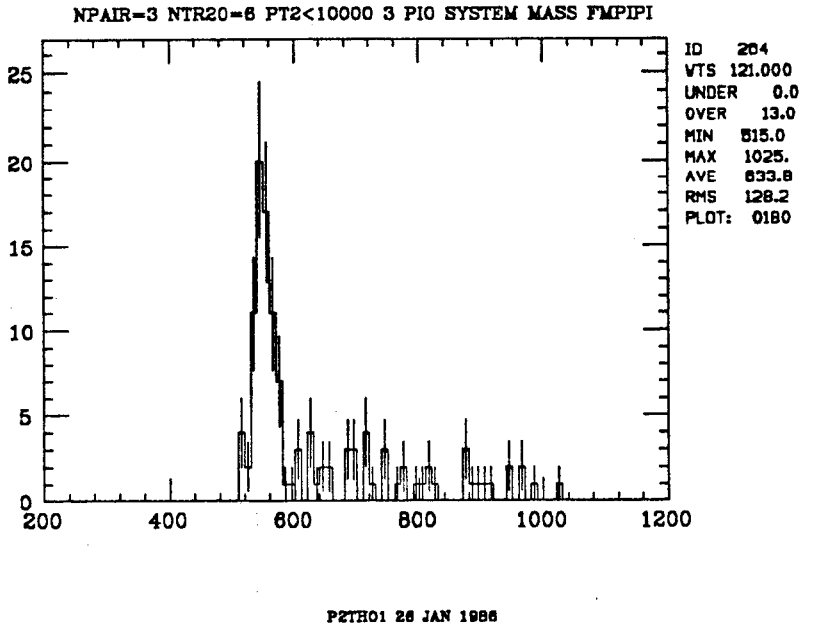

Fig. 4.22 $\pi^0\pi^0\pi^0$System Mass Distribution $P_T^2 < 10000$. Mass is given in MeV. A P_T cut has been made to remove non 2γ backgrounds.

Result	All $3\pi^0$ events	P_T cut
Mean Mass (MeV)	547.4± 1.5	550.4± 2.0
Width (MeV)	16.8± 1.6	14.4 ± 1.8
Amplitude (Events)	263.0± 23.6	65.3 ± 9.0

Table 4.5 Fit to $\eta \rightarrow \pi^0\pi^0\pi^0$ events.

of the $3\pi^0$ system for these events is plotted in Figure 4.21. Because 2γ events have very low transverse momentum, a cut on events with $P_T^2 > (100.\frac{MeV}{c})^2$ is used to remove most of the background events present. The $3\pi^0$ system mass for the remaining events is plotted in figure 4.22. A fit to these distributions gives the values found in table 4.5.

A Monte Carlo simulation of 9312 $\eta \rightarrow \pi^0\pi^0\pi^0$ events yielded 163 $3\pi^0$ candidate events after trigger simulation and analysis cuts and 114 events after the

$P_T^2 < 10000$ MeV cut. Since the latter selection removes almost all background events, it will be used as an estimate of the efficiency for selecting ηs. The detection and analysis efficiency based on the Monte Carlo simulation and exclusive of the charged particle cut is then

$$\epsilon_{3\pi^0}^{MC} = .012 \pm .001 \quad . \qquad [4.40]$$

This implies that 5500 ± 1200 $\eta \rightarrow 3\pi^0$ reactions took place during the $\Upsilon(2S)$ data taking covered by this study. Since $BR(\eta \rightarrow 3\pi^0)$ is $31.8 \pm .8\%$,[10] and the charged particle efficiency for six track events is $84.2 \pm 13.0\%$ by equation [4.21], approximately 20 ± 7 k ηs were originally created in two-photon reactions during this period. The 2γ width of the η has been measured to be ($.560 \pm .040$ KeV) in storage ring experiments.[11] Its 2γ cross section can be calculated to be[12]

$$\sigma_\eta^{\gamma\gamma} \sim (.72 \pm .06) nb \quad . \qquad [4.41]$$

In the 44.1pb^{-1} available for this study, about 32 (± 2) k η events should be produced. Although this number is a higher than the estimate from the data sample (but not statistically high) it serves to indicate that the detection and analysis efficiency calculations are at least approximately correct. In particular, the calculated efficiency is not excessively low.

A check on possible feed-down into the four track final event sample from two photon processes where a particle was lost or mistakenly used by PHYSAC to form a π^0 was made by using the $\eta \rightarrow 3\pi^0$ Monte Carlo sample referred to above and another Monte Carlo sample of $\eta\prime \rightarrow \pi^0\pi^0\eta$ events. 14 of the 9312 η events and 10 of the 10000 $\eta\prime$ events were classified by the analysis process as four track-$2\pi^0$ events. There was no apparent peaking near the Υ mass in the missing mass plot. These small branching ratios imply that the η and $\eta\prime$ do not contribute appreciably to the final data sample missing mass distribution. It is possible that a feed-down process exists for a higher lying meson but it is very

difficult to explain either the dipion background level or event accumulation near the Υ mass on this basis.

4.5 Conclusion

An effect is seen which is consistent with the decay mode: $\Upsilon' \rightarrow \pi^0\pi^0\Upsilon$, $\Upsilon \rightarrow$ Unseen. From equation [4.28], the amplitude of the effect is

$$N_{\Upsilon \rightarrow Unseen} = 141. \pm 36. \text{ (events)}, \qquad [4.42]$$

when the missing mass distribution of figure 4.6 is fit to a gaussian peak fixed to the Monte Carlo signal width (13 MeV) and a quadratic background. The detection and analysis efficiency from eqn. [4.24] is given by

$$\epsilon_{Analysis} = .122 \pm .011 \pm .010 \quad , \qquad [4.43]$$

where the last error represents the systematic uncertainty due to a possible shift in the energy scale used in the analysis as opposed to the energies used at the hardware level (estimated to be 8% from table 4.4). Because both the statistical and systematic uncertainties on the efficiency influence the magnitude of the computed branching ratio for $\Upsilon \rightarrow$ Unseen in this analysis, we combine them in quadrature for the purpose at hand to yield:

$$\epsilon_{Analysis} = .122 \pm .015 \quad . \qquad [4.44]$$

The branching ratio for $\Upsilon \rightarrow$ Unseen is given by

$$BR(\Upsilon \rightarrow Unseen) = \frac{N_{\Upsilon \rightarrow Unseen} - N_{ll}^{MC}}{\epsilon_{Analysis} N_{\pi^0\pi^0\Upsilon}} \quad . \qquad [4.45]$$

From Monte Carlo simulation, the expected signal from the decay mode $\Upsilon' \rightarrow \pi^0\pi^0\Upsilon$, $\Upsilon \rightarrow$ lepton pairs, is given by eqn. [4.32] as

$$N_{ll}^{MC} = 9.2 \pm 2.4 \pm .9 \quad , \qquad [4.46]$$

where a possible 10% uncertainty on the solid angle available to escaping lepton pairs ($.93 \leq |\cos\theta| \leq 1.$; $|\phi|$ or $|\phi - \pi| < .015$) has been added as a systematic error. As both the statistical and systematic errors on this number influence the desired branching ratio computation, we add them in quadrature to obtain:

$$N_{ll}^{MC} = 9.2 \pm 2.6 \text{ (events)}. \qquad [4.47]$$

Taking the number of $\Upsilon(2S)$ resonance events contained in the data sample available for this study from eqn. [4.33] and the branching ratio for $\Upsilon' \to \pi^0\pi^0\Upsilon$ from eqn. [4.34], yields the number

$$\begin{aligned} N_{\pi^0\pi^0\Upsilon} &= (141. \pm 7.) \times 10^3 \times (10.0 \pm .5) \times 10^{-2} \\ &= 14100 \pm 1410 \text{ (events)}. \end{aligned} \qquad [4.48]$$

The error on this number will contribute only to the systematic uncertainty on BR($\Upsilon \to$Unseen). Equation [4.45] may now be used to derive this branching ratio. Inserting the results of equations [4.42],[4.44],[4.47]and [4.48] into this equation produces the result:

$$\begin{aligned} BR(\Upsilon \to Unseen) &= \frac{(141 \pm 36) \; - \; (9 \pm 3)}{(.122 \pm .015)(14100)} \\ &= 7.7 \pm 3.2 \pm 0.8 \quad \% \quad , \end{aligned} \qquad [4.49]$$

where the first error represents a linear combination of the statistical and signal-related systematic errors, and the second is the systematic uncertainty due to the luminosity and BR($\Upsilon' \to \Upsilon\pi^0\pi^0$) normalization of equation [4.48]. Because of the unexpectedly large amplitude for this branching ratio as determined by the present analysis, and the possibility that a background process or systematic effect may be responsible for this effect, we choose to quote a 90% confidence level upper limit for the purpose of this thesis:

$$BR(\Upsilon \to Unseen) < 12\% \quad (90\% \text{ C.L.}). \qquad [4.50]$$

It is hoped that an independent analysis of the data sets used in this analysis will be undertaken in the near future as a check of this result and that a systematic study of the dipion background at DORIS II will be made at differing center-of-mass energies in order to determine the probable origin of this effect.

References

1) D. Gelphman Ph.D. Thesis, Measurement of the Decay $\Upsilon(2S) \rightarrow \pi^0\pi^0\Upsilon$, Stanford U. 1985, SLAC Report 286. Unpublished.

2) The CONTAG routine was written by Gary Godfrey of the Crystal Ball Collaboration.

3) M. Voloshin and V. Zakharov, *Phys. Rev. Lett.*,**45**, 688 (1980). See also.

T.M. Yan, *Phys. Rev. D.*, **22**, 1652 (1980), and

Y.P. Kuang and T.M. Yan, *Phys. Rev. D.*, **24**, 2874 (1981).

4) D. Besson, *Phys. Rev. D*, **30**, 1433 (1984)

5) R. Ford and W. Nelson, "The EGS Code System: Computer Programs for the Monte Carlo Simulation of Electromagnetic Cascade Showers (Version 3)," SLAC Report 210, June 1978.

6) R. Lee, Ph.D. Thesis, "Radiative Decays of the Psi Prime to All-photon Final States," Stanford U., 1985. SLAC Report-282. Unpublished.

7) D.P. Barber, *et al.*, *Physics Letters*, **135b**, 498 (1984).

8) D. Prindle, Ph.D. Thesis, "Measurement of the Resonance Parameters of the Υ and Υ' Mesons," Carnegie-Mellon U., 1985. Unpublished.

9) K. Konigsman, "Crystal Ball Note 257," 1981, SLAC.

10) Particle Data Group, *Reviews of Modern Physics*, **56**, S10 (1984)

11) H. Kolonoski, "Two Photon Processes," Invited Talk, 1985 Intl. Symposium on Lepton Photon Interactions, Kyoto, Japan,Bonn-HE-85-34, U. Bonn, Phys. Inst.

12) R. Clare, private communication, at 10 GeV c.m.,
$\sigma_{\gamma\gamma}(m_{Res} = 550.\ MeV) = (1.29 \pm .01)$ nb/KeV.

Chapter 5

Search for $\Upsilon' \rightarrow \pi^0\pi^0\Upsilon$, $\Upsilon \rightarrow \gamma$ + Unseen.

The techniques developed in the previous chapters for tagging Upsilons produced during the hadronic transition $\Upsilon' \rightarrow \pi^0\pi^0\Upsilon$, will be adapted in this chapter to the search for the reaction: $\Upsilon \rightarrow \gamma$+ Unseen. Because this process involves an additional photon which may deposit many GeV of energy, the analysis will be based on the use of a different trigger than that used in the previous process studied. The NTOPO trigger will be used for this purpose. Unlike the NMULT trigger which functions over a narrow energy range, its total energy condition demands only that an event exceed an energy threshold set at 800 MeV. (Details are presented in appendix A.) The available $\Upsilon(2S)$ luminosity for which this trigger was installed and running is 57.4 pb^{-1}. Crystal Ball runs from 9079 to 13230 are included in this data set which covers the period from February 1983 to February 1984.

5.1 Data Selection and Analysis

Events which survived the Pass 1 and CONTAG (charged particle) cuts 1-6 described in chapter 4 were then subjected to the following cuts after making the ELOG energy correction (eqn. 3.2) on photon energies.

7) Events were triggered by NTOPO. [5.1]

8) # photons (with $E_{13} > 20$ MeV and $|\cos\theta_{track}| < .85$) $= 5$. [5.2]

9) # π^0s found by PHYSAC = 2. [5.3]

These cuts are very nearly equivalent to those used in chapter 4. The only difference is that NTOPO trigger events are selected so that the full photon energy range above a few hundred MeV may be covered and five photons are selected instead of four. Approximately 347 $\Upsilon(2S)$ production tapes were scanned during Pass 1. 13,384 NTOPO trigger events with 2 or more π^0s remaining after the energy correction step and 7,452 of these events remained after cuts 7-9.

5.2 Detection and Analysis Efficiency

The detection and analysis efficiency for this process was evaluated by means of Monte Carlo simulation of the decay

$$\begin{array}{l} \Upsilon' \rightarrow \pi^0\pi^0\Upsilon \\ \qquad\qquad\quad \big\lfloor\!\!\longrightarrow \gamma + Unseen \end{array} \qquad [5.4]$$

Particle 4-vectors were generated with the same dipion system parameters as were used in the chapter 4 analysis but the Upsilon was constrained to decay into a monoenergetic photon and unseen particles. The photons were generated with a $1 + \cos^2\theta$ distribution in the Upsilon rest frame. This is the expected angular distribution for $\Upsilon \rightarrow \gamma +$ axion decays. The choice of this distribution provides a worst-case estimate of the analysis efficiency for decay processes which have a less severe $\cos\theta$ dependence. The beam polarization was assumed to be 70% as in chapter 4. Figure 5.1 illustrates the detector plus analysis efficiency over the photon energy range of 400- 5000 MeV as determined via these five Monte Carlo Data sets. A linear fit was performed to these points yielding a χ^2 per degree of freedom of .5 . The parameters obtained from this fit are used to estimate the efficiency over the entire photon energy range of interest. The error on the efficiency function over this range was evaluated by considering parallel straight-line fits to the same points. The error on this function is taken to be 2.25 % of the value determined by means of the fit parameters. Table 5.1 contains the

Cuts	γ Energy (MeV) 500	700	1000	2500	5000
Initial	5000	5000	5000	4304	2508
Trigger	1708	1732	1707	1406	773
EOTAP	1270	1231	1229	1404	773
Pass 1	885	842	784	620	314
Final	570	551	545	465	226

Table 5.1 $\Upsilon \rightarrow \gamma +$ Unseen Monte Carlo Data Sets and Applied Cuts. The number of surviving Monte Carlo events for each data set is displayed for each cut.

number of Monte Carlo events surviving all but the charged particle cuts for the five data sets generated in this study. The efficiency for the CONTAG charged particle cut for the five track events in this data sample is taken from eqn. 4.21 to be

$$\epsilon_{Charge}^{5Track} = 88.0 \pm 8.8\ \%. \qquad [5.5]$$

5.3 Results

5.3.1 π^0 and $\pi^0\pi^0$ System Angular and Kinematic Distributions.

Figure 5.2 shows the distribution formed by plotting the masses formed by all unique pairings of two photon tracks in the NTOPO data sample. The $\cos\theta$ angular distribution of the pions found by PHYSAC in this sample is shown in figure 5.4. As in the chapter 4 analysis, a peaking toward -Z is observed, indicating the presence of an assymmetric, beam-related background. The dipion pion system formed from the PHYSAC π^0s displays a peaking toward high mass ($\cos\theta_{\pi\pi} \rightarrow -1$) as seen in figure 5.5. The mass distribution of the dipion system

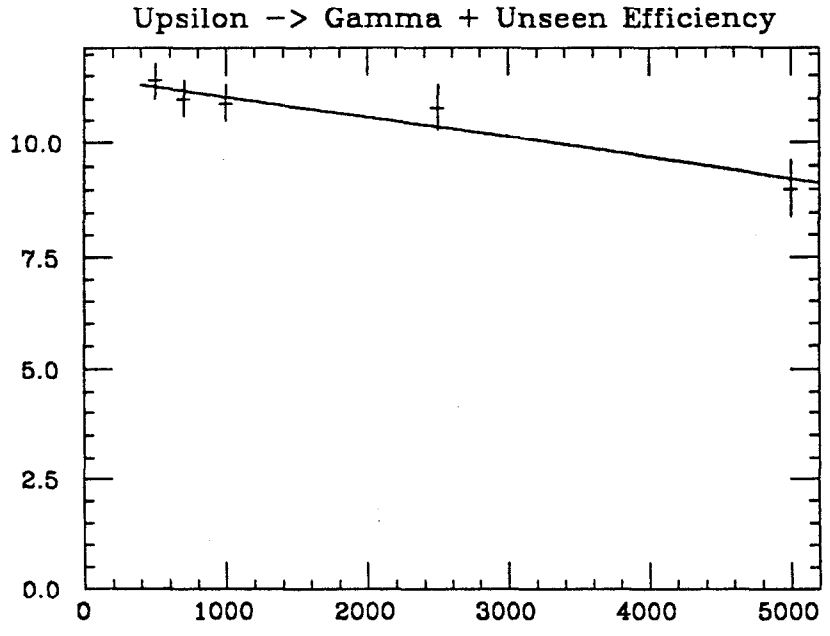

Fig. 5.1 Detector and Analysis Efficiency for the process $\Upsilon' \rightarrow \pi^0\pi^0\Upsilon$, $\Upsilon \rightarrow \gamma +$ Unseen. The linear fit to the five data points is indicated. Efficiency is given in % and the photon energy scale units are MeV. The charged particle cut efficiency has not been included.

is shown in figure 5.6. The missing mass distribution derived from the dipion system energy and momentum is displayed in figure 5.7.

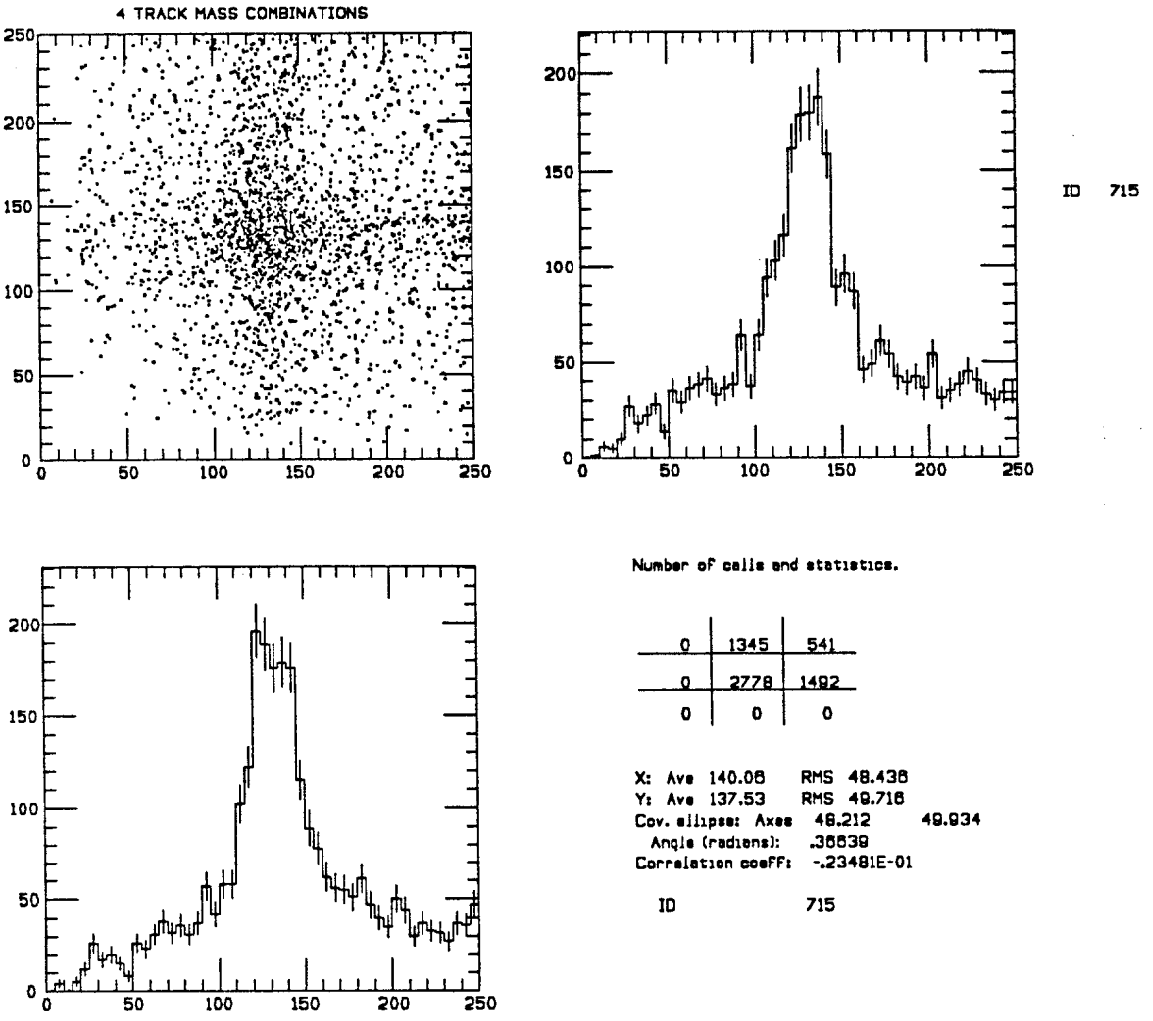

Fig. 5.2 $m_{\gamma\gamma}$ *vs* $m_{\gamma\gamma}$ scatterplot for NTOPO events with ≥ 5 tracks (Final sample after PHYSAC kinematic fitting). $m_{\gamma\gamma}$ projections are shown. A matrix indicates the number of events within the scatterplot as well as the number of events with $m_{\gamma\gamma} > 250$ MeV on the vertical or horizontal axis. Unfitted photon energies and directions are used to form the paired photon masses.

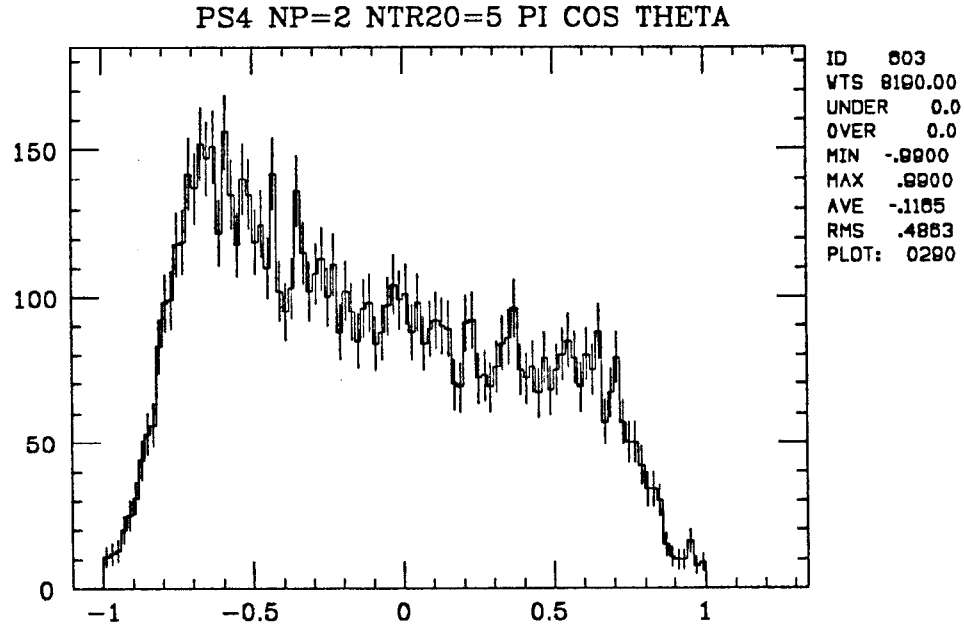

Fig. 5.4 $\cos\theta$ for pions found by PHYSAC. The distribution obtained from the final NTOPO $\Upsilon(2S)$ data sample is histogrammed.

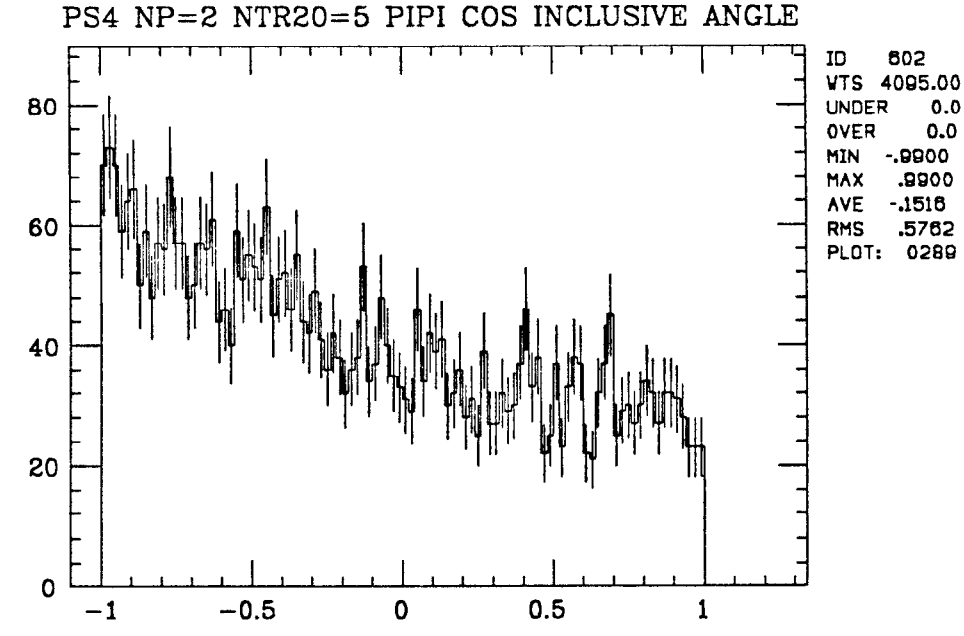

Fig. 5.5 cos $\theta_{\pi\pi}$ distribution for pion pairs found by PHYSAC.

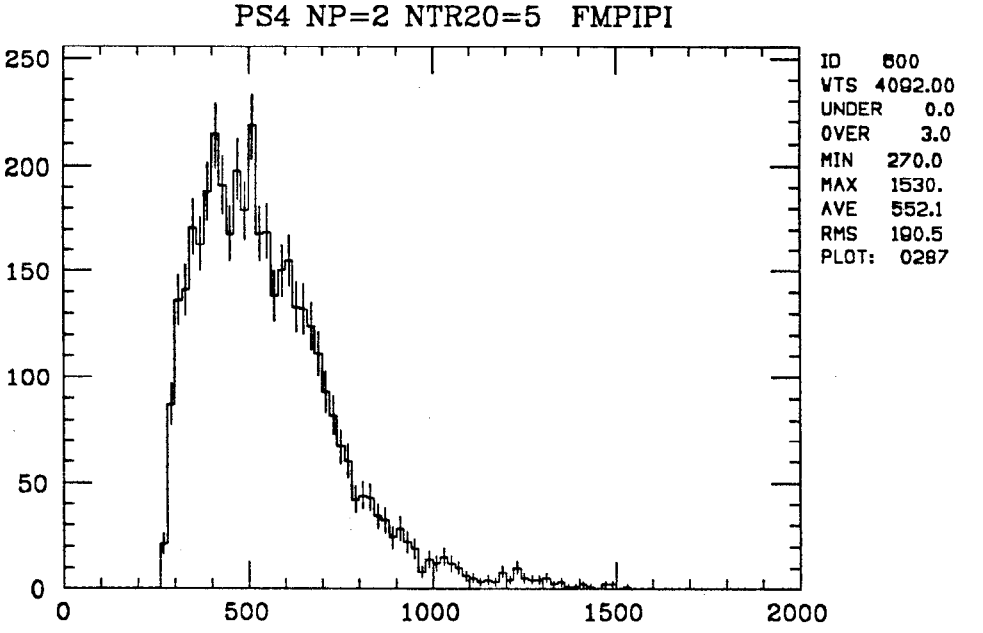

Fig. 5.6 Dipion system mass distribution for NTOPO final sample five track events. Mass is given in MeV/c^2.

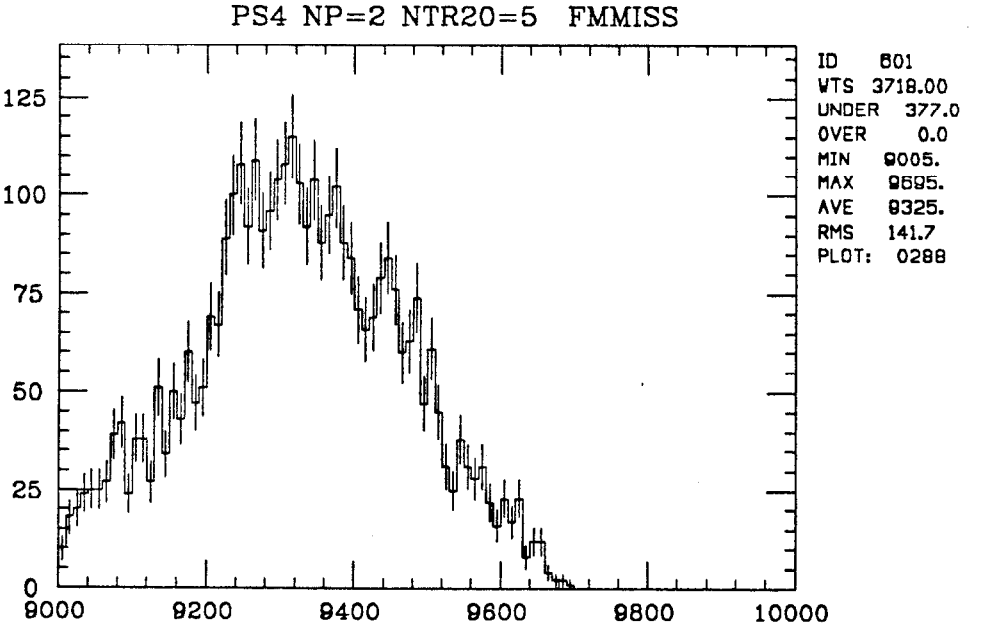

Fig. 5.7 Missing mass distribution for NTOPO final sample five track events. Missing mass is given in MeV/c^2.

5.3.2 *Photon Energy Distributions*

Figure 5.8 illustrates the missing mass formed from the dipion system (four photons) found by PHYSAC plotted versus the energy of the extra photon in the five track event. A band of low energy photons is visible for energies below 500 MeV and a smattering of photons with energies greater than this is distributed over the missing mass range displayed in the plot. The low energy edge of the the background event band is truncated for missing masses above 9300 MeV by the total energy threshold of the NTOPO trigger. The missing mass distribution for photons having more than 500 MeV is shown in figure 5.9. Because it is desired to study only the reaction $\Upsilon' \rightarrow \pi^0\pi^0\Upsilon$, where the Upsilon decays radiatively, a final cut is made on events having missing outside the range 9400-9500:

10) $9400 < M_{miss} < 9500.$ [5.6]

The unpaired photon energy distribution for events passing this cut is shown in figure 5.10.

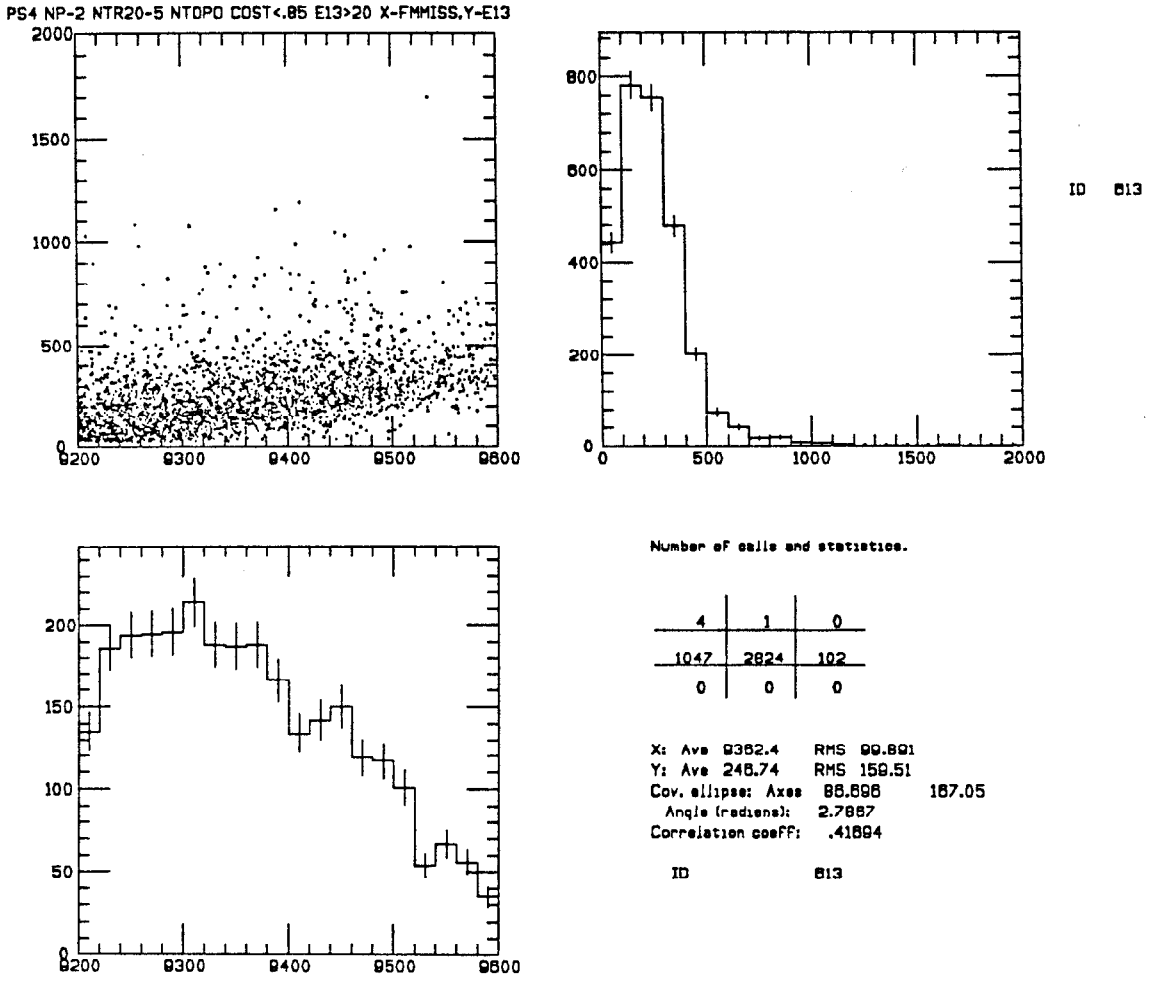

Fig. 5.8 Missing mass versus unpaired photon energy for events passing cuts 7-9. Masses and energies are given in MeV.

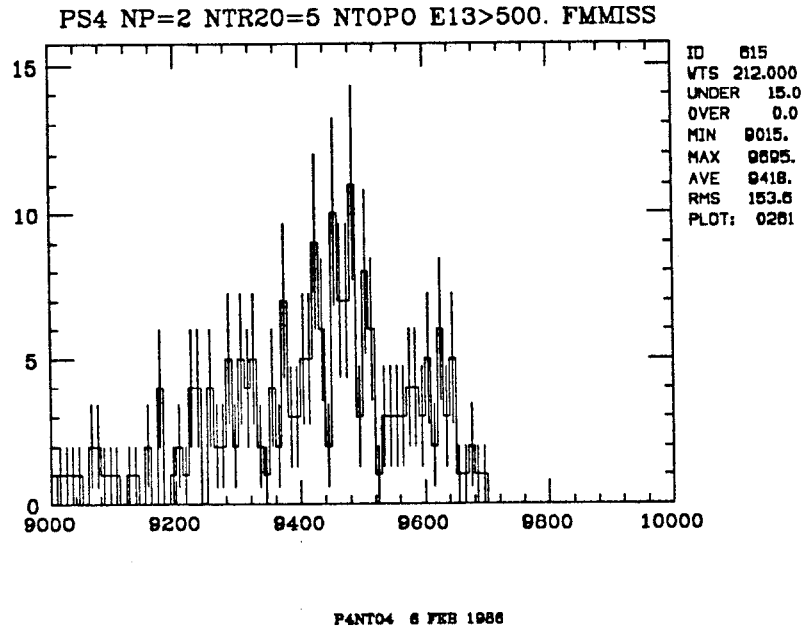

Fig. 5.9 Missing Mass Distribution for $E_\gamma > 500$ MeV events passing cuts 7-9. Missing mass is given in MeV.

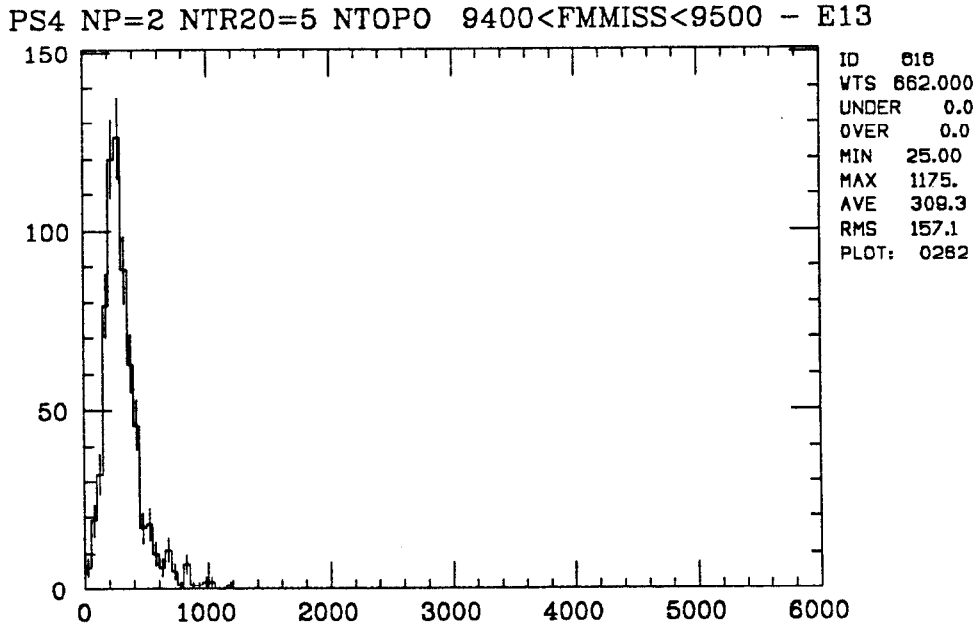

Fig. 5.10 E_γ distribution for events with $9400 < m_{missing} < 9500$. Unpaired photon energy is given in MeV.

5.4 Conclusions

The unpaired photon energy distribution (fig. 5.10) indicates that a large low energy photon background with a peak corresponding to the NTOPO total energy threshold still remains after the missing mass cut (10). No events with a photon energy greater than 1250 MeV are present in this plot. In order to obtain a 90% confidence level upper limit on the number of monochromatic photon + $\pi^0\pi^0$ events seen over this distribution, a 5 term Legendre polynomial background plus a signal gaussian was fit to the events in the expanded scale plot shown in figure 5.11. The width of the gaussian function was based on the width observed in the Monte Carlo datasets and the mean was fixed at 50 MeV intervals from 500 to 1300 MeV. The results of the fit were evaluated by a program which varied the fit parameters in order to map out the likelihood functional dependence on the gaussian amplitude. The likelihood versus amplitude distribution obtained in this manner is then normalized and integrated from amplitude 0 until the integral reaches 90% of the functional normalization value. This result is then considered to be the 90% upper limit for the gaussian amplitude at a given mean. The value 2.3 (Poisson statistics) was taken to be the 90% confidence level upper limit for events with $E_\gamma > 1350.$ MeV.

The number of observable $\Upsilon(1S)\rightarrow\gamma+$ Unseen events was estimated by assuming a 5% error on the 57.4 pb^{-1} of $\Upsilon(2S)$ luminosity, a 2.25% error on the calculated efficiency curve shown in fig. 5.1, and the quoted errors in $BR(\Upsilon'\rightarrow\pi^0\pi^0\Upsilon)$ (eqn. [4.34]) and $\epsilon_{CH}^{5\,Track}$ (eqn. [5.5]). A 90% lower limit based on gaussian errors was calculated for this number and divided into the upper limit for observed events in order to obtain a 90% C.L. Upper limit for $BR(\Upsilon\rightarrow\gamma+$ Unseen). Figure 5.12 illustrates the upper limits obtained by means of this process for the photon energy range 500-5000.

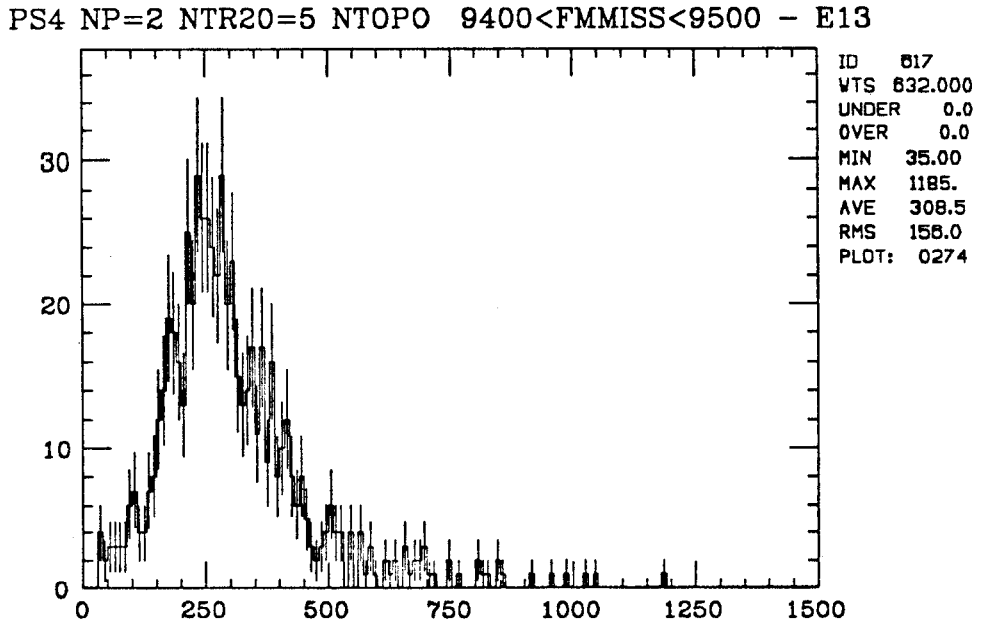

Fig. 5.11 E_γ (0-1500 MeV) distribution for events with $9400 < m_{missing} < 9500$.

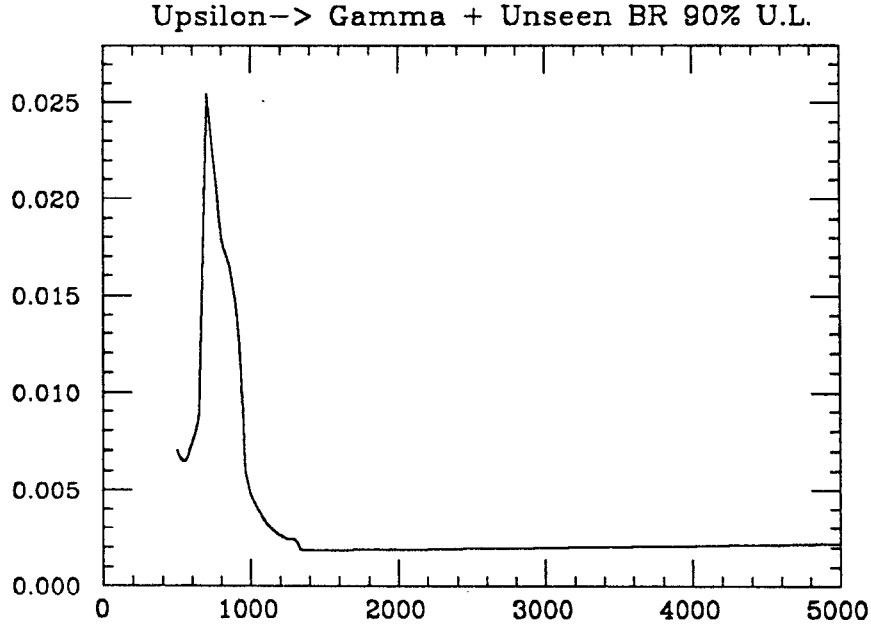

Fig. 5.12 90% C.L. Upper Limit for BR($\Upsilon \rightarrow \gamma$+Unseen) for $500 < E_\gamma < 5000$ MeV The energy range above 4730 MeV is kinematically forbidden for Upsilons created at rest.

Chapter 6

Conclusions

This thesis reports on a search for two possible decay modes of the Upsilon involving the emission of noninteracting particles. This search makes use of the hadronic transition $\Upsilon' \rightarrow \pi^0\pi^0\Upsilon$ to 'tag' the unseen Upsilon. In the first process considered, the Upsilon decays directly into unseen particles. The upper limit

$$BR(\Upsilon \rightarrow Unseen) < 12\% \quad (90\ \%\ \text{C.L.}) \qquad [6.1]$$

was obtained for this reaction. The only previous measurement of this process by the CLEO collaboration yielded an upper limit of 5% (95% C.L.) as measured via transitions from the $\Upsilon(2S)$ and 8% (95% C.L.) from the $\Upsilon(3S)$. The CLEO $\Upsilon(2S)$ measurement suffered from an extremely low detection and analysis efficiency of 0.7 %. The detection and analysis efficiency for the CLEO $\Upsilon(3S)$ measurement is much better (8%) but a combination of a much smaller dipion branching ratio from the $\Upsilon(3S)$ to the Upsilon and a smaller $\Upsilon(3S)$ data set limit the event statistics of this analysis as well.

The second process considered was the radiative decay of the Upsilon into noninteracting particles. The present measurement sets an upper limit on BR($\Upsilon \rightarrow \gamma$+Unseen) over the photon energy range from 500 - $\frac{M_\Upsilon}{2}$. This is the first measurement of this process and is sensitive to photons having energy less

than 1 GeV. For the highest enegy photons having mass $\sim \frac{M_\Upsilon}{2}$,

$$BR(\Upsilon \rightarrow \gamma + Unseen) < 2.3 \times 10^{-3} \ . \qquad [6.2]$$

Although this upper limit is larger than those obtained via higher statistics direct $e^+e^- \rightarrow \Upsilon$ production, the compact geometry of the Crystal Ball detector reduces this disadvantage when the noninteracting particles under consideration are short-lived. As a consequence of this effect, a short-lived 1.6 MeV axion can be excluded based on the present measurement and the assumption of the minimal Peccei-Quinn model.

Appendix A

Trigger System

A.1 Trigger System Overview

A high energy physics experiment is usually not able to record information at the rate that colliding beam processes generate signals in the detector. Storage ring raw signal rates can range from 10 KHz to 1 MHz while the typical experiment can only record information at the rate of 1-10 Hz. Because of this limitation, only selected events can be recorded by the data acquisition system. It is the job of the trigger system to decide which of the raw events will be recorded for further study.

This appendix describes the Crystal Ball trigger system as implemented at DORIS II.* The configuration of this system was a compromise between organizational complexity in the data acquisition electronics and a desire to sample all possibly interesting e^+e^- reactions. The final configuration was designed to ensure a high trigger efficiency for the major channels of interest while providing a reasonable efficiency for the sampling of more speculative channels.

Since the interrogation of the detector electronics following a trigger assertion requires a finite time, during which the detector is unable to take new data, all of these channels need to be sampled without incurring an unduly high trigger

* For a discussion of the corresponding situation at SPEAR, see references 1 and 2.

rate. The Crystal Ball data acquisition system requires 40-50 ms of "dead-time" per event to digitize the raw electronic signals and record this information. If events are triggered at the rate of 3 Hz, approximately 140 milliseconds are lost every second. In this case the detector would be unable to sample 14% of the produced events. A high trigger rate therefore directly translates into a lower total number of colliding beam events available for study.

The primary contribution to the trigger rate is from phenomena not related to e^+e^- collisions. Interactions of either the electron or positron beams with gas molecules within the beampipe account for the majority of these background events. These beam-gas events have an energy distribution which is peaked at low energy values. They tend to deposit energy within a single region in the detector and this region is usually located at small angles to the beam. Since annihilation events tend to distribute energy more isotropically into the apparatus, topology conditions on the deposited energy may be useful in rejecting beam-gas related background processes. The trigger system must therefore attempt to exclude background processes by means of constraints on the energy and topology of accepted events.

Event information is recorded when one or more of the hardware triggers are asserted. These triggers are formed from logical functions implemented in either TTL or NIM logic. The TTL system is housed in custom designed CAMAC modules while the NIM system is a collection of commercially available NIM standard modules. The two systems are nearly independent in operation except that the TTL system always sets the event timing in cases of concurrent TTL and NIM triggers.

Individual triggers are optimized to enable one or more of the desired reaction channels to be sampled. Table A.1presents a list of the triggers used during this study and their corresponding particle physics motivation. The TTL system triggers are listed first and are followed by the NIM system triggers (prefixed by "NIM"). The ETOT triggers have only a total energy requirement that must be

satisfied before they will be asserted. The remaining triggers (excepting the DBM triggers) must fulfill some combination of total energy and topology conditions before being asserted. The topology conditions fall into three classes: hemispherical, back-to-back, and multiplicity. The hemispherical topology triggers are indicated by the word "topo." These triggers require that a hemispherical topology condition be satisfied. The Mu Pair, Bhabha and Quark triggers demand that at least two approximately back-to-back energy depositions be detected. The 3MT and 4MT triggers require a signal in 3 and $\geq$ 4 major triangles, respectively. The NIM NMULT trigger has a similar, $\geq$ 3 major triangle, condition. The DBM triggers are used to sample random beam crossings in order to study beam-related background effects. A description of each trigger's construction will be given following the explanation of the trigger system architecture. Because of the importance of the NIM NMULT and NIM Topo triggers to this thesis work, details of their performance are presented in the final sections.

A.2 Trigger Electronics

Each photomultiplier tube (PMT) produces output pulses having a characteristic NaI scintillator rise-time of 50 ns and fall-time of 250 ns. (The rise time is typical of such large volume crystals.) The area and the amplitude of these pulses are proportional to the energy deposited in the crystal connected to the PMT. A coherent analog summation of the output pulse from each PMT in a minor triangle (group of nine) is constructed and made available to the trigger electronics. Therefore, the minor triangle is the smallest spatial segment of the detector in which deposited energy can be evaluated in trigger decisions. Minor triangle pulses are similarly summed by fours to produce major triangles. Upper and lower hemisphere minor triangles are also combined separately to form top, bottom and full (total) energy sums.

Each of the distinct energy sums (80 minor triangles, 20 major triangles, top and bottom hemispheres, full energy, 8 endcap segments and 2 tunnel regions)

TRIGGER PHYSICS MOTIVATION	
Trigger	Primary Type of Event Sought
Topo 6	Two photon interaction →final state
Topo 20	$\Upsilon'\rightarrow$ hadronic final state
Topo 20V	$\Upsilon'\rightarrow$ hadronic final state
3 MT	backup to NMULT trigger.
4 MT	backup to NMULT trigger.
Mu Pair	e^+e^-, $\Upsilon'\rightarrow \mu\mu$, $\Upsilon'\rightarrow \gamma\gamma\mu\mu$, $\Upsilon'\rightarrow \pi\pi\mu\mu$
Bhabha	$e^+e^-\rightarrow e^+e^-$
Quark	backup to Mu Pair trigger.
ETOT	$\Upsilon'\rightarrow$ hadronic final state, $e^+e^-\rightarrow e^+e^-$
NIM Topo	Two photon interaction →final state $\Upsilon'\rightarrow \pi^0\pi^0\Upsilon$, $\Upsilon\rightarrow \gamma+$ Unseen (This Study)
NIM ETOT	backup to ETOT
NIM DBM	beam related background sampling
NIM DBM2	high energy tail of beam related background
NIM NMULT	$\Upsilon'\rightarrow \pi^0\pi^0\Upsilon$, $\Upsilon\rightarrow$ Unseen (This Study)

Table A.1 Υ(2S) Trigger Physics Motivation.

may cause a dedicated hardware discriminator to fire. This will occur whenever a given energy sum exceeds a preset threshold level. For example, all minor triangle discriminators may be set so that the energy threshold is 90 MeV.* If the

* These thresholds are approximate within 10% or so. This is due to the lack of calibration constants at the hardware level. Discriminator thresholds are checked frequently and photomultiplier gains are reset periodically to correct for systematic drifts of the electronics.

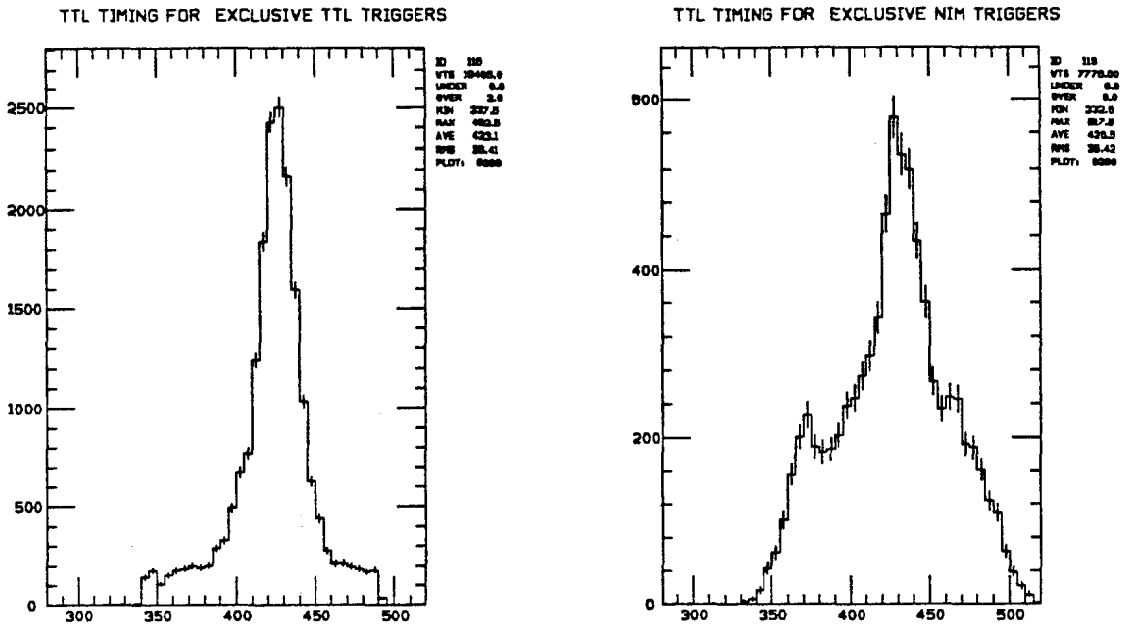

Fig. A.1 Trigger System Timing Distributions.
Figure a shows the timing distribution of events which were triggered only by the TTL Trigger System. Figure b shows the corresponding distribution for events which were triggered only by the NIM Trigger System. Note that the vertical scales are not the same in the two plots.

deposited energy in any minor triangle is higher than this value, the corresponding discriminator will produce a logic pulse which may then cause a trigger to be asserted.

A.2.1 *Event Timing*

The trigger system functions subject to the constraint that an event may only be triggered within a short interval of the time the electron and positron bunches cross in the interaction region. The purpose of this constraint is both to enhance the number of events derived from e^+e^- annihilation relative to those originating in cosmic ray interactions (which are not correlated with the beam timing) and to ensure that the data acquisition system can accurately record the crystal energies. The timing signal used is derived from the DORIS RF cavity

control signal which is synchronized with the experimental timing through a 'black box' supplied by the DORIS machine group. The timing window for the TTL system is 32 ns wide while the NIM system must trigger within a 16 ns window. Figure A.1 displays the timing distributions for exclusive TTL and exclusive NIM system trigger events.

A.3 Trigger Logic

This section describes the logical functions which may be incorporated into the construction of a given trigger.

A.3.1 *Total Energy*

The total energy function is formed by applying a discriminator to the energy sum of the non-tunnel modules within the central detector. Energies measured in the endcaps are not included in this sum. Most triggers are a combination of a total energy threshold and a topology condition. However, this is the only logical function utilized by the NIM and TTL system ETOT triggers.

A.3.2 *Back-To-Back Topology Condition*

Event topology information may be decoded by forming higher order functions from discriminator logic outputs. These logic functions require that certain combinations of discriminators fire in concert. For instance, since muon pairs ($e^+e^- \rightarrow \mu^+\mu^-$) are highly colinear they may be detected by requiring some total energy threshold and the presence of "back-to-back" minor triangles. The back-to-back function demands that at least one minor triangle and the minor triangle located diametrically opposite to it in the detector fire in the same event. The TTL system forms a back-to-back function for both minor and major triangles. The Mu Pair, Bhabha and Quark triggers utilize a back-to-back minor triangle logical function.

A.3.3 *Major Triangle Multiplicity*

Both trigger systems also form a multiplicity function for major triangles. This function counts the number of major triangle discriminators that fire in an event. It is most useful in the search for low multiplicity final state reactions. The NIM NMULT, 3MT and 4MT triggers make use of this topology condition in order to detect the $\Upsilon' \rightarrow \pi^0\pi^0\Upsilon$ hadronic transition when the Υ is unseen. The low energy pions predominantly decay into two photons which often deposit energy in separate major triangles.

A.3.4 *Hemispherical Topology*

Another type of function demands a loose energy balance in the detector. Energy balance is achieved by dividing the detector into many rough, overlapping hemispheres composed of major triangles and demanding that the event deposit energy in each of these. As an example, a four hemisphere function could be defined such that energy must be deposited in both the top and bottom halves as well as in the left and right sides of the detector during an event. The TTL system forms two hemispherical topology functions based on divisions into 6 and into 20 hemispheres which are used by the Topo 6, Topo 20, and Topo 20V (tunnel module "Veto'ed") triggers. The two functions require a minimum of one major triangle discriminator to fire in each of the six or twenty hemispheres respectively. The NIM Topo trigger employs a topology function based on a two hemisphere division of the central detector.

A.3.5 *Tunnel Veto*

One method of suppressing beam gas events makes use of the fact that they predominately deposit energy at small angles to the beam direction. Since the "tunnel" region (see chapter 2) consists of the main ball NaI modules that border the beam pipe, large energy depositions in these modules arise primarily from beam gas interactions. Accordingly, a discriminator is used to generate a trigger

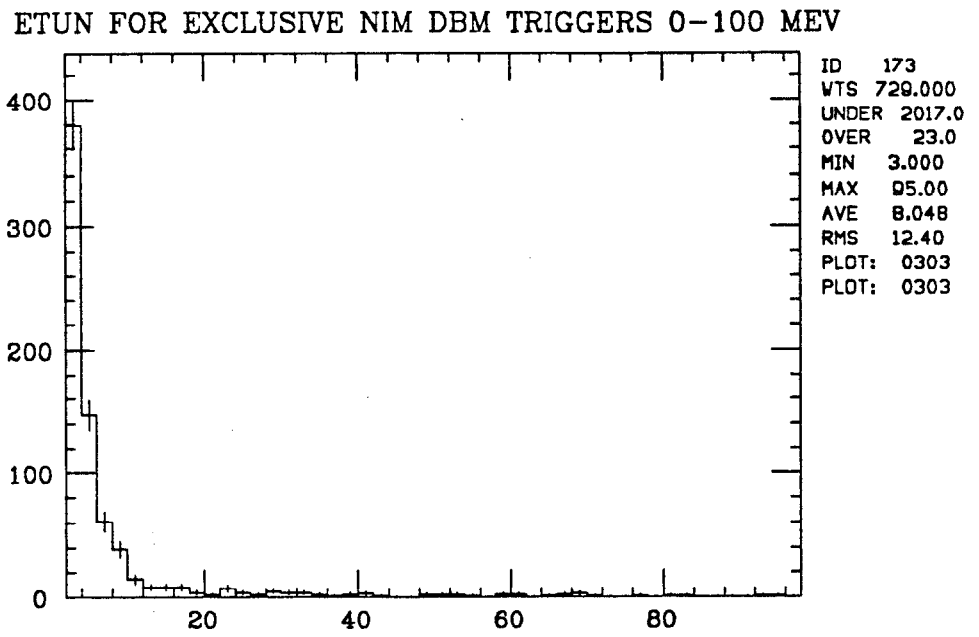

Fig. A.2 Tunnel Region Energy Distribution.
Energy distribution sum for tunnel region modules during random beam crossings.

veto signal whenever the tunnel region energy sum exceeds some threshold value. Since the tunnel region subtends a small solid angle, beam gas events will be rejected preferentially (compared to annihilation events) as long as the tunnel veto threshold value is set above the ambient level of energy deposited within this region (see Figure A.2).

It should be noted that this veto condition was not needed at SPEAR. The DORIS II environment has higher backgrounds than those experienced at the lower energy machine. This is likely due to the closer proximity of the mini-β quadrupole magnets at DORIS, coupled with the higher beam currents ($\sim$ 50 mA per beam) commonly used.

A.4 Trigger Architecture

A trigger is constructed by combining logical functions in such a way as to attempt to maximize the trigger efficiency for a desired event topology while

minimizing the acceptance for unwanted topologies. Table A.2 furnishes the logical functions and discriminator threshold values utilized by the various Crystal Ball triggers during the course of this study. Because of their importance to the detection of the processes studied in this thesis, the performance of the NIM NMULT and NIM Topo triggers is discussed. Similarly, the DBM triggers were useful in characterizing the beam-related background encountered at the DORIS II storage ring and modeling that background during data analysis. Their operation and utility are therefore discussed. A schematic outline of the NIM trigger system in fig. A.3 illustrates the logic employed in its construction.

A.4.1 *NIM NMULT Trigger*

The NIM NMULT trigger was designed to sample the process

$$\Upsilon' \rightarrow \pi^0\pi^0\Upsilon$$
$$\qquad\qquad\quad \Big\downarrow$$
$$\qquad\qquad\quad \textit{Unseen}$$

by detecting the photons emitted via the reaction $\pi^0 \rightarrow \gamma\gamma$. The total energy available for this process is

$$\Delta M = M_{\Upsilon'} - M_{\Upsilon} \sim 560\ MeV.$$

The trigger combines the following conditions:

- $500 \leq E_{Tot} \leq 700\ MeV.$
- $E_{Major\ Triangle} > 95\ MeV$
- $E_{Tunnel\ Region} < 35\ MeV$

The total energy and major triangle thresholds were set as low as practical giving an exclusive rate for this trigger which varied from .5 to 1.0 Hz depending on running conditions. Figure A.4 shows the efficiency of the NMULT trigger versus total energy for the data used in this analysis.

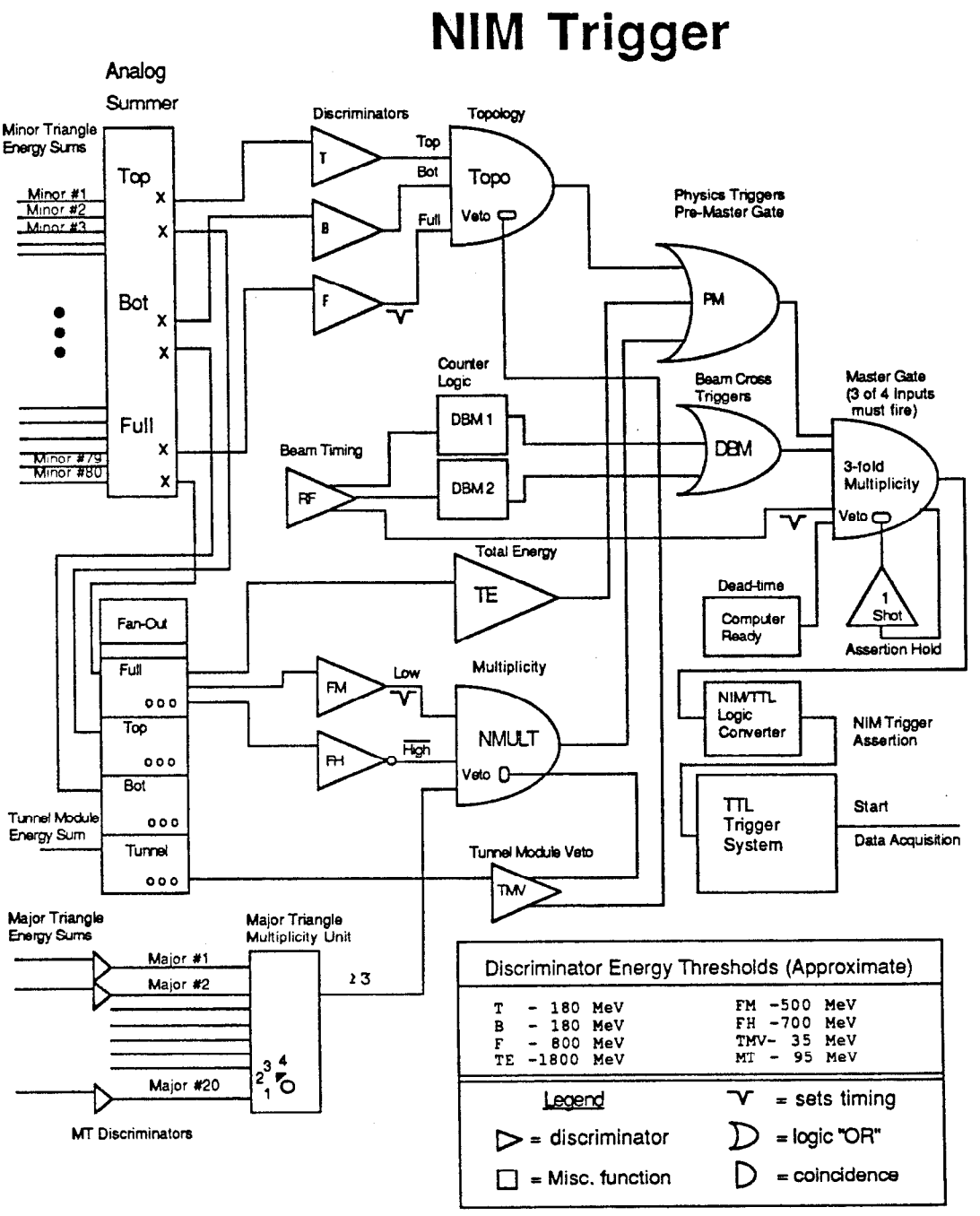

Fig. A.3 NIM Trigger System Logic. Analog fan/outs and fan/ins produce energy sums which are compared to set thresholds by discriminators. The discriminator logic-level outputs are combined to form triggers. The 1-shot veto in the master logic gate is designed to prevent multiple trigger assertions from occurring.

TRIGGER CONDITIONS					
Trigger	E_{tot} MeV	Major Triangle # (MeV)	Minor Triangle # (MeV)	Hemispheres # (MeV)	Tunnel Veto
Topo 6	980	≥2(150)	—	6(150)	—
Topo 20	770	≥2(150)	—	20(150)	—
Topo 20V	—	≥2(150)	—	20(150)	yes
3 MT	450	3(95)	—	—	yes
4 MT	450	≥4(95)	—	—	yes
Mu Pair	220	—	≥ 2(85)[a]	—	yes
Bhabha	5900	—	—	—	—
Quark	220	—	≥ 2(85)[a]	—	yes
ETOT	1760	—	—	—	—
NIM Topo	800	—	—	2(180)	yes
NIM ETOT	1740	—	—	—	—
NIM DBM[b]	—	—	—	—	—
NIM DBM2[c]	150	—	—	—	—
NIM NMULT	500[d]	≥3(95)	—	—	yes

Table A.2 Υ(2S) Trigger Conditions. Discriminator thresholds are given in MeV.[e]

(*a*) Minor triangles must be nearly back-to-back for the Mu Pair Trigger and exactly back-to-back for the Quark Trigger.

(*b*) Fires once every 10^7 beam crossings (~ once per 10 sec).

(*c*) Enabled once every 10 seconds (real time).

(*d*) NMULT employed a total energy window of $500 < E_{tot} < 700\ MeV$.

(*e*) Trigger thresholds are approximate within 10% due to drifts in phototube gains and electronics.

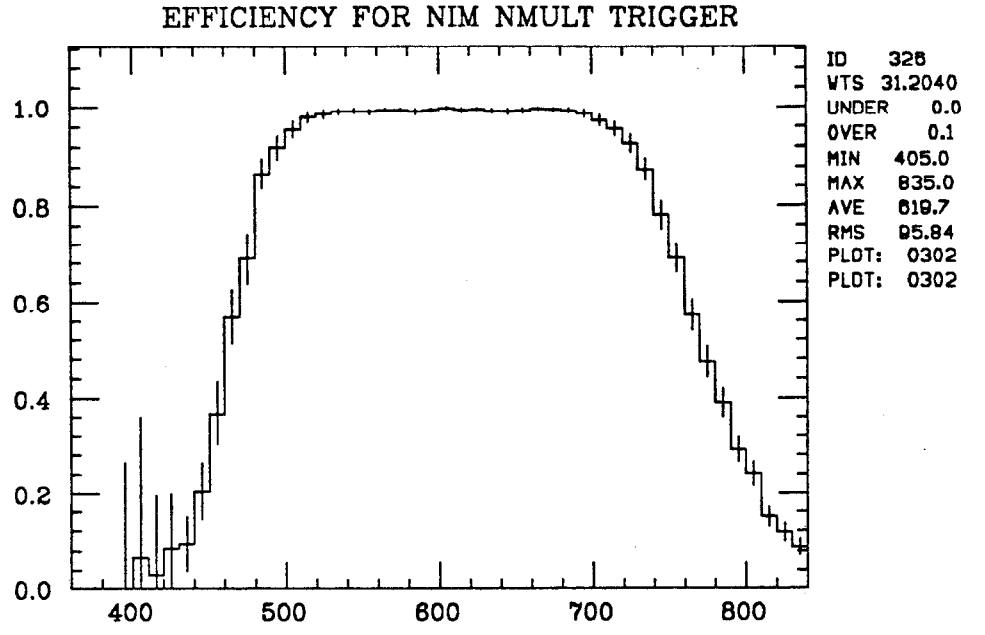

Fig. A.4 NIM NMULT Trigger efficiency versus total energy. The energy is given in MeV.

A.4.2 *NIM Topo Trigger*

The NIM Topo trigger is used to sample the process

$$\Upsilon \rightarrow \pi^0\pi^0\Upsilon$$
$$\qquad\qquad\quad \lfloor\!\!\longrightarrow \gamma + Unseen\ .$$

The trigger requirements are as follows:

- $E_{Tot} \geq 800\ MeV.$
- $E_{Top,Bottom\ Hemisphere} > 180\ MeV$
- $E_{Tunnel\ Region} < 35\ MeV$

Because of the high total energy threshold, this trigger is inefficient for the detection of $\Upsilon \rightarrow$Unseen. However, the two hemisphere topology condition is less restrictive than the NMULT major triangle multiplicity condition. Therefore,

the trigger is efficient in detecting $\pi^0\pi^0$ hadronic transitions when the Upsilon decay particles contribute to the total energy as in the case of $\Upsilon \rightarrow \gamma + Unseen$.

A.4.3 *Random Beam-crossing Triggers*

Two special triggers were installed to sample the background of detected energy due to interactions of the beam with gas molecules in the interaction region or with the beampipe structure itself. The result of these interactions is that a "halo" of low energy particles is added to every detected event. These particles may contribute on the order of 50 MeV to the energy deposited in the detector by any e^+e^- event.

The analysis of a given final state reaction requires that a Monte Carlo simulation be performed in order to understand the corresponding detection and analysis chain efficiencies. Typically, Monte Carlo event generators model the fundamental electron-positron reactions without taking into account beam-related backgrounds. In this regard, Monte Carlo events are too "clean" since they lack the "halo" of energy found in real events. The DBM trigger provides a solution to this problem by collecting, in effect, a sampling of these energy "halos" which may be used in conjunction with Monte Carlo events to conduct the necessary efficiency studies. It collects this data set by firing once every 10^7 beam crossings regardless of deposited energy in the detector. Figure A.5 (a) is the background deposited energy spectrum sampled by this trigger.

The DBM2 trigger functions much like the DBM trigger except that a minimum total energy threshold must be exceeded to acquire an event. Therefore, this trigger samples only the high energy tail of the beam-related energy background as seen in figure A.5 (b). These events are most useful in evaluating the effect of beam-related background on trigger firing rates. While events sampled by the DBM trigger could in theory allow one to determine at what rate a hypothetical trigger would fire, a million DBM events would be needed to evaluate how often it fired during the first second alone. This is due to the fact that

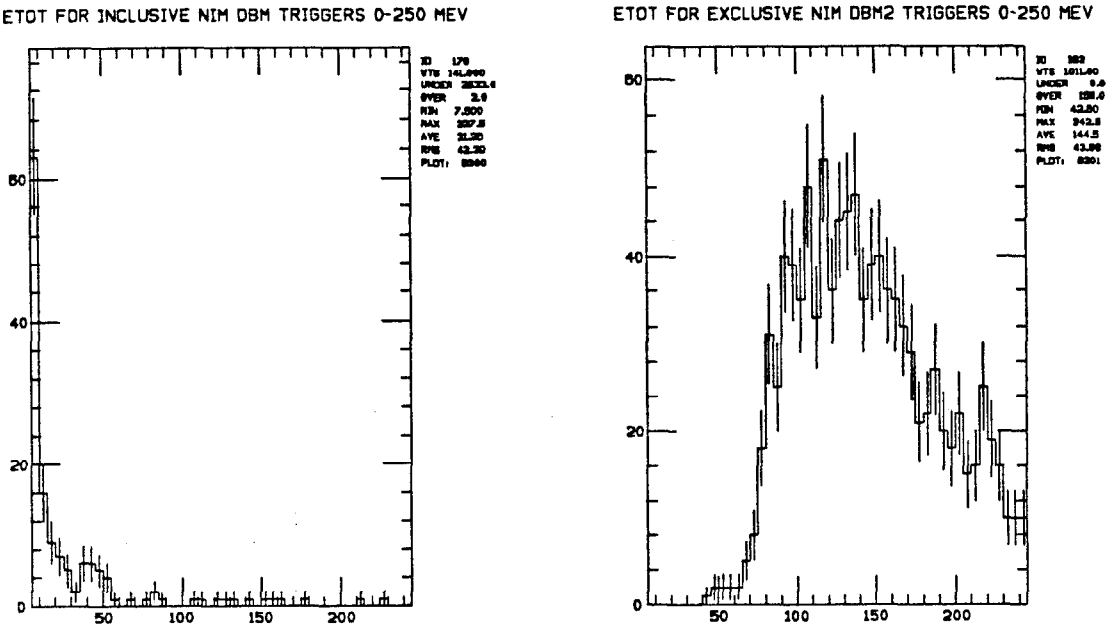

Fig. A.5 Background Energy Distribution.
Figure a shows the visible energy in the detector as sampled by the DBM trigger during random beam crossings. Figure b shows the corresponding distribution as sampled by the DBM2 trigger. Note that the high energy tail is enhanced.

there are a million bunch crossings per second at DORIS II all of which need to be considered by the trigger simulation. The DBM2 trigger remedies this situation by discarding the highly peaked low energy part of the background energy distribution (see Figure A.5 (a)) while retaining the higher energy events which have some chance of causing a trigger to fire. A relatively small sample of DBM2 events is therefore sufficient to realistically model a hypothetical trigger's response to background energy deposition.

References

1) M. Oreglia, Ph.D. Thesis, "A Study of the Reactions $\psi' \rightarrow \gamma\gamma\psi$," Stanford U., 1980. SLAC Report-236. Unpublished.

2) J. Gaiser, Ph.D. Thesis, "Charmonium Spectroscopy from Radiative Decays of the J/ψ and ψ'," Stanford U.,1982. SLAC Report-255. Unpublished.

Appendix B

Monte Carlo

The ability to model particle production processes and to simulate the response of a given detector to the final state particles is a necessary aspect of high energy physics data analysis. Monte Carlo simulations provide information used to separate desired events from background processes and to estimate the efficiency of the various analysis steps. In this study, the Crystal Ball is simulated by means of a geometry program and a material response program which interact to calculate the energy deposited in each part of the detector due to incident particles. The first part of this appendix briefly describes the general structure and operation of the Crystal Ball Monte Carlo program. The final section will discuss the program used to simulate the trigger system.

B.1 Organization

Figure B.1 schematically illustrates the data flow in the Crystal Ball Monte Carlo. The event generation and detector simulation process is divided into two sections referred to as STEP1 and STEP2. The first of these programs is used to generate particle 4-vectors according to selected production models. Many models have been developed for general use. For example models exist to generate events based on phase space decays of various particles such as D and F mesons. There are also models which treat two photon physics, QED and quark fragmentation processes. Although energy deposition within the detector

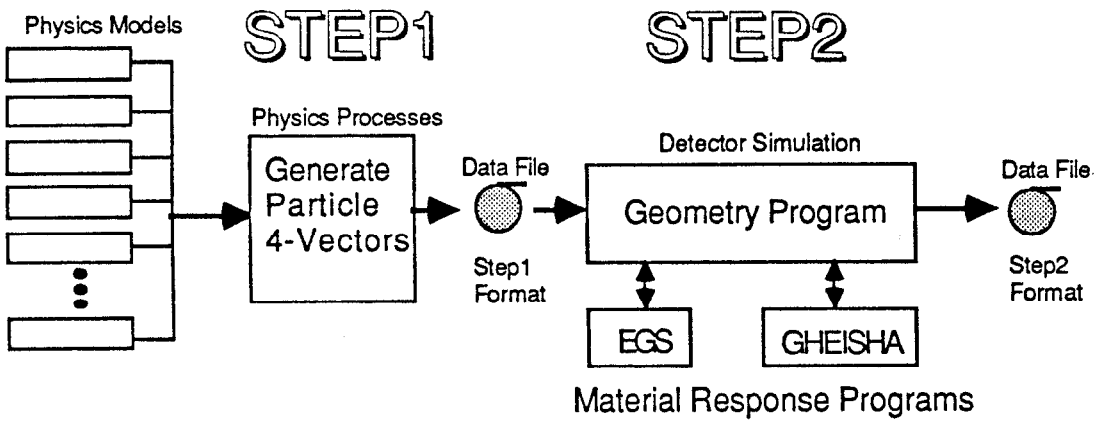

Fig. B.1 Data Flow in the Crystal Ball Monte Carlo.

is not considered at this stage, photons may be converted to e^+e^- pairs in the beampipe or tube chamber material in STEP1. A file containing Monte Carlo event 4-vectors is written either to disk or tape at this point. The STEP2 program then reads these 4-vectors as an input file and calculates the energy deposited in the detector for each event.

B.2 Detector Simulation

The deposited energy is calculated by two interacting programs. A geometry program first identifies the location of each STEP1 particle within the detector. If a particle has not yet reached the central detector or endcaps it is propagated until it does. The appropriate material response program then calculates the energy deposited in the detector element containing the particle and the distance the particle will travel before its next interaction. If a showering process occurs, secondary particles are created which are, in turn, treated in the same manner as the initial STEP1 particles. As long as a given particle retains kinetic energy, it is propagated by the geometry program which then invokes the material response

program. This process continues until the particle either deposits all of its energy or exits the detector.

The detector is subdivided into 800 regions for the calculation of energy deposition. These regions may represent energy sensitive structures such as individual crystals, nonsensitive metallic structures such as the hemispherical shells or volumes of space used as a book-keeping system for keeping track of a particle's approximate location while the geometry program determines its trajectory into an other region.

Table B.1 summarizes the regions used by the geometry program and their material composition. Four different media are assumed to account for all matter (or lack thereof) in the detector simulation. These media are vacuum, sodium iodide, stainless-steel and aluminum. Interactions between particles and these media are handled by the EGS[1] and GHEISHA[2] programs. The first of these programs simulates interactions between electromagnetically showering particles such as electrons and photons and matter. The program has been modified to handle muons by means of a special shower function which approximately emulates the energy deposition of these minimum ionizing particles. The GHEISHA program treats hadronically interacting particles such as charged pions or kaons.

The Monte Carlo results presented in this thesis do not involve hadronically interacting final state particles and therefore the GHEISHA program has not been used. A detailed comparison of the energy and angular resolution of the EGS program, which was used in this work, to Crystal Ball data is found in ref. 3.

B.2.1 *DORIS II Endcaps*

The solid angle subtended by the Crystal Ball is the primary factor in determining the number of Upsilon decays into lepton pairs which will be undetected and thus contribute to the $\Upsilon \rightarrow$Unseen signal studied in this thesis. Because the Monte Carlo must accurately reflect the structure of the detector in order to

Region	Description	Medium	Minimum Dimension
1 - 720	NaI Modules	NaI	2 inches
720-791	NaI Endcap Modules	NaI	5 inches
792	Endcap Block	vacuum	2 feet
793	Endcap module sheathing	SS	20 mil
794	not used	—	—
795	Module 1-720 mylar wrapping	Al	10 mil
796	not used	—	—
797	Equator Washer	SS	$\frac{1}{16}$ inch
798	Outer Shell	Al	$\frac{7}{8}$ inch
799	Inner Shell Dome	SS	$\frac{1}{16}$ inch
800	Unidentified location	vacuum	—

Table B.1 Detector Regions in the Monte Carlo.

model the solid angle acceptance, the geometry program had to be modified to account for the changes in the endcap array described in chapter 2.

Figure B.2 illustrates the horizontal and vertical endcap stacking schemes. Each endcap array ($\pm z$) contains 20 NaI Modules. The horizontal stacks ($\pm y$) each consist of six crystals and the vertical stacks ($\pm x$) are composed of four. The horizontal stacks incorporate 5 long (20 in) and 1 short (10 in) hexagonal crystals. The vertical stacks have two short and two long crystals.

The new endcap algorithm functions by storing the coordinates of the centroid of the two hexagonal faces of each endcap crystal. This defines a symmetry axis for each crystal. Since the hexagonal faces of each crystal are of equal dimension, geometrical planes congruent with the outer faces of each hexagonal module may be defined. The distance of a particle to each of these faces may then be

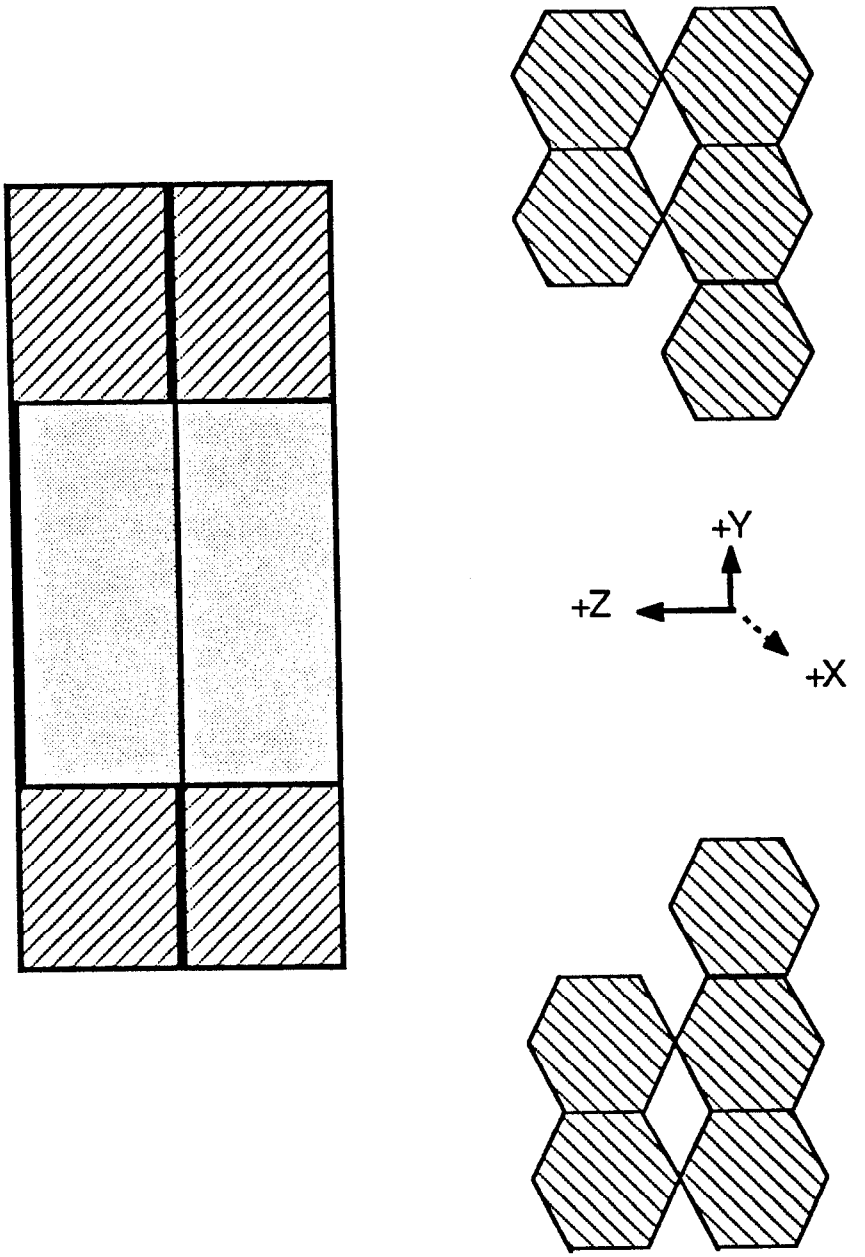

Fig. B.2 Orthogonal side view of +Z endcap stacking scheme. The endcap array is viewed from a point inside the DORIS II ring. The horizontal stacks are seen end on. The far vertical stack is obscured by the near stack (left side of diagram). All crystals have hexagonal end-faces with 2. inch edges and are hermetically sealed in a 20 mil thick stainless-steel sheath.

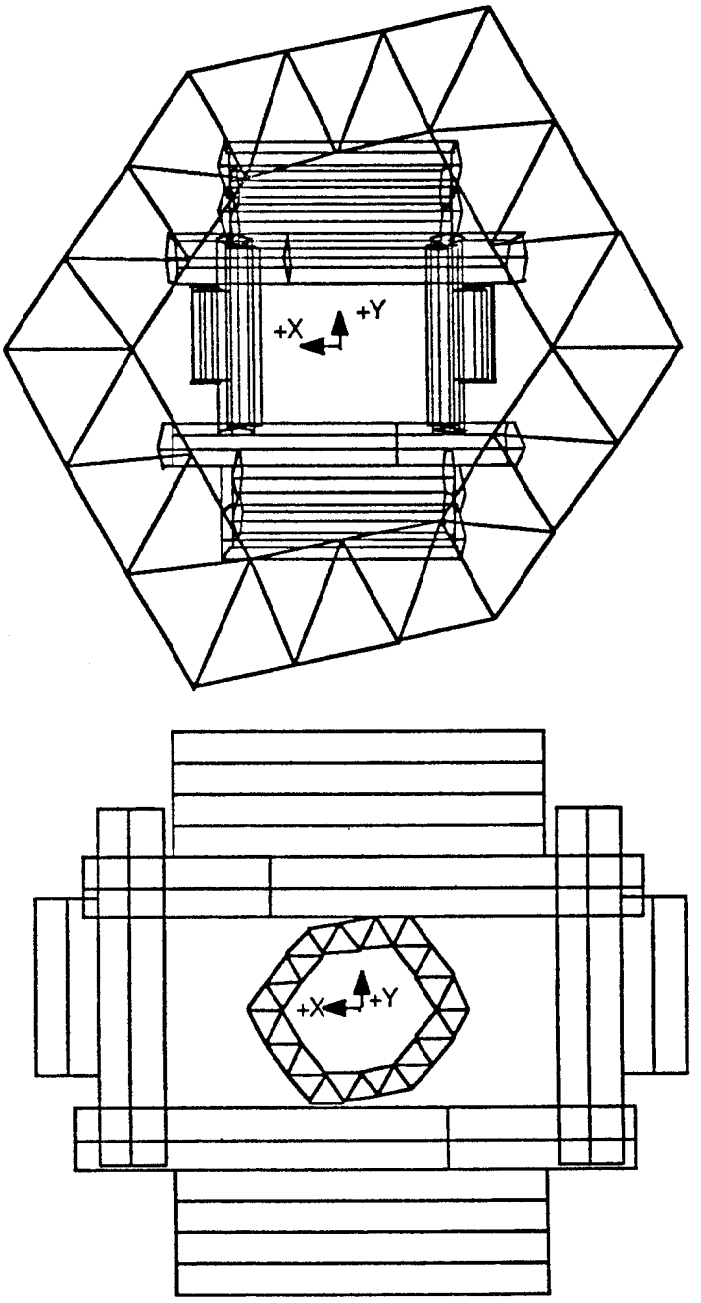

Fig. B.3 Projective (top) and orthogonal (bottom) view of the +Z endcap array as seen from a particle emanating from the interaction point. The tunnel region crystals bordering the beampipe are also shown. Although the tunnel region has a smaller vertical and horizontal extent than the endcaps, it is considerably nearer to the interaction region and so subtends a greater solid angle as seen in the top figure.

computed and used to identify the nearest crystal to that particle. Its associated 4-vector may then be used to compute an impact parameter for the particle's trajectory with respect to the nearest crystal's symmetry axis. Figure B.3 shows the +Z endcap array as seen from the e^+e^- interaction point based on the crystal coordinates used in the Monte Carlo endcap geometry program.

B.3 Trigger Simulation

The Crystal Ball Trigger system is described in Appendix A. Because it determines which events are recorded for analysis by the data acquisition system, its operation must be simulated in software in order to determine the detection efficiency for a given final particle state based on Monte Carlo events.

The simulation program emulates the analog energy sums utilized in the hardware trigger by adding the appropriate (calibrated) crystal energies together in software. Hardware discriminators are imitated by means of measured discriminator efficiency curves. The appropriate software energy sum is then used to determine the probability that a given discriminator will fire based on the corresponding efficiency curve. The simulated discriminator then fires if this probability exceeds a generated random number.

The appropriate logic for each trigger can then be constructed by combining these simulated discriminators. The result of trigger simulation is stored in the same format for each Monte Carlo event as the hardware trigger information is stored for data. The same programs may then be used to select Monte Carlo or real data events based on which triggers were asserted.

Hardware efficiency curves are determined by histogramming the fraction of times a given discriminator fires within a given range of the appropriate energy sum. This is a straightforward procedure for discriminators which set a latch bit when they fire. Figure B.4 presents the efficiency curve measured in this way for the (latched) tunnel module veto discriminator used in the NMULT and NTOPO

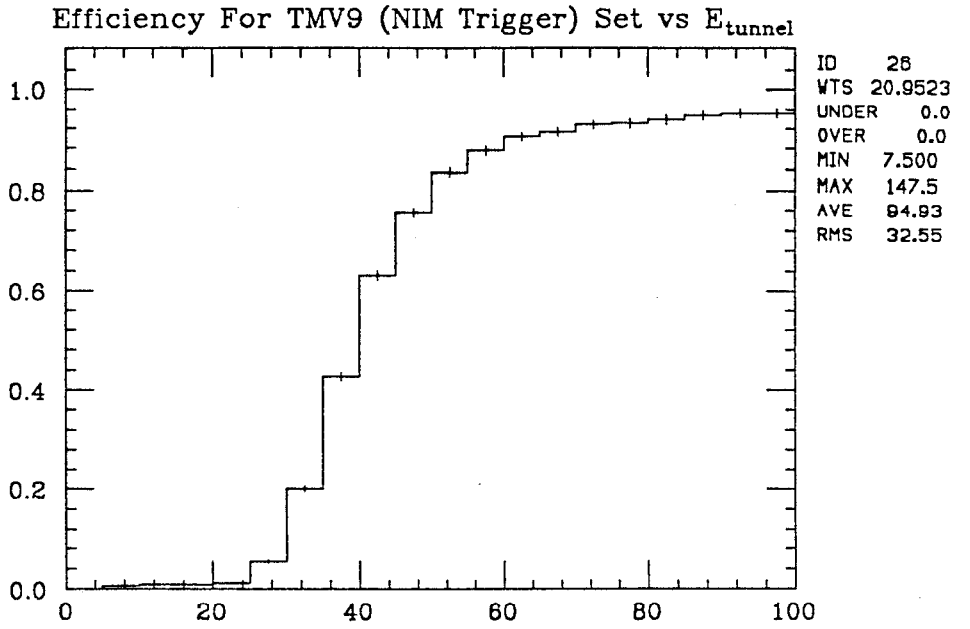

Fig. B.4 NIM Tunnel Module Veto discriminator efficiency curve. The latch bit set when the discriminator fires is used to plot the fraction of times the discriminator fires per tunnel region energy bin (sum of energies in both tunnel regions). A 5% inefficiency is seen for energies well above the discriminator threshold of 30-40 MeV. This inefficiency is attributable to the high firing rate for this discriminator.

triggers. This particular curve is atypical in that a finite (*O(5%)*) inefficiency remains at (tunnel) energies much greater than the discriminator threshold. This effect is due to dead-time associated with the very low energy threshold and hence the high rate at which this discriminator fires ($\sim$ 50 kHz). It implies that the triggers incorporating this veto signal will accept slightly more events than if the discriminator was fully efficient.

Efficiency curves are also needed for the other discriminators used in the NMULT and NTOPO triggers. As seen in figure A.3 in appendix A, the NMULT trigger utilizes 2 total energy discriminators, a tunnel module energy discriminator and 20 major triangle energy discriminators. The NTOPO trigger incorporates 2 hemisphere energy discriminators, the tunnel module energy and a total

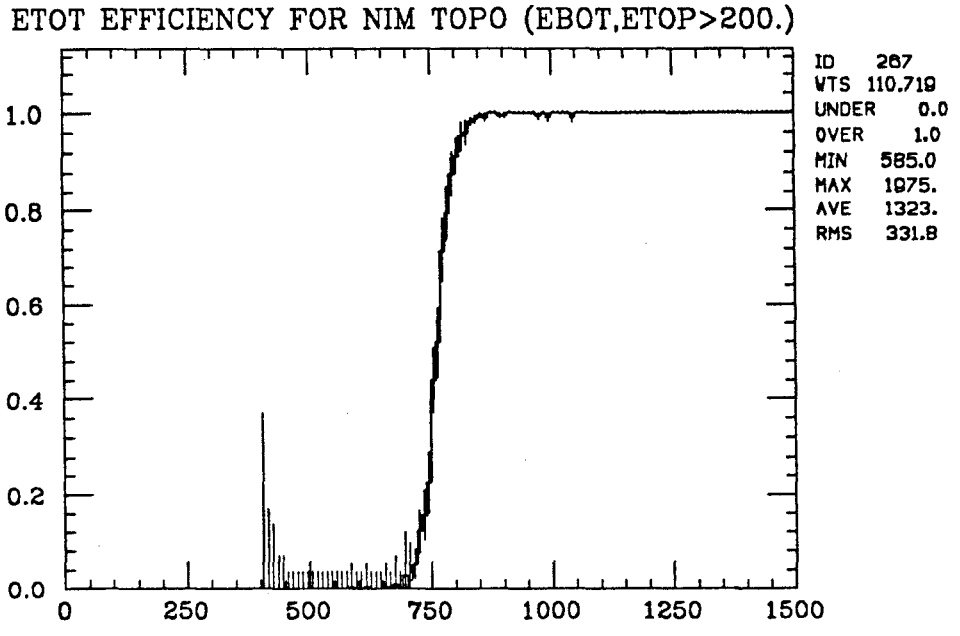

Fig. B.5 NTOPO total energy discriminator efficiency curve. This curve is derived from events in which all of the other NTOPO trigger conditions were satisfied. (The total energy condition was not considered in selecting these events.)

energy discriminator. With the exception of the NMULT total energy discriminators, one of the NMULT major triangle discriminators and the tunnel module veto discriminator mentioned above, none of these discriminators set a latch bit which may be directly used to determine their efficiency curves.

Efficiency curves for unlatched discriminators in a given trigger are measured by selecting events from data in which it is required that all the other trigger discriminator or logic conditions are satisfied. It may then be assumed that the operation of the trigger is dependent on whether the remaining discriminator fired or not. Figure B.5 illustrates the total energy discriminator (unlatched) efficiency curve for the NTOPO trigger which is derived from events in which the NTOPO top and bottom hemisphere energy sums exceeded the required discriminator thresholds by a safe margin and the tunnel module veto discriminator did not fire.

Because of the large number of discriminators used in the NMULT trigger and the added complexity of the multiplicity unit which insures that at least 3 of the 20 major triangle discriminators have fired, it is somewhat more difficult but still possible, to measure the requisite discriminator efficiency curves for this trigger. The total energy window discriminators are both latched and their efficiency is determined directly for the purpose of Monte Carlo simulation. In spite of this, the full energy efficiency for the trigger may be derived in the same manner as was used for the NTOPO trigger in order to verify the overall operation of the major triangle discriminators. Figure B.6 presents the NMULT total energy efficiency as a function of 4 software thresholds (at 90, 95, 100, and 105 MeV) imposed on the major triangle energies. This figure indicates that the trigger operates fully efficiently within the total energy window for major triangle thresholds above 95 MeV (per major triangle) and conversely that the major triangle discriminators are very nearly fully efficient at 95 MeV.

In order to derive the discriminator curve for each major triangle discriminator, events must be selected in which a given major triangle discriminator determines whether the NMULT trigger fired or not. This situation pertains if the major triangle is the third highest energy major triangle, assuming that the first and second highest energy major triangle discriminators have fired and all the other NMULT trigger conditions are satisfied. If a safe, software energy threshold (110 MeV) is applied to the two highest energy major triangles and the other NMULT conditions are satisfied, the operation of the third highest energy major triangle discriminator will determine if the three-fold multiplictiy condition is satisfied and hence the assertion of the NMULT trigger. Figure B.7 shows the resulting discriminator curves based on this method for major triangles 1-4. Because it was feasible to latch one of the major triangle triangle discriminators, a direct comparison may be made between the derived and the measured discriminator efficiency curves for major triangle #7. Figure B.8 presents this comparison. The derived curve for this major triangle agrees quite well with the

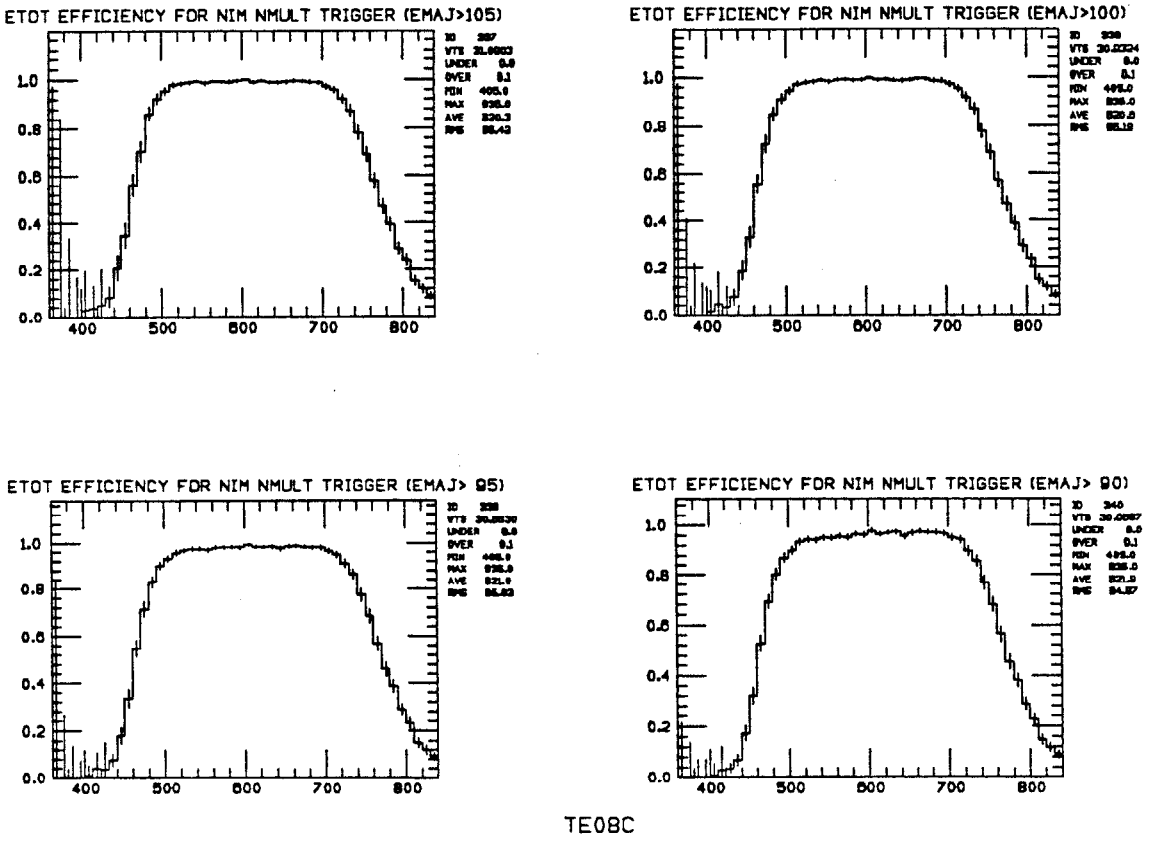

Fig. B.6 NMULT total energy efficiency derived from software major triangle energy thresholds. Four major triangle energy thresholds set at 90, 95, 100 and 105 MeV were used. The resulting total energy efficiency for the NMULT trigger is indicated for each threshold. This efficiency is very nearly 100% for major triangle thresholds $\geq$ 95 MeV. The total energy scale is given in MeV.

measured efficiency. All twenty major triangle discriminator curves derived in this way are modeled in the Monte Carlo trigger simulation.

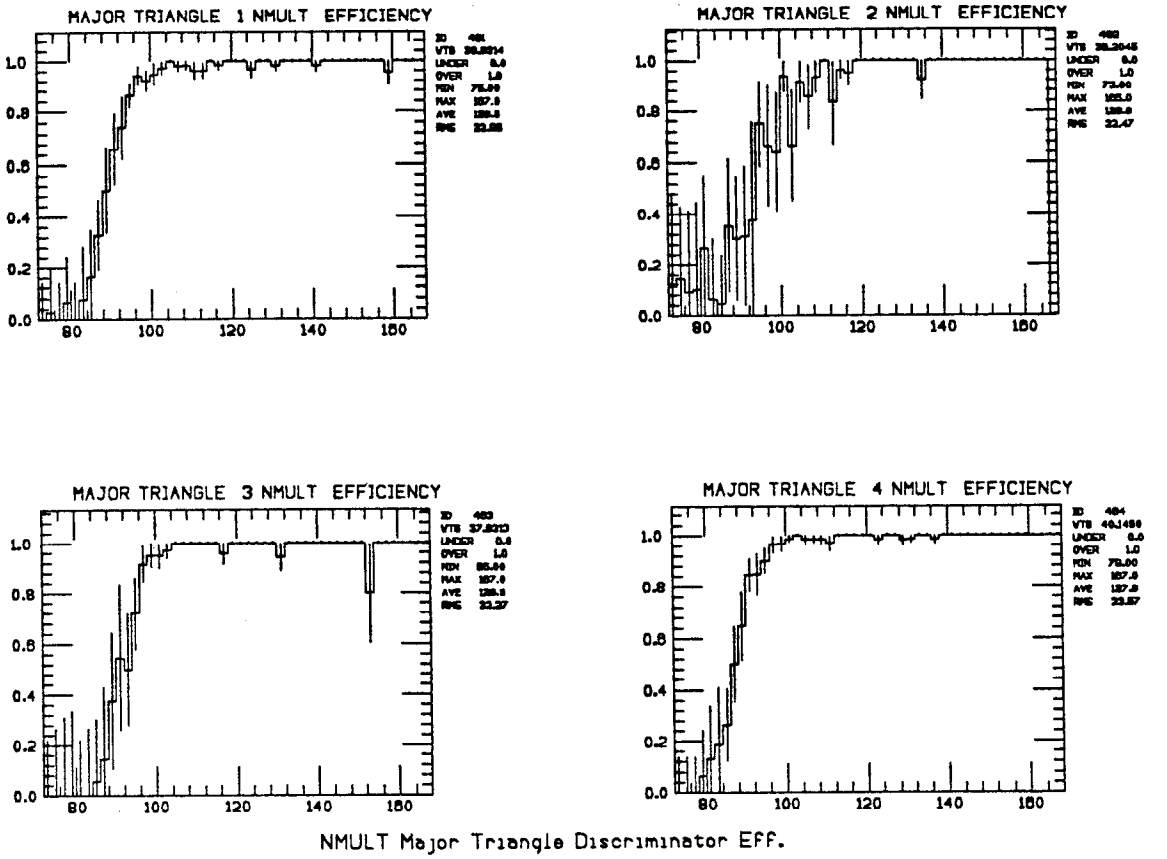

Fig. B.7 NMULT trigger major triangle 1-4 discriminator efficiency curves. These curves are derived for the third highest energy major triangle in an event when the two highest energy majors contain $\geq$ 110 MeV and all other NMULT trigger conditions are met. Similar curves are obtained for the remaining 16 majors. Majors #2 and #3 each border the +Z tunnel region and therefore contribute only three minor triangles (9 NaI modules) to the various trigger energy sums. This reduces the statistics available for analysis of their discriminator curves. Major triangle energies are in MeV.

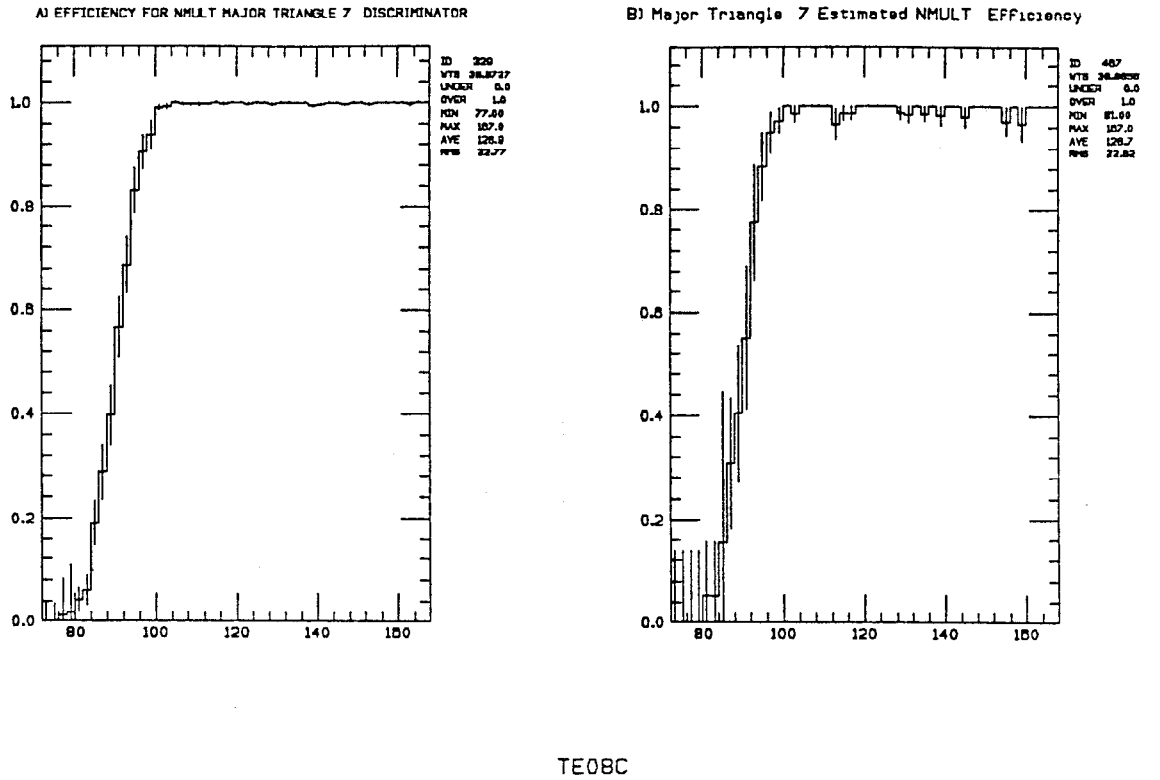

Fig. B.8 Measured (A) and derived (B) discriminator efficiency curves for major triangle #7. The efficiency curve for the major triangle #7 discriminator may be measured directly by means of a latch bit or derived as in fig. B.7. The derived curve agrees well with the measured efficiency for this discriminator. The major triangle energy is given in MeV.

References

1) R. Ford and W. Nelson, "The EGS Code System: Computer Programs for the Monte Carlo Simulation of Electromagnetic Cascade Showers (Version 3)," SLAC Report 210, June 1978.

2) H. Fesefeldt, "The Simulation of Hadronic Showers: Physics and Applications," U. of Aachen, Tech. Hochsch., III Phys. Inst., PITHA-85/02, 1985.

3) R. Lee, Ph.D. Thesis, "Radiative Decays of the Psi Prime to All-photon Final States," Stanford U., 1985. SLAC Report-282. Unpublished.

4) B. Niczyporuk, "Survey of Endcaps," Internal Crystal Ball Memorandum, Aug. 1983. DESY